

Supporting Information

**Putting Cyaphide in its Place: Determining the Donor/Acceptor
Properties of the κ C-Cyaphido Ligand**

Contents

1. Experimental section.....	2
1.1 General experimental methods	2
1.2 Synthesis of reported compounds.....	3
1.2.1 Synthesis of $\text{Co}(\text{DippPDI})(\text{CCH})$ (Co_{CCH})	3
1.2.2 Synthesis of $\text{Na}(\text{THF})\text{Co}(\text{PIEA})(\text{CCH})$	5
1.2.3 Synthesis of $[\text{Co}(\text{DippPDI})(\text{CO})][\text{BAR}^{\text{F}}_4]$ (Co_{CO^+})	7
1.2.4 Synthesis of $[\text{Co}(\text{DippPDI})(\text{CN}^t\text{Bu})][\text{BAR}^{\text{F}}_4]$ ($\text{Co}_{\text{CNBu}^+}$)	9
1.2.5 Synthesis of $[\text{Co}(\text{DippPDI})(\text{CN}^t\text{Bu})_2][\text{BAR}^{\text{F}}_4]$	11
1.2.6 Synthesis of $\text{Rh}(\text{DippPDI})(\text{CP})$ (Rh_{CP}).....	13
1.2.7 Synthesis of $\text{Rh}(\text{DippPDI})(\text{CCH})$ (Rh_{CCH})	16
1.2.8 Synthesis of $[\text{Rh}(\text{DippPDI})(\text{CO})][\text{BAR}^{\text{F}}_4]$ (Rh_{CO^+})	18
1.2.9 Synthesis of $[\text{Rh}(\text{DippPDI})(\text{CN}^t\text{Bu})][\text{BAR}^{\text{F}}_4]$ ($\text{Rh}_{\text{CNBu}^+}$)	20
1.2.10 Synthesis of $[\text{Rh}(\text{DippPDI})(\text{C}_2\text{H}_4)][\text{BAR}^{\text{F}}_4]$ ($\text{Rh}_{\text{ethene}^+}$).....	22
1.2.11 Attempted syntheses of $\text{Co}(\text{DippPDI})(\text{CN})$ (Co_{CN}) and $\text{Rh}(\text{DippPDI})(\text{CN})$ (Rh_{CN}).....	24
1.3 Other characterization data	25
2. Single crystal X-ray diffraction data	27
3. Computational details	43
3.1. General computational methods	43
3.2. Calculations on anions	44
3.3. Natural Bond Orbital analysis.....	46
3.4. Energy decomposition analysis.....	47
3.5. Data analysis.....	50
4. References	60

1. Experimental section

1.1 General experimental methods

Synthetic methods. All reactions and product manipulations were carried out using standard Schlenk-line techniques under an inert atmosphere of argon, or in a dinitrogen filled glovebox (MBraun LABstar glovebox maintained at < 0.1 ppm H₂O and < 0.1 ppm O₂). Na(BAr^F₄),¹ Co(^{Dipp}PDI)Cl,² Co(^{Dipp}PDI)Me, [Co(^{Dipp}PDI)(N₂)] [B(Me)(C₆F₅)₃],³ Rh(^{Dipp}PDI)Cl,⁴ and Rh(^{Dipp}PDI)Me⁵ were synthesized according to previously reported synthetic procedures. Crystals of Rh(^{Dipp}PDI)Cl suitable for SCXRD were obtained from THF/pentane at -20 °C. Crystals of Rh(^{Dipp}PDI)Me suitable for SCXRD were obtained from toluene/pentane at -35 °C. Mg(^{Dipp}NacNac)(dioxane)(CP) was generated *in situ* according to a previously reported procedure.⁶ Ethynylmagnesium chloride (Sigma Aldrich, 0.5 M in THF), sodium acetylide (Sigma Aldrich 95%), *tert*-butyl isocyanide (Sigma Aldrich 98%), carbon monoxide (BOC), ethylene (BOC), potassium cyanide (TCI >98%), trimethylsilyl cyanide (Sigma Aldrich 98%), and anhydrous methanol (99.8%) were purchased and used as received. Tetrabutylammonium cyanide (Sigma Aldrich 95%) was recrystallized from anhydrous THF/hexane. Toluene (Sigma Aldrich HPLC grade), hexane (Sigma Aldrich HPLC grade), and pentane (Sigma Aldrich HPLC grade) were purified using an MBraun SPS-800 solvent system. THF (Sigma Aldrich HPLC grade) was distilled over sodium/benzophenone. 1,2-DFB (Alfa Aesar, 98%) was distilled over CaH₂. C₆D₆ (Aldrich, 99.5%) was degassed and dried over CaH₂. d₈-THF (Aldrich, 99.5%) was distilled over NaK. All dry solvents were stored under argon in gas-tight ampoules over activated 3 Å molecular sieves.

Characterization techniques. NMR spectra were acquired on a Bruker AVIII 400 MHz NMR spectrometer (¹H 400 MHz, ³¹P 162 MHz) or a Bruker Avance NEO 600 MHz NMR spectrometer with a broadband helium cryoprobe (¹³C 151 MHz). ¹H and ¹³C NMR spectra in deuterated solvents were referenced to the most downfield solvent resonance (¹H NMR C₆D₆: δ = 7.16 ppm, d₈-THF: δ = 3.58 ppm; ¹³C NMR C₆D₆: δ = 128.06 ppm, d₈-THF: δ = 67.21 ppm). ¹H and ¹³C NMR spectra in 1,2-DFB were measured locked to a C₆D₆ capillary and referenced according to literature methods. ³¹P NMR spectra were externally referenced to an 85% solution of H₃PO₄ in H₂O. Infrared spectra were acquired on a Thermo Scientific iS5 FTIR spectrometer with an iD3 ATR stage. Raman spectra were acquired on a Thermo Fisher Scientific DXR3 SmartRaman spectrometer using a 532 nm laser. UV-vis absorption spectra were acquired for dilute toluene solutions on a Horiba Duetta spectrofluorometer at 298 K using an anaerobic quartz cuvette. Elemental analyses were carried out by Elemental Microanalyses Ltd. (Devon, U.K.) or by London Metropolitan University (London, U.K.). Samples (approx. 5 mg) were submitted in flame sealed glass tubes.

1.2 Synthesis of reported compounds

1.2.1 Synthesis of $\text{Co}(\text{DippPDI})(\text{CCH})$ (Co_{CCH})

$\text{Co}(\text{DippPDI})\text{Cl}$ (100 mg, 0.17 mmol) was dissolved in THF (10 mL). Ethynylmagnesium chloride (0.7 mL, 0.25 M in THF, 0.18 mmol) was added dropwise, and stirred for 3 days. This was then filtered, and the solvent removed under reduced pressure. The product was crystallized from a 3:1 mixture of pentane/toluene at $-20\text{ }^\circ\text{C}$ for 3 days, then isolated by filtration to give $\text{Co}(\text{DippPDI})(\text{CCH})$ as dark purple crystals. Yield: 33 mg, 0.06 mmol, 34%. Anal. Calcd. (%) for $\text{C}_{35}\text{H}_{44}\text{N}_3\text{Co}$: C, 74.31; H, 7.84; N, 7.43. Found: C, 72.86; H, 7.17; N, 6.75.

^1H NMR (600 MHz, C_6D_6): δ (ppm) 10.05 (t, $^3J_{\text{H-H}} = 7.7$, 1H, pyridine *para* CH), 7.50 (t, $^3J_{\text{H-H}} = 7.8$, 2H, Dipp *para* CH), 7.37 (d, $^3J_{\text{H-H}} = 7.8$, 4H, Dipp *meta* CH), 7.08 (d, $^3J_{\text{H-H}} = 7.7$, 2H, pyridine *meta* CH), 3.27 (sept, $^3J_{\text{H-H}} = 6.8$ Hz, 4H, Dipp CH(CH_3)₂), 2.27 (s, 1H, CCH), 1.25 (d, $^3J_{\text{H-H}} = 6.8$ Hz, 12H, Dipp CH(CH_3)₂), 0.94 (d, $^3J_{\text{H-H}} = 6.8$ Hz, 12H, Dipp CH(CH_3)₂), -0.33 (s, 6H, imine NCCH_3).

$^{13}\text{C}\{^1\text{H}\}$ NMR (151 MHz, C_6D_6): δ (ppm) 169.05 (s, imine NCCH_3), 154.83 (s, Dipp *ipso* C), 154.25 (s, Dipp *ortho* C), 140.84 (s, pyridine *ortho* C), 132.24 (s, CCH), 126.65 (s, Dipp *para* C), 124.42 (s, pyridine *meta* C), 123.72 (s, Dipp *meta* C), 117.57 (s, pyridine *para* C), 29.01 (s, Dipp CH(CH_3)₂), 24.04 (s, Dipp CH(CH_3)₂), 23.53 (s, Dipp CH(CH_3)₂), 22.54 (s, imine NCCH_3).

UV-vis: λ_{max} (nm) 559.

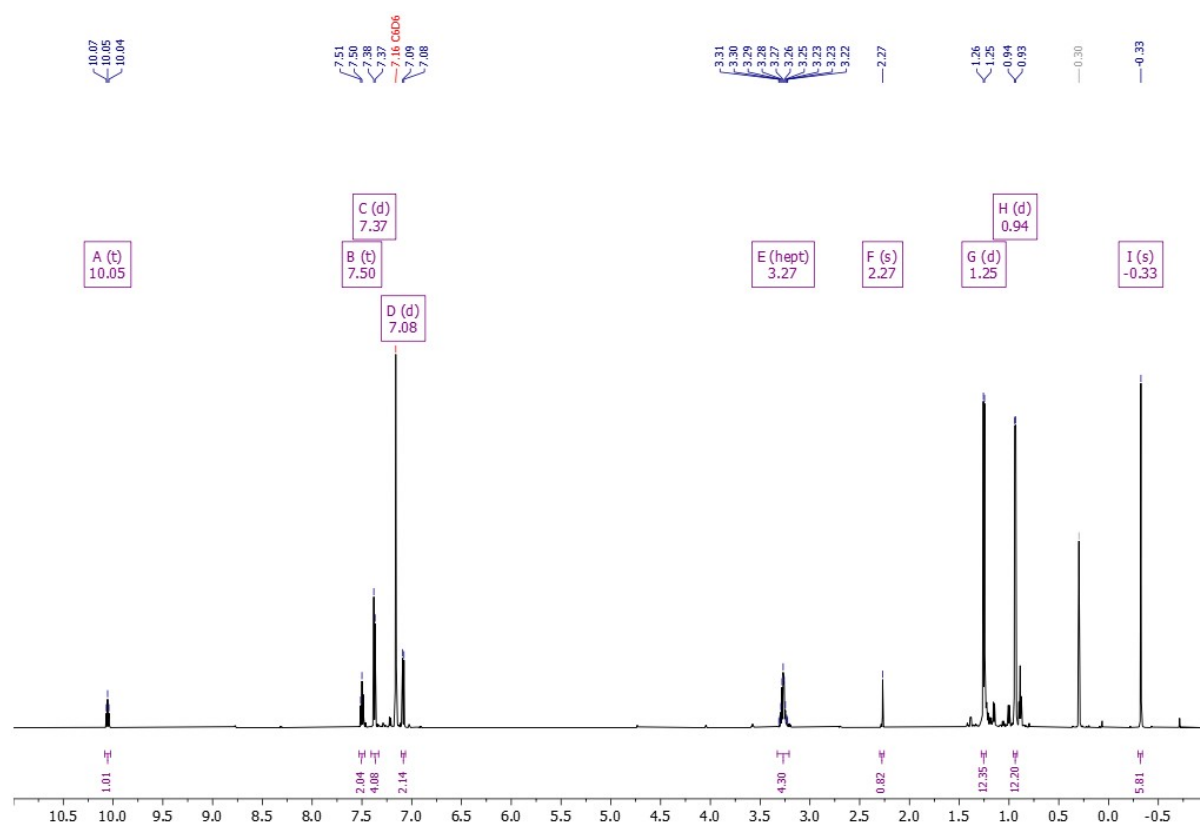


Figure S1. ^1H NMR (600 MHz) spectrum of Co_{CCH} in C_6D_6 .

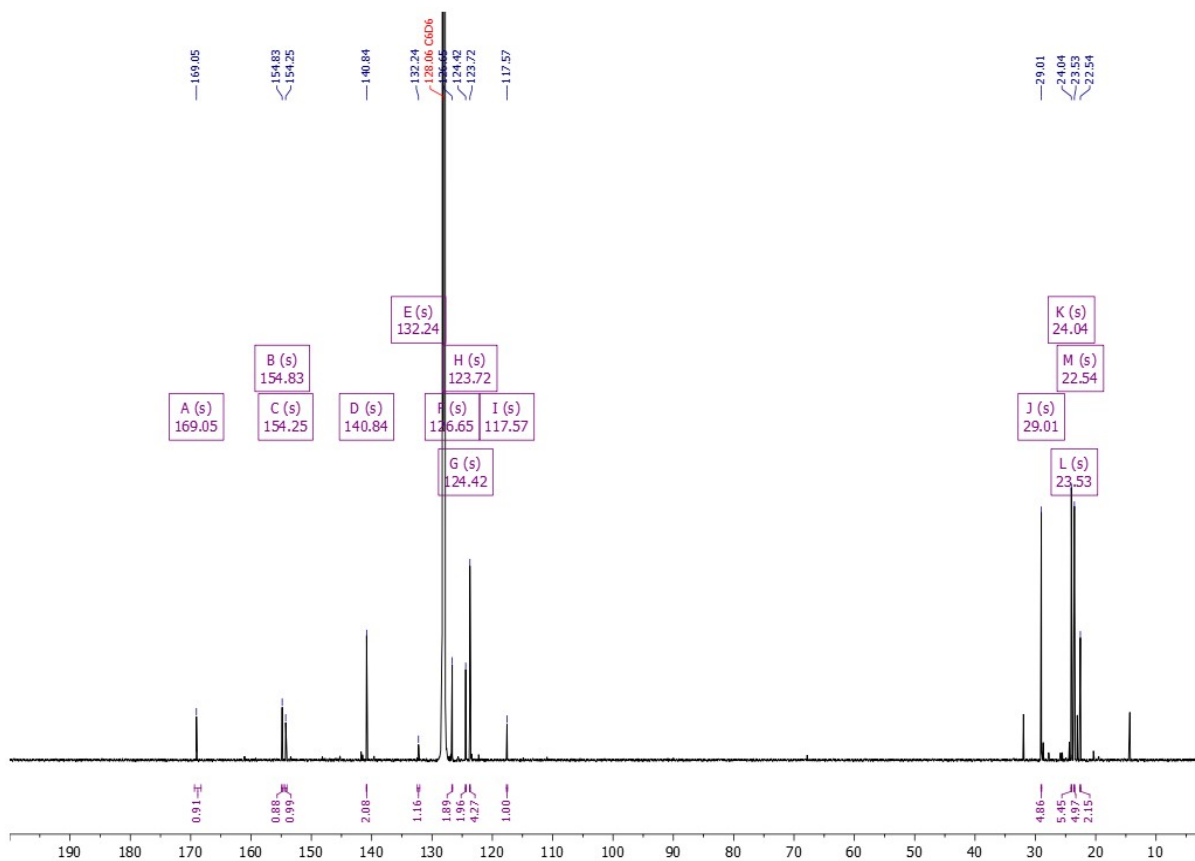


Figure S2. $^{13}\text{C}\{^1\text{H}\}$ NMR (600 MHz) spectrum of CoCCH in C_6D_6 .

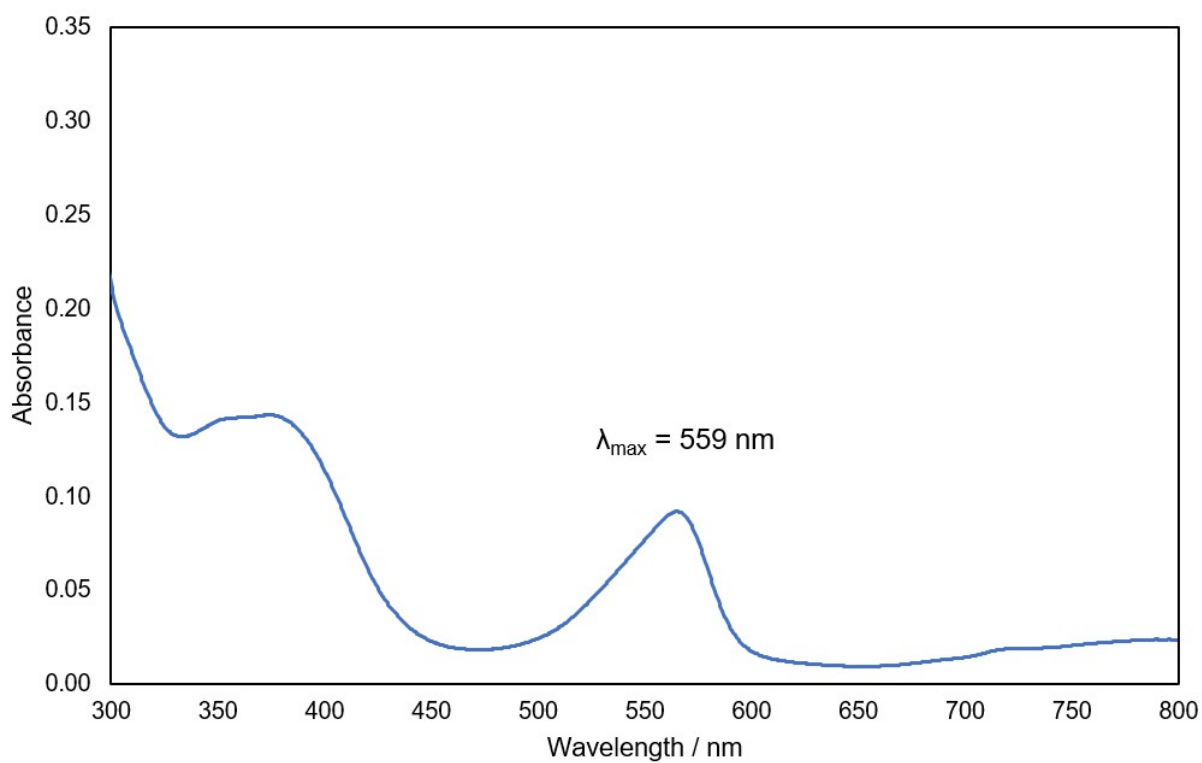


Figure S3. UV-vis absorption spectrum of CoCCH in toluene.

1.2.2 Synthesis of Na(THF)Co(PIEA)(CCH)

Co(^{Dipp}PDI)Cl (120 mg, 0.21 mmol) and sodium acetylide (20 mg, 0.42 mmol) were dissolved in THF (15 mL), then stirred overnight. The solvent was removed under reduced pressure, then extracted with hexane (3 × 10 mL). This solution was concentrated, then crystallized at -20 °C for 3 days, yielding dark red crystals of Na(THF)Co(PIEA)(CCH) that were isolated by filtration. Yield: 28 mg, 0.04 mmol, 20%. Anal. Calcd. (%) for C₃₉H₅₁N₃CoNaO: C, 71.00; H, 7.79; N, 6.37. Found: C, 69.99; H, 7.42; N, 6.24. In solution, Na(THF)Co(^{Dipp}PIEA)(CCH) (**1**) appears to be in equilibrium with the separated ion pair [Na(THF)_n][Co(^{Dipp}PIEA)(CCH)] (**2**).

¹H NMR (400 MHz, d₈-THF): δ(ppm) 11.00 (d, ³J_{H-H} = 7.3 Hz, 1H, **1** *o*-enamine pyridine *meta* CH), 10.51 (t, ³J_{H-H} = 7.8 Hz, 1H, **2** pyridine *para* CH), 8.35 (d, ³J_{H-H} = 8.1 Hz, 1H, **1** *o*-imine pyridine *meta* CH), 8.22–8.15 (m, 1H, **1** pyridine *para* CH), 7.75 (t, ³J_{H-H} = 7.8 Hz, 2H, **2** pyridine *meta* CH), 7.43–7.37 (m, 1H, **1** enamine Dipp *para* CH), 7.34 (t, ³J_{H-H} = 7.6 Hz, 2H, **2** Dipp *para* CH), 7.27 (d, ³J_{H-H} = 7.7 Hz, 2H, **1** enamine Dipp *meta* CH), 7.07 (d, ³J_{H-H} = 7.6 Hz, 2H, **2** Dipp *meta* CH), 6.78 (dd, ³J_{H-H} = 8.3, 6.6 Hz, 1H, **1** imine Dipp *para* CH), 6.72–6.67 (m, 2H, **1** imine Dipp *meta* CH), 5.25 (s, 1H, **1** enamine NCCH₂), 3.47 (s, 1H, **1** enamine NCCH₂), 3.11 (sept, ³J_{H-H} = 6.9 Hz, 2H, **1** enamine Dipp CH(CH₃)₂), 2.76 (s, 1H, **1** CCH), 2.40 (sept, ³J_{H-H} = 6.9 Hz, 2H, **1** imine Dipp CH(CH₃)₂), 2.27 (s, 1H, **2** CCH), 2.03 (sept, ³J_{H-H} = 6.9 Hz, 4H, **2** Dipp CH(CH₃)₂), 1.54 (d, ³J_{H-H} = 6.8 Hz, 12H, **2** Dipp CH(CH₃)₂), 1.25 (d, ³J_{H-H} = 6.8 Hz, 6H, **1** enamine Dipp CH(CH₃)₂), 0.94 (d, ³J_{H-H} = 6.8 Hz, 6H, **1** imine Dipp CH(CH₃)₂), 0.66 (d, ³J_{H-H} = 7.0 Hz, 12H, **2** Dipp CH(CH₃)₂), 0.64 (d, ³J_{H-H} = 6.8 Hz, 6H, **1** enamine Dipp CH(CH₃)₂), 0.43 (d, ³J_{H-H} = 6.8 Hz, 6H, **1** imine Dipp CH(CH₃)₂), 0.03 (bs, 5H, **2** imine/enamine NCCH₃/NCCH₂), -4.20 (s, 3H, **1** imine NCCH₃).

¹³C{¹H} NMR (151 MHz, d₈-THF): δ(ppm) 174.87 (**1** enamine NCCH₂), 164.26 (**2** enamine/imine NCCH₃/NCCH₂), 158.43 (**2** Dipp *ipso* C), 156.34 (**1** imine NCCH₃), 155.17 (**1** enamine Dipp *ipso* C), 152.01 (**1** imine Dipp *ipso* C), 146.80 (**1** imine Dipp *ortho* C), 141.15 (**1** enamine Dipp *para* C), 135.82 (**2** Dipp *ortho* C), 132.18 (**1** pyridine *para* C), 131.65 (**2** pyridine *ortho* C), 126.42 (**1** enamine Dipp *ortho* C), 125.08 (**2** pyridine *meta* C), 124.39 (**2** Dipp *para* C), 123.62 (**1** enamine Dipp *meta* C), 122.55 (**1** imine Dipp *meta* C), 121.75 (**2** Dipp *meta* C), 121.60 (**1** imine Dipp *para* C), 114.66 (**1** *o*-imine pyridine *meta* C), 102.20 (**1** *o*-enamine pyridine *meta* C), 97.72 (**1** CCH), 81.63 (**1** enamine NCCH₂), 68.03 (**2** CCH), 29.15 (**1** enamine Dipp CH(CH₃)₂), 27.87 (**2** Dipp CH(CH₃)₂), 26.94 (**1** imine Dipp CH(CH₃)₂), 26.19 (**1** imine NCCH₃), 24.59 (**1** imine Dipp CH(CH₃)₂), 24.39 (**2** Dipp CH(CH₃)₂), 23.94 (**1** enamine Dipp CH(CH₃)₂), 23.56 (**1** imine Dipp CH(CH₃)₂), 23.43 (**1** enamine Dipp CH(CH₃)₂), 23.24 (**2** Dipp CH(CH₃)₂).

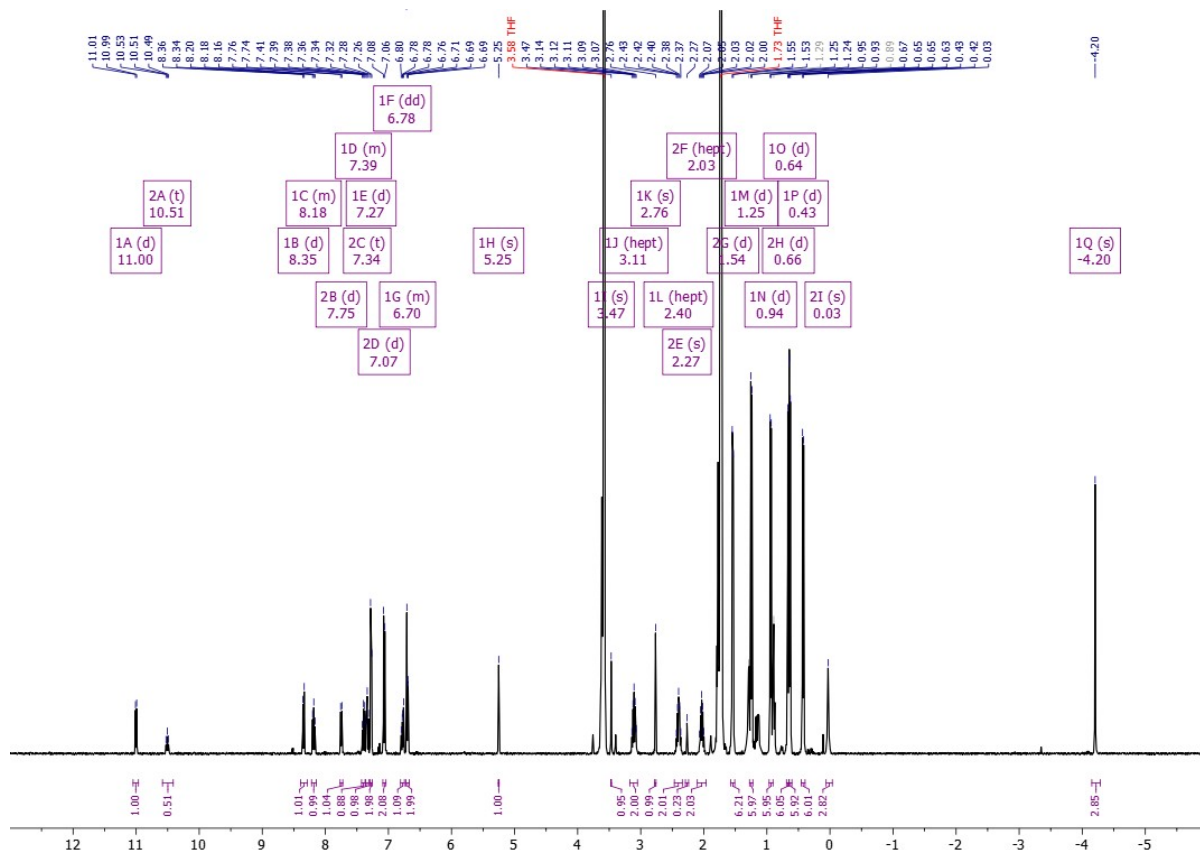


Figure S4. ^1H NMR (400 MHz) spectrum of $\text{Na}(\text{THF})\text{Co}(\text{DippPIEA})(\text{CCH})$ in $d_8\text{-THF}$.

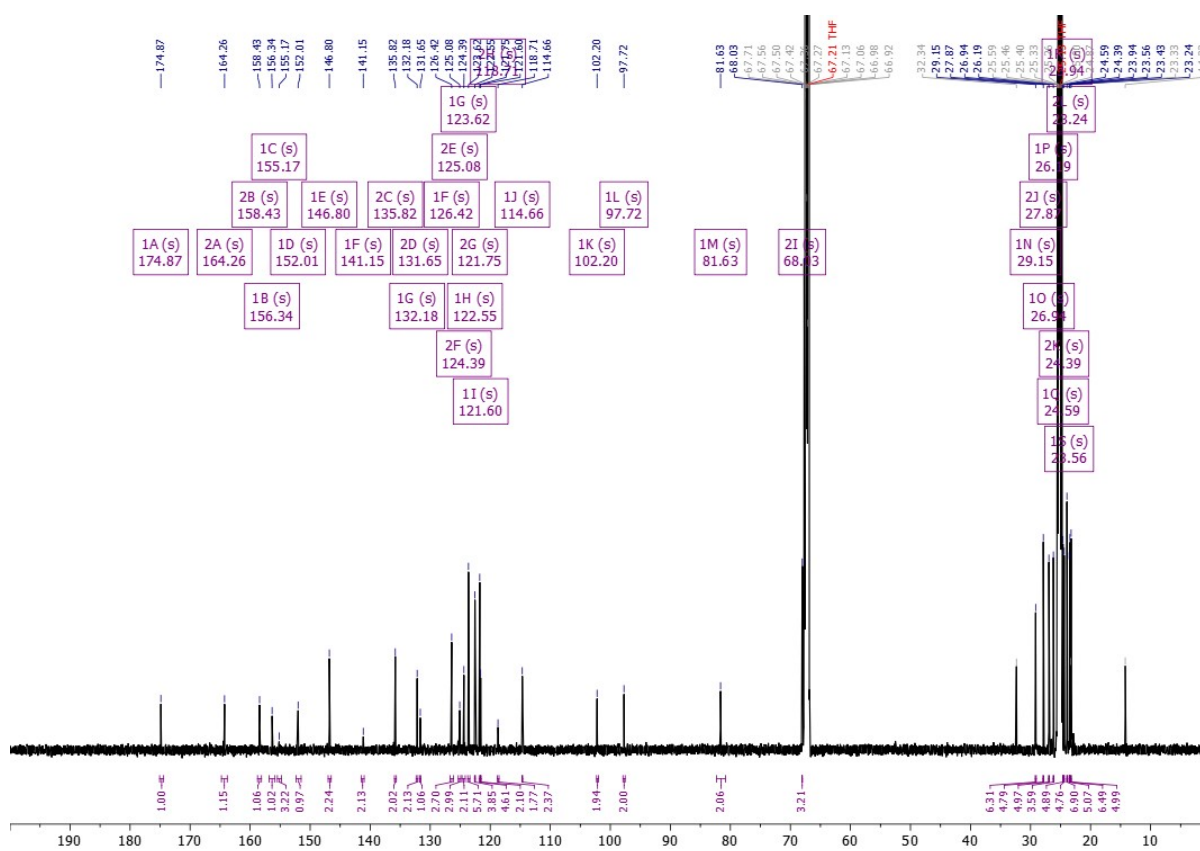


Figure S5. $^{13}\text{C}\{^1\text{H}\}$ NMR (151 MHz) spectrum of $\text{Na}(\text{THF})\text{Co}(\text{DippPIEA})(\text{CCH})$ in $d_8\text{-THF}$.

1.2.3 Synthesis of [Co(^{Dipp}PDI)(CO)][BAr^F₄] (Co_{co}⁺)

Co(^{Dipp}PDI)Cl (100 mg, 0.17 mmol) and Na(BAr^F₄) (154 mg, 0.17 mmol) were dissolved in 1,2-DFB (3 mL). The solution was degassed, then placed under CO gas (1 bar). The dark blue solution was degassed then filtered. The filtrate was concentrated, then layered with pentane (30 mL) for one week. After filtration, [Co(^{Dipp}PDI)(CO)][BAr^F₄] was obtained as large dark blue crystals. Yield: 145 mg, 0.10 mmol, 58%. Anal. Calcd. (%) for C₆₆H₅₅N₃BCoF₂₄O: C, 55.36; H, 3.87; N, 2.93. Found: C, 54.92; H, 2.85; N, 2.87.

¹H NMR (400 MHz, 1,2-DFB/C₆D₆): δ(ppm) 8.17–8.09 (m, 8H, BAr^F₄ *ortho* CH) 7.69 (t, ³J_{H-H} = 8.0, 1H, pyridine *para* CH), 7.49 (bs, 4H, BAr^F₄ *para* CH), 7.42 (d, ³J_{H-H} = 8.0, 2H, pyridine *meta* CH), 3.01 (sept, ³J_{H-H} = 6.8 Hz, 4H, Dipp CH(CH₃)₂), 1.59 (s, 6H, imine NCCH₃), 1.30 (d, ³J_{H-H} = 6.8 Hz, 12H, Dipp CH(CH₃)₂), 1.04 (d, ³J_{H-H} = 6.8 Hz, 12H, Dipp CH(CH₃)₂). The signals for some aromatic protons could not be located due to overlap with 1,2-DFB solvent peaks.

¹³C{¹H} NMR (151 MHz, 1,2-DFB/C₆D₆): δ(ppm) 175.64 (s, imine NCCH₃), 162.60 (q, ¹J_{C-B} = 49.7 Hz, BAr^F₄ *ipso* C), 157.07 (s, Dipp *ipso* C), 144.91 (s, Dipp *ortho* C), 141.80 (s, pyridine *para* C), 138.29 (s, ArC), 135.16 (bs, BAr^F₄ *ortho* C), 129.76 (qq, ²J_{C-F} = 31.5 Hz, ²J_{C-B} = 3.0 Hz, BAr^F₄ *meta* C), 128.86 (s, ArC), 125.86 (s, pyridine *meta* C), 124.06 (s, ArC), 117.73–117.56 (m, BAr^F₄ *para* C), 29.15 (s, Dipp CH(CH₃)₂), 23.01 (s, CH(CH₃)₂), 22.83 (s, Dipp CH(CH₃)₂), 16.48 (s, imine NCCH₃). The signals for some aromatic carbons could not be assigned due to overlap with 1,2-DFB solvent peaks.

UV-vis: λ_{max}(nm) 593.

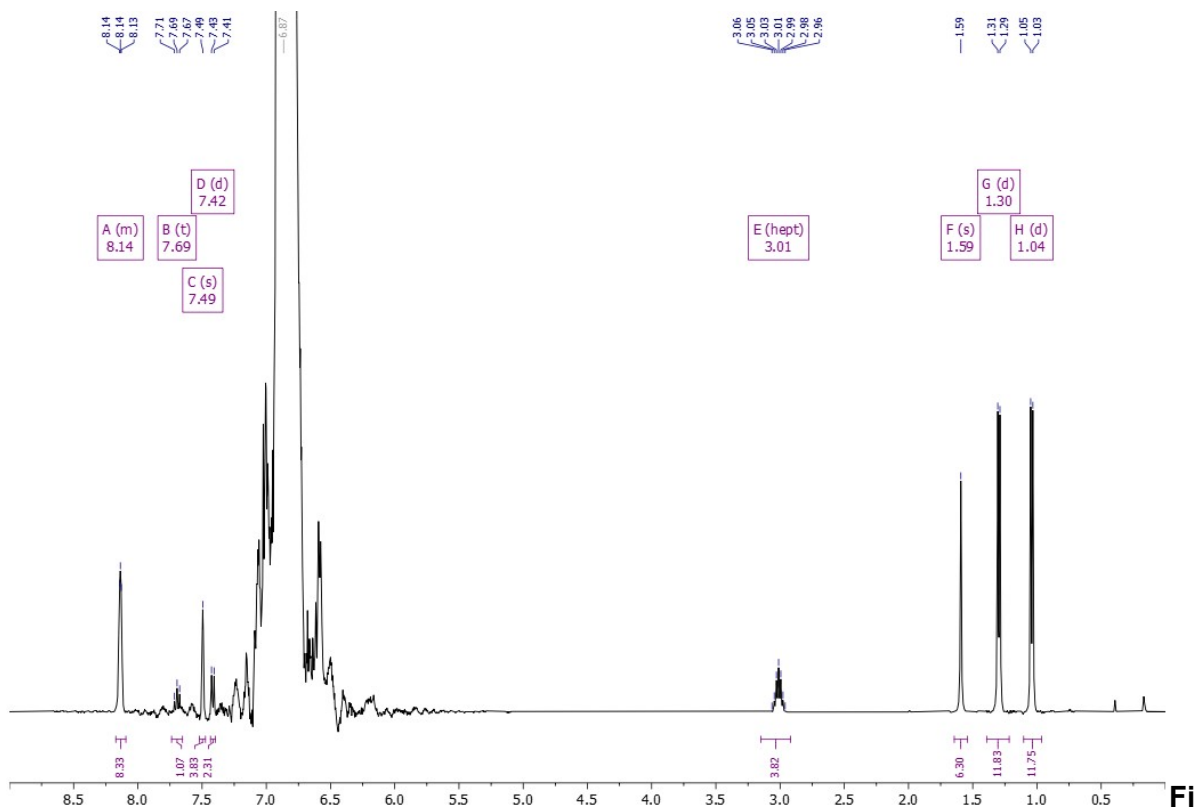


Figure S6. ^1H NMR (400 MHz) spectrum of CoCo^+ in 1,2-DFB, locked to a C_6D_6 capillary.

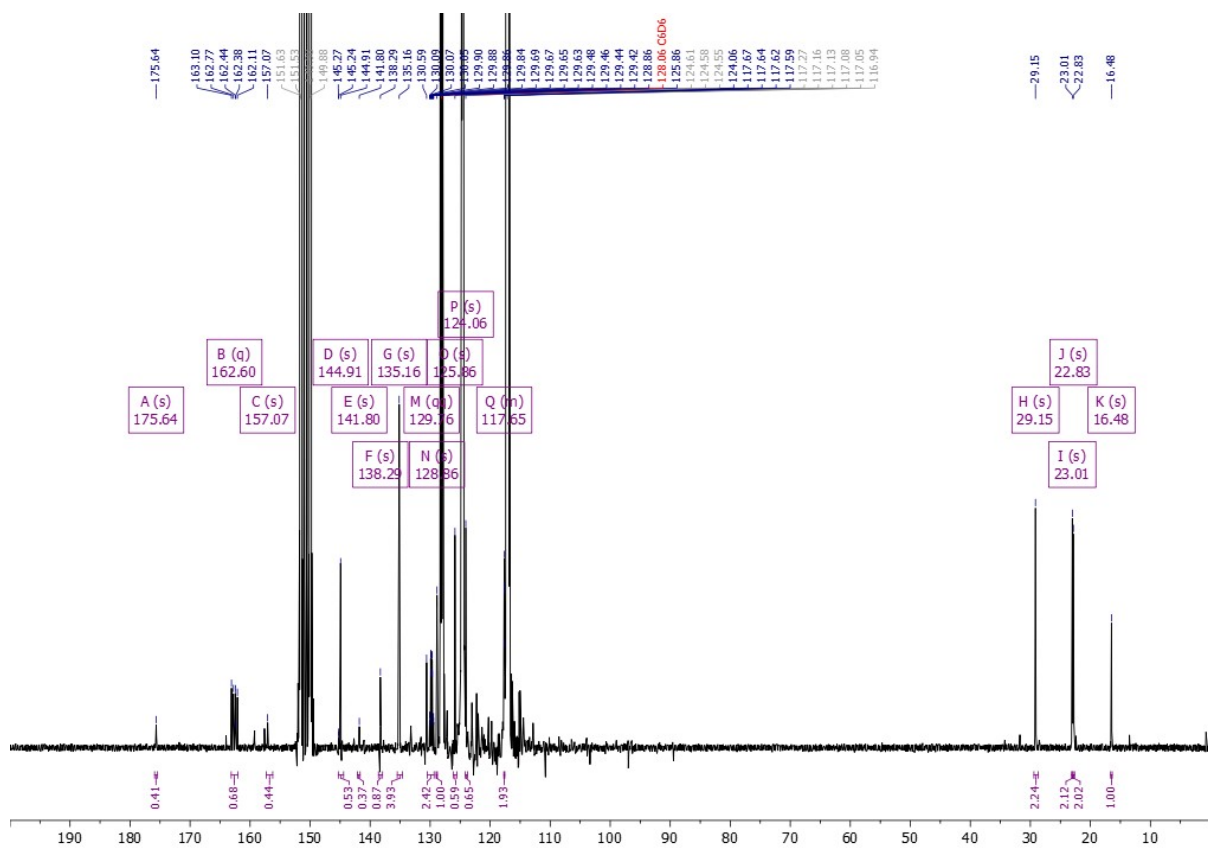


Figure S7. $^{13}\text{C}\{^1\text{H}\}$ NMR (600 MHz) spectrum of CoCo^+ in 1,2-DFB, locked to a C_6D_6 capillary.

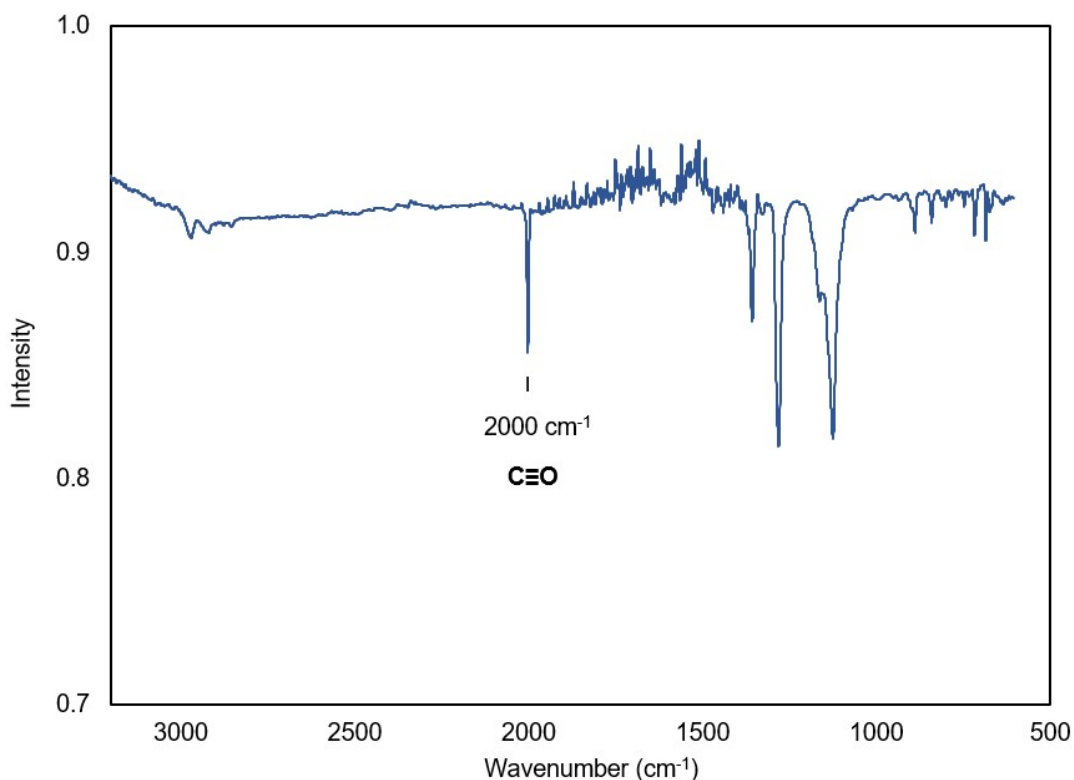


Figure S8. ATR-FTIR spectrum of CoCo^+ .

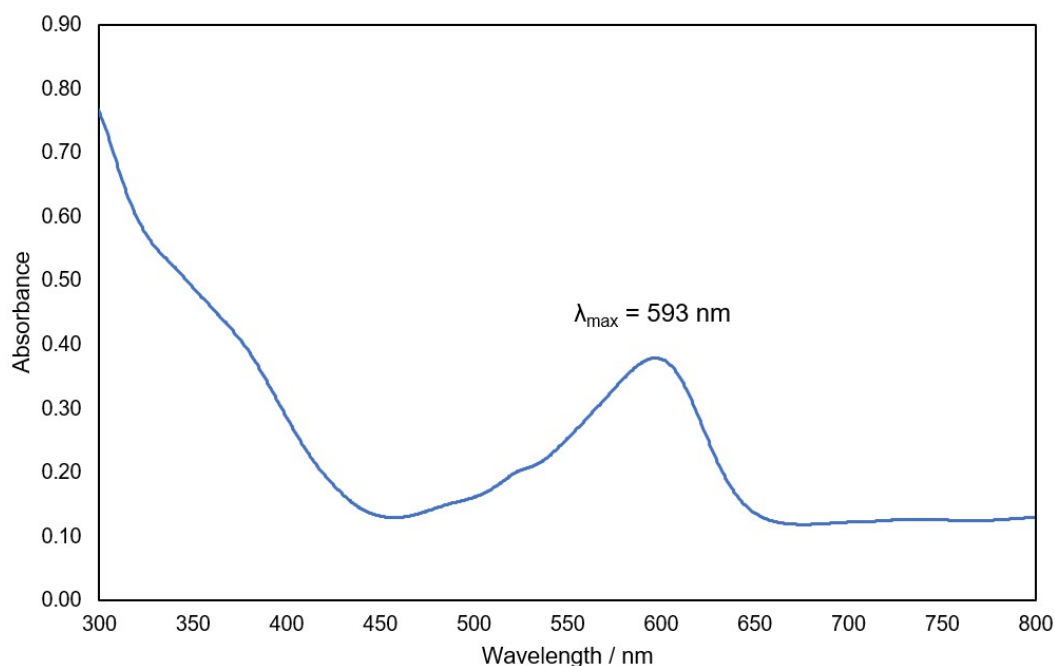


Figure S9. UV-vis absorption spectrum of CoCo^+ in toluene.

1.2.4 Synthesis of $[\text{Co}(\text{DippPDI})(\text{CN}^t\text{Bu})][\text{BAR}^{\text{F}}_4]$ ($\text{Co}_{\text{CNBu}^+}$)

$\text{Co}(\text{DippPDI})\text{Cl}$ (50 mg, 0.09 mmol) and $\text{Na}(\text{BAR}^{\text{F}}_4)$ (77 mg, 0.09 mmol) were dissolved in 1,2-DFB (3 mL). A solution of $^t\text{BuNC}$ (7 mg, 0.08 mmol) in DFB (0.5 mL) was added dropwise. The dark blue reaction mixture was stirred for 1 h, then filtered. The filtrate was concentrated, then layered with pentane (30 mL) for one week. After filtration, $[\text{Co}(\text{DippPDI})(\text{CN}^t\text{Bu})][\text{BAR}^{\text{F}}_4]$

was obtained as dark blue crystals. Yield: 99 mg, 0.07 mmol, 77%. Anal. Calcd. (%) for $C_{70}H_{64}N_4BCoF_{24}$: C, 56.54; H, 4.34; N, 3.96. Found: C, 56.75; H, 3.95; N, 4.42.

1H NMR (600 MHz, 1,2-DFB/ C_6D_6): δ (ppm) 8.59 (t, $^3J_{H-H} = 7.9$, 1H, pyridine *para* CH), 8.17–8.11 (m, 8H, BAr^F *ortho* CH), 7.50 (bs, 4H, BAr^F *para* CH), 7.23 (d, $^3J_{H-H} = 7.9$, 2H, pyridine *meta* CH), 2.67 (sept, $^3J_{H-H} = 6.9$ Hz, 4H, Dipp $CH(CH_3)_2$), 1.08 (d, $^3J_{H-H} = 6.9$ Hz, 12H, Dipp $CH(CH_3)_2$), 0.96 (s, 6H, imine $NCCH_3$), 0.84 (d, $^3J_{H-H} = 6.9$ Hz, 12H, Dipp $CH(CH_3)_2$), 0.64 (s, 9H, $CNC(CH_3)_3$). The signals for some aromatic protons could not be located due to overlap with 1,2-DFB solvent peaks.

$^{13}C\{^1H\}$ NMR (151 MHz, 1,2-DFB/ C_6D_6): δ (ppm) 173.05 (s, imine $NCCH_3$), 162.58 (q, $^1J_{C-B} = 49.7$ Hz, BAr^F_4 *ipso* C), 155.05 (s Dipp *ipso* C), 148.99 (s, Dipp *ortho* C), 139.85 (s, ArC), 135.13 (bs, BAr^F_4 *ortho* C), 131.46 (s, ArC), 130.57 (s, ArC), 129.74 (qq, $^2J_{C-F} = 31.8$ Hz, $^2J_{C-B} = 2.9$ Hz, BAr^F_4 *meta* C), 125.84 (s, ArC), 123.22 (s, ArC), 117.71–117.48 (m, BAr^F_4 *para* C), 58.63 (s, $CNC(CH_3)_3$), 29.24–28.94 (m, $CNC(CH_3)_3$ and Dipp $CH(CH_3)_2$), 23.05 (s, Dipp $CH(CH_3)_2$), 22.78 (s, Dipp $CH(CH_3)_2$), 18.05 (s, imine $NCCH_3$). The signals for some aromatic carbons were not assigned due to overlap with 1,2-DFB solvent peaks.

UV-vis: λ_{max} (nm) 593.

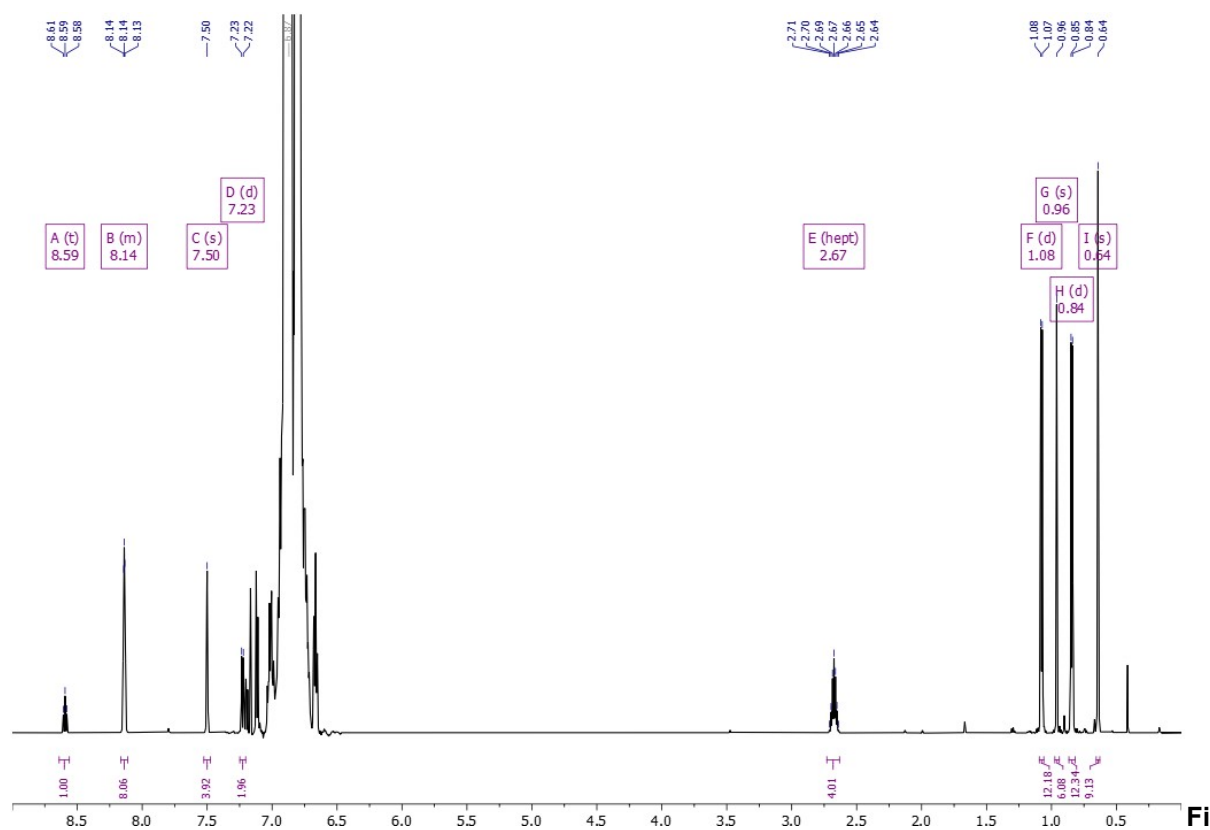
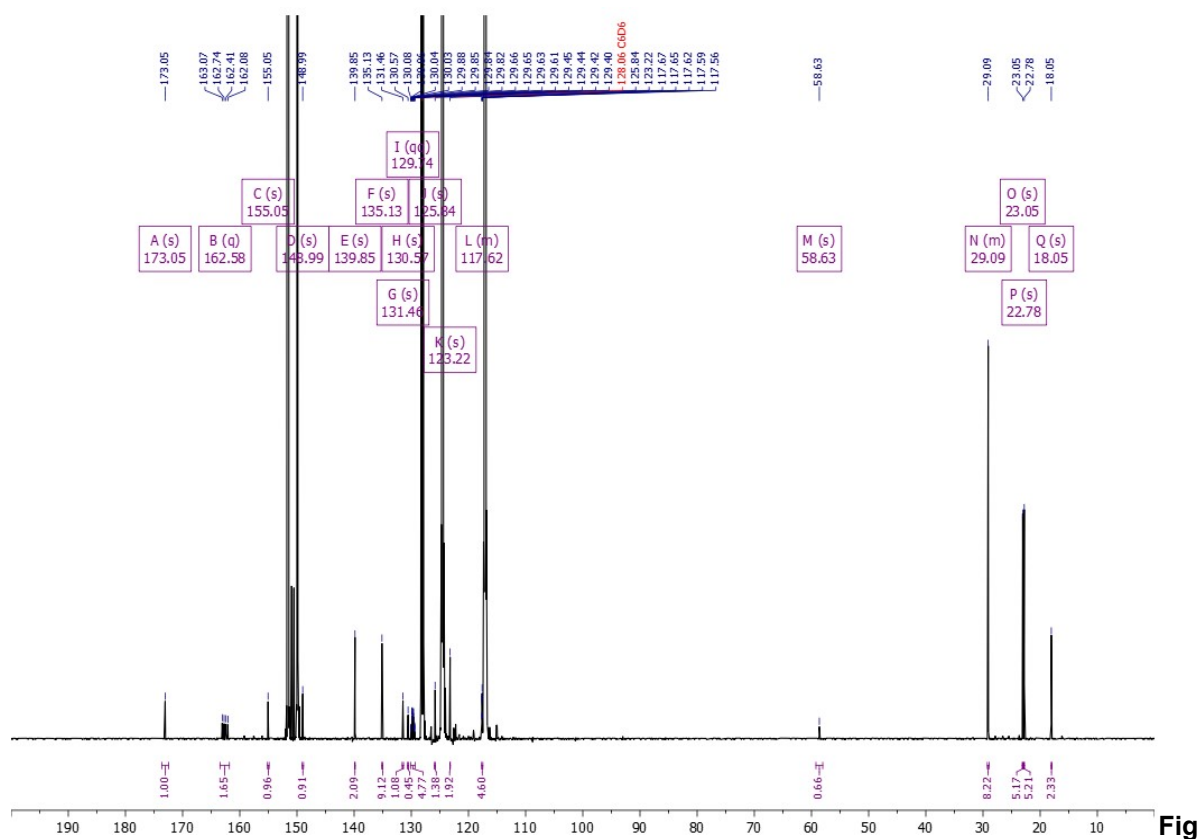


Figure S10. 1H NMR (600 MHz) spectrum of $CoCNBu^+$ in 1,2-DFB, locked to a C_6D_6 capillary.



ure S11. $^{13}\text{C}\{^1\text{H}\}$ NMR (600 MHz) spectrum of CoCNBu^+ in 1,2-DFB, locked to a C_6D_6 capillary.

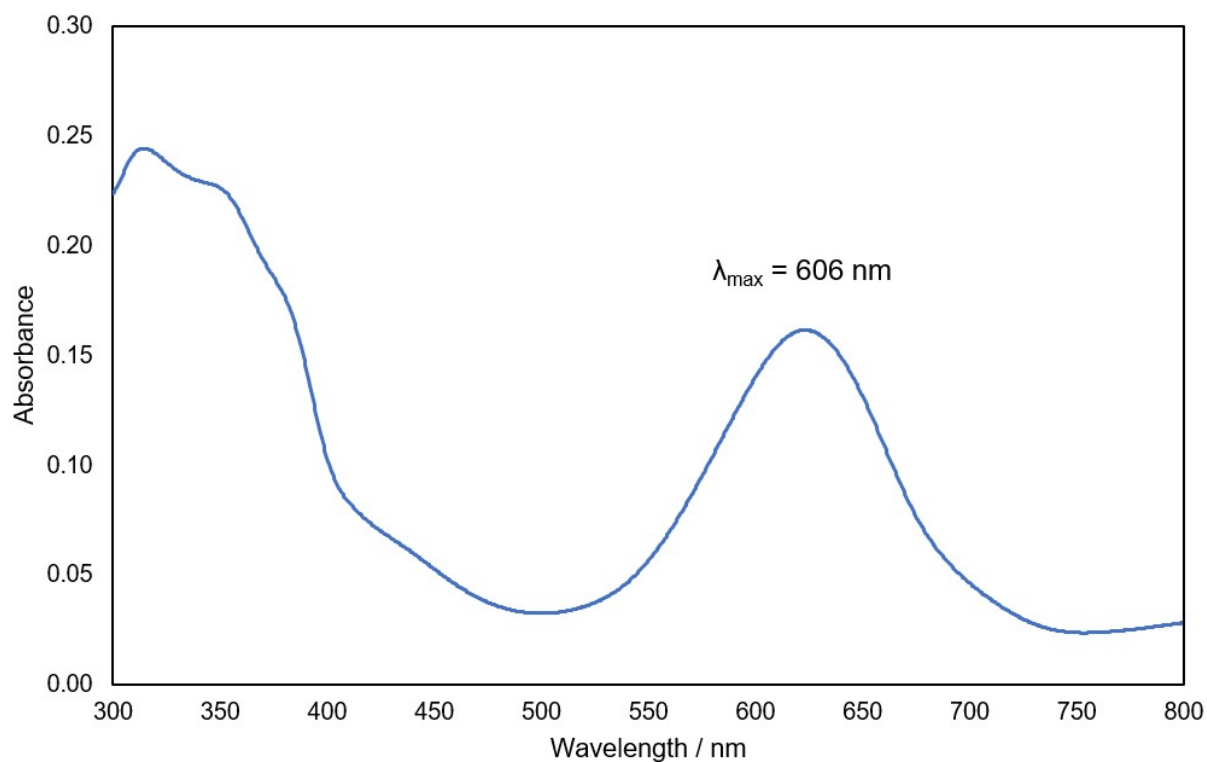


Figure S12. UV-vis absorption spectrum of CoCNBu^+ in toluene.

1.2.5 Synthesis of $[\text{Co}(\text{DippPDI})(\text{CN}^t\text{Bu})_2][\text{BAr}^{\text{F}_4}]$

$\text{Co}(\text{DippPDI})\text{Cl}$ (50 mg, 0.09 mmol) and $\text{Na}(\text{BAr}^{\text{F}_4})$ (77 mg, 0.09 mmol) were dissolved in 1,2-DFB (3 mL). $^t\text{BuNC}$ (17 mg, 0.2 mmol) was added, and the dark blue-green reaction mixture was stirred for 1 h, then filtered. The filtrate was concentrated, then layered with pentane (30 mL) for one week. After filtration, $[\text{Co}(\text{DippPDI})(\text{CN}^t\text{Bu})_2][\text{BAr}^{\text{F}_4}]$ was obtained as dark blue-green crystals. Yield: 140 mg, 0.08 mmol, 84%. Anal. Calcd. (%) for $\text{C}_{75}\text{H}_{73}\text{N}_5\text{BCoF}_{24}$: C, 57.37; H, 4.69; N, 4.46. Found: C, 57.59; H, 4.91; N, 4.25.

^1H NMR (400 MHz, 1,2-DFB/ C_6D_6): δ (ppm) 8.17–8.11 (m, 8H, BAr^{F_4} *ortho* CH), 7.84–7.75 (m, 3H, pyridine *para/meta* CH), 7.50 (bs, 4H, BAr^{F_4} *para* CH), 2.67 (sept, $^3J_{\text{H-H}} = 6.7$ Hz, 2H, Dipp CH(CH_3)₂), 2.23 (sept, $^3J_{\text{H-H}} = 6.9$ Hz, 2H, Dipp CH(CH_3)₂), 1.66 (s, 6H, imine NCCH_3), 1.30 (d, $^3J_{\text{H-H}} = 6.7$ Hz, 6H, Dipp CH(CH_3)₂), 1.11 (d, $^3J_{\text{H-H}} = 6.9$ Hz, 6H, Dipp CH(CH_3)₂), 0.93 (d, $^3J_{\text{H-H}} = 6.9$ Hz, 6H, Dipp CH(CH_3)₂), 0.90 (s, 9H, $\text{CNC}(\text{CH}_3)_3$), 0.80 (d, $^3J_{\text{H-H}} = 6.7$ Hz, 6H, Dipp CH(CH_3)₂), 0.66 (s, 9H, $\text{CNC}(\text{CH}_3)_3$). The signals for some aromatic protons could not be located due to overlap with 1,2-DFB solvent peaks.

$^{13}\text{C}\{^1\text{H}\}$ NMR (151 MHz, 1,2-DFB/ C_6D_6): δ (ppm) 184.29 (s, imine NCCH_3), 162.58 (q, $^1J_{\text{C-B}} = 49.8$ Hz, BAr^{F_4} *ipso* C), 162.37 (s pyridine ArC), 148.99 (s, pyridine *ortho* C), 141.10 (s, Dipp ArC), 138.25 (s, Dipp ArC), 135.13 (bs, BAr^{F_4} *ortho* C), 130.57 (s, Dipp ArC), 129.77 (qq, $^2J_{\text{C-F}} = 31.3$ Hz, $^2J_{\text{C-B}} = 3.2$ Hz, BAr^{F_4} *meta* C), 127.40 (s, Dipp ArC), 125.84 (s, ArC), 125.20 (s, ArC), 123.48 (s, ArC), 117.73–117.56 (m, BAr^{F_4} *para* C), 57.97 (s, $\text{CNC}(\text{CH}_3)_3$), 57.84 (s, $\text{CNC}(\text{CH}_3)_3$), 29.16 (s, $\text{CNC}(\text{CH}_3)_3$), 29.08 (s, $\text{CNC}(\text{CH}_3)_3$), 27.91 (s, Dipp CH(CH_3)₂), 27.83 (s, Dipp CH(CH_3)₂), 25.49 (s, Dipp CH(CH_3)₂), 23.65 (s, Dipp CH(CH_3)₂), 23.64 (s, Dipp CH(CH_3)₂), 22.71 (s, Dipp CH(CH_3)₂), 16.21 (s, imine NCCH_3). The signals for some aromatic carbons were not assigned due to overlap with 1,2-DFB solvent peaks.

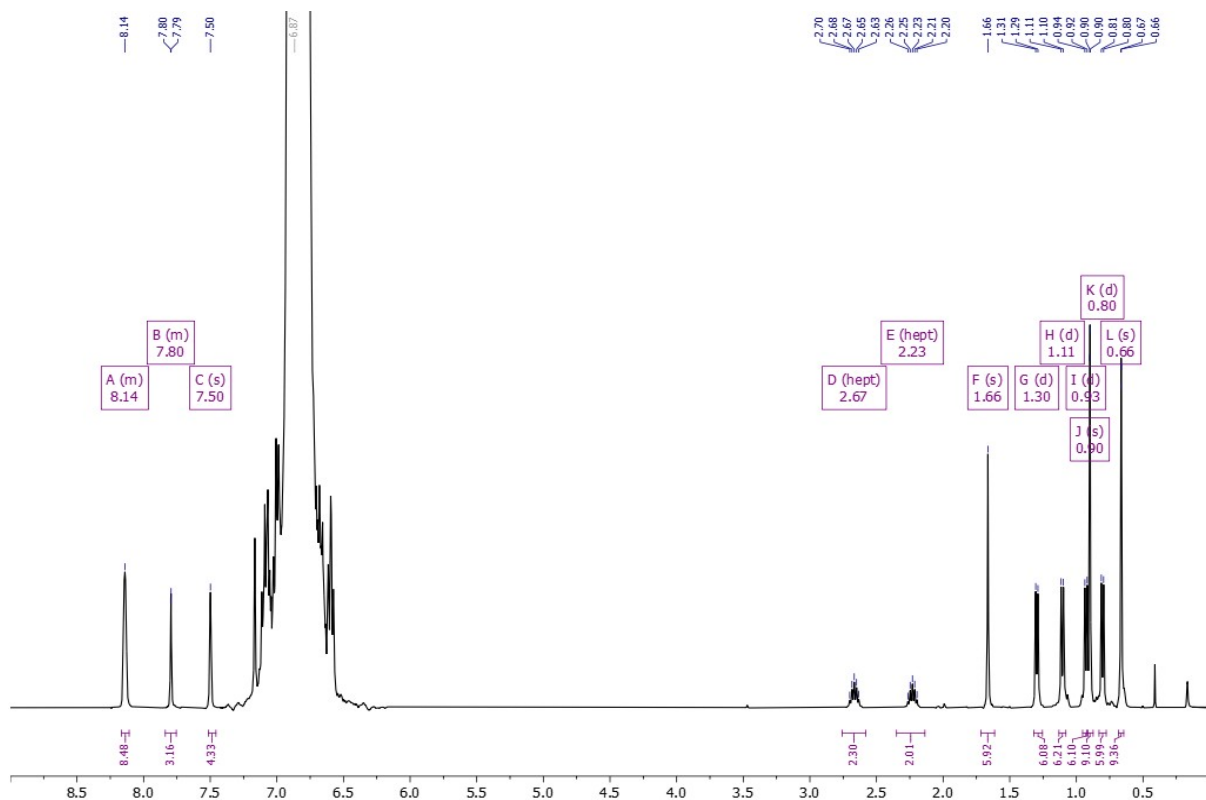


Figure S13. ^1H NMR (600 MHz) spectrum of $[\text{Co}(\text{DippPDI})(\text{CN}^t\text{Bu})_2][\text{BARF}_4]$ in 1,2-DFB, locked to a C_6D_6 capillary.

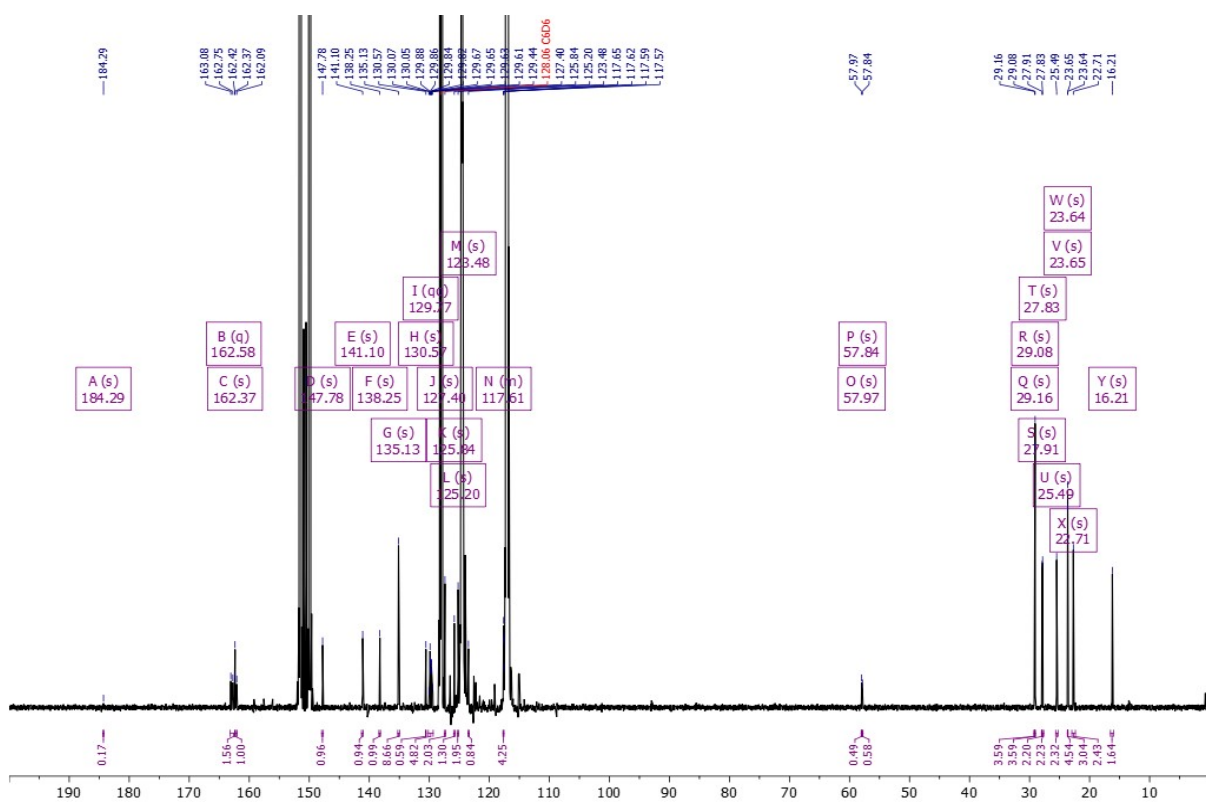


Figure S14. $^{13}\text{C}\{^1\text{H}\}$ NMR (600 MHz) spectrum of $[\text{Co}(\text{DippPDI})(\text{CN}^t\text{Bu})_2][\text{BARF}_4]$ in 1,2-DFB, locked to a C_6D_6 capillary.

1.2.6 Synthesis of $\text{Rh}(\text{DippPDI})(\text{CP})$ (Rh_{CP})

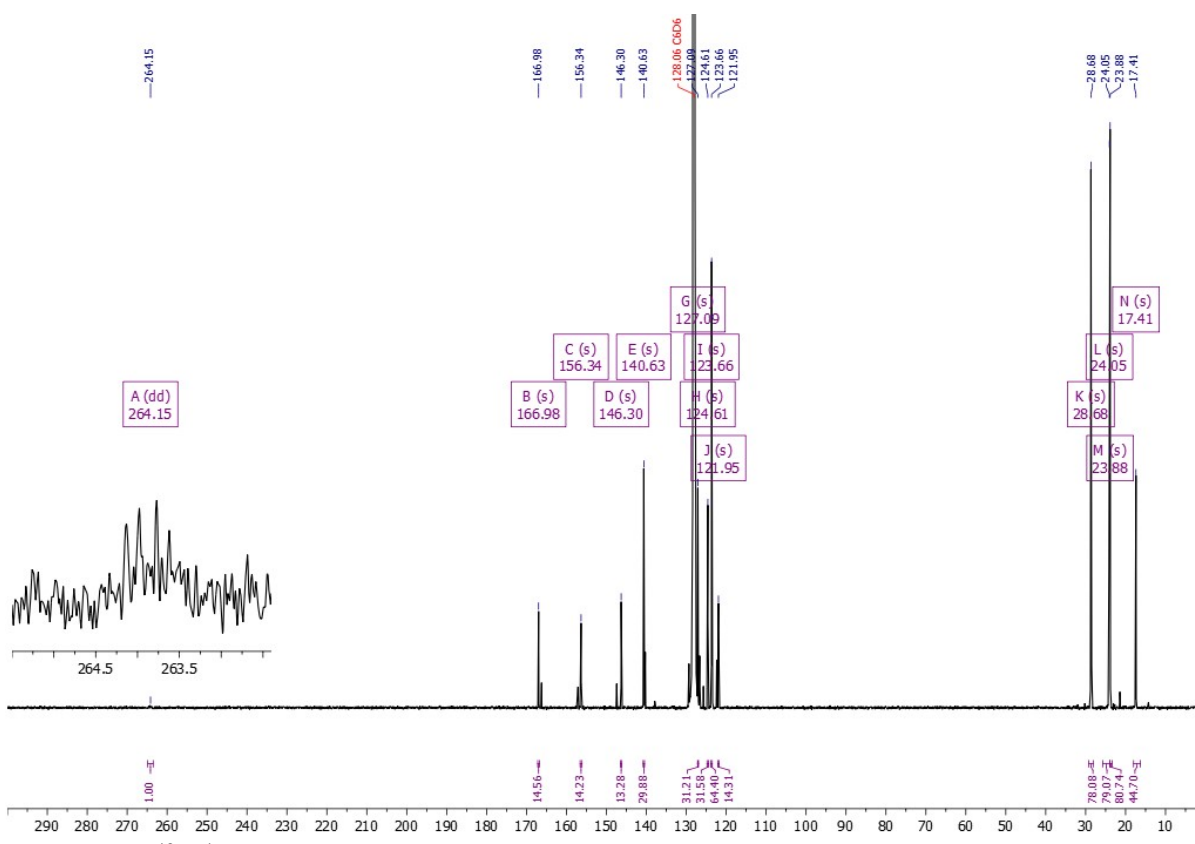
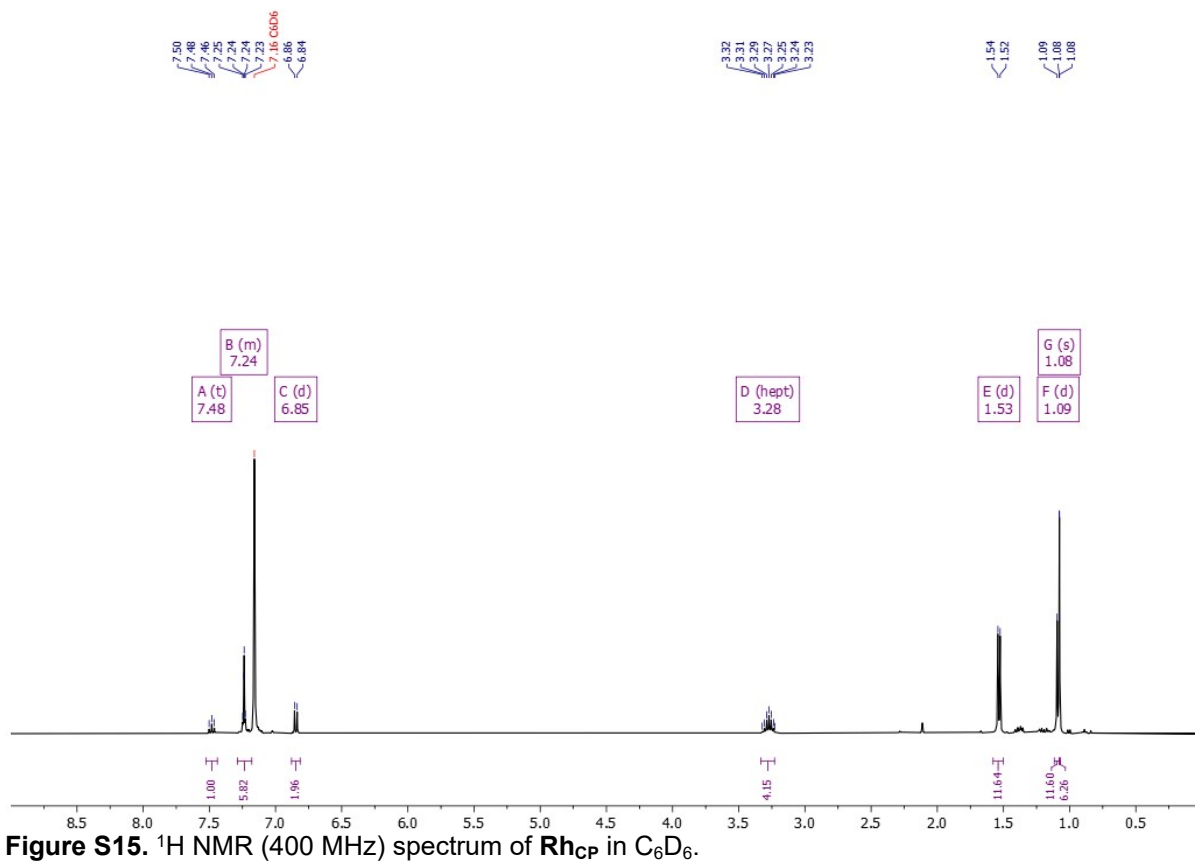
Mg(^{Dipp}Nacnac)(dioxane)(CP) (approx. 65 mg, 0.11 mmol) was generated *in situ* in toluene (1 mL). Rh(^{Dipp}PDI)Cl (62 mg, 0.10 mmol) was added as a solid to the solution of Mg(^{Dipp}Nacnac)(dioxane)(CP), and the mixture stirred at room temperature for 3 days. The mixture was filtered, and the solvent removed from the filtrate *in vacuo*. The residue was washed with hexane (3 × 1 mL), then extracted with toluene (1 mL). The dark green solution was concentrated *in vacuo*, then layered with hexane and stored at -35 °C for 3 days, yielding Rh(^{Dipp}PDI)(CP) as green-black crystals. The crystals were isolated by filtration, and washed with cold hexane (2 × 0.5 mL). Yield: 14 mg, 0.02 mmol, 22%. Anal. Calcd. (%) for C₃₄H₄₃N₃PRh: C, 65.07; H, 6.91; N, 6.70. Found: C, 63.69; H, 5.91; N, 5.65.

¹H NMR (400 MHz, C₆D₆): δ(ppm) 7.48 (t, ³J_{H-H} = 7.9, 1H, pyridine *para* CH), 7.26–7.22 (m, 6H, Dipp *para/meta* CH), 6.85 (d, ³J_{H-H} = 7.9, 2H, pyridine *meta* CH), 3.28 (sept, ³J_{H-H} = 6.8 Hz, 4H, Dipp CH(CH₃)₂), 1.53 (d, ³J_{H-H} = 6.8 Hz, 12H, Dipp CH(CH₃)₂), 1.09 (d, ³J_{H-H} = 6.8 Hz, 12H, Dipp CH(CH₃)₂), 1.09 (s, 6H, imine NCCH₃).

¹³C{¹H} NMR (151 MHz, C₆D₆): δ(ppm) 264.15 (dd, ¹J_{C-Rh} = 54.8 Hz, ¹J_{C-P} = 22.9 Hz, RhCP), 166.98 (s, imine NCCH₃), 156.34 (s, Dipp *ipso* C), 146.30 (s, Dipp *ortho* C), 140.63 (s, Dipp *para* C), 127.01 (s, Dipp *meta* C), 124.61 (s, pyridine *meta* C), 123.59 (s, pyridine *ortho* C), 121.61 (s, pyridine *para* C), 28.68 (s, Dipp CH(CH₃)₂), 24.05 s, Dipp CH(CH₃)₂), 23.88 (s, Dipp CH(CH₃)₂), 17.41 (s, imine NCCH₃).

³¹P{¹H} NMR (162 MHz, C₆D₆): δ(ppm) 251.4 (d, ²J_{P-Rh} = 6 Hz, CP).

Raman: 1334 cm⁻¹ (m, ν(C≡P)).



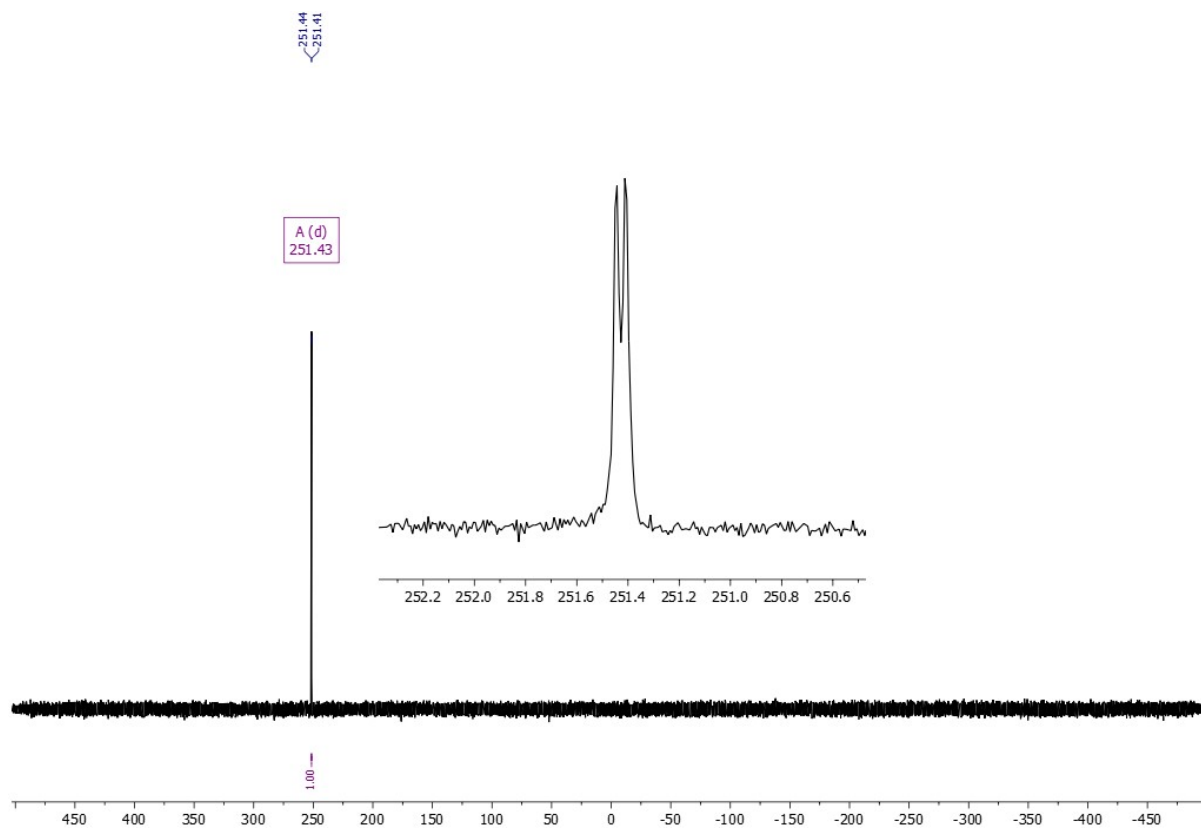


Figure S17. $^{31}\text{P}\{^1\text{H}\}$ NMR (162 MHz) spectrum of Rh_{CP} in C_6D_6 .

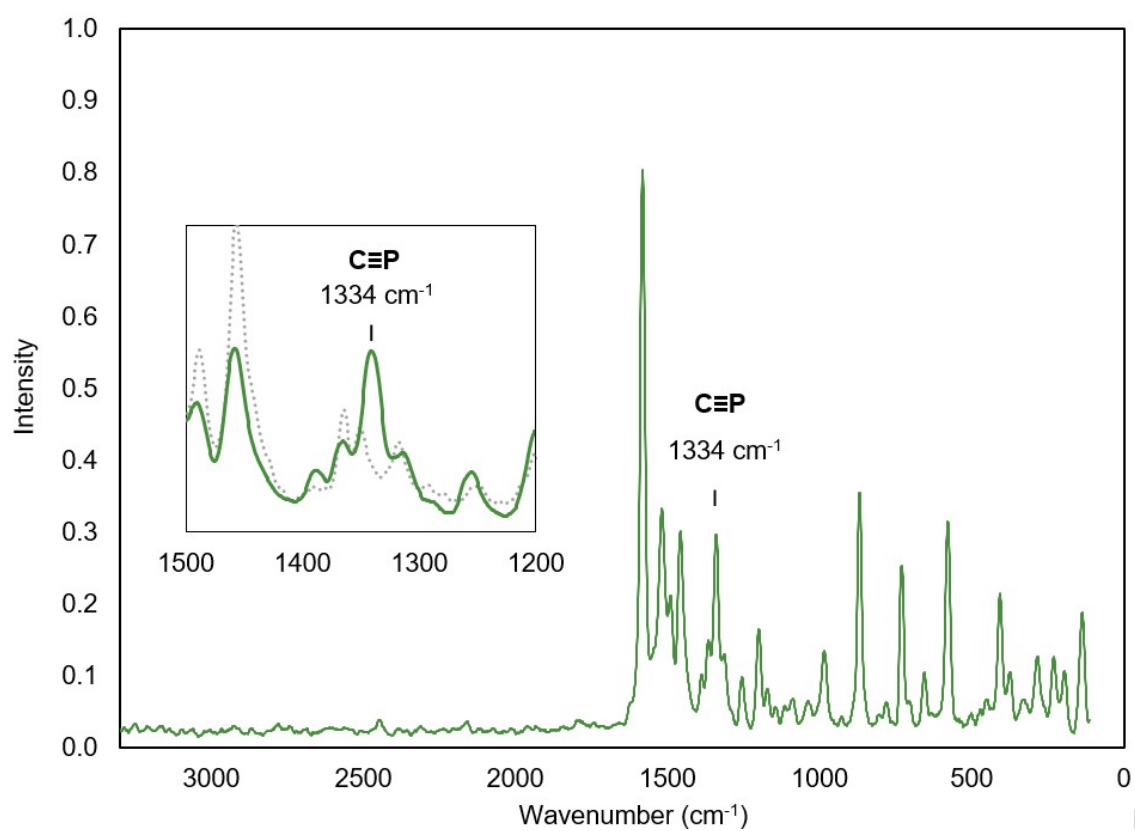


Figure S18. Dispersive Raman spectrum of Rh_{CP} . For comparison, the Raman spectrum of $\text{Rh}(\text{DippPDI})\text{Cl}$ between 1200–1500 cm^{-1} is shown as a dotted line in the inset.

1.2.7 Synthesis of Rh^(DippPDI)(CCH) (Rh_{CCH})

Rh^(DippPDI)Cl (100 mg, 0.16 mmol) was dissolved in THF (10 mL). Ethynylmagnesium chloride (0.7 mL, 0.25 M in THF, 0.18 mmol) was added dropwise, and stirred for 3 days. This was then filtered, and the solvent removed under reduced pressure to give Rh^(DippPDI)(CCH) as a green solid. Yield: 60 mg, 0.10 mmol, 61%. Anal. Calcd. (%) for C₃₅H₄₄N₃Rh: C, 68.95; H, 7.27; N, 6.89. Found: C, 66.89; H, 6.37; N, 6.10. Crystals suitable for X-ray diffraction were obtained from toluene/pentane by vapor diffusion.

¹H NMR (600 MHz, C₆D₆): δ(ppm) 7.78 (t, ³J_{H-H} = 7.9, 1H, pyridine *para* CH), 7.25–7.22 (m, 6H, Dipp *para/meta* CH), 6.97 (d, ³J_{H-H} = 7.9, 2H, pyridine *meta* CH), 3.27 (sept, ³J_{H-H} = 6.8 Hz, 4H, Dipp CH(CH₃)₂), 3.03 (d, ³J_{H-Rh} = 1.3 Hz, 1H, CCH), 1.42 (d, ³J_{H-H} = 6.8 Hz, 12H, Dipp CH(CH₃)₂), 1.12 (d, ³J_{H-H} = 6.8 Hz, 12H, Dipp CH(CH₃)₂), 1.04 (s, 6H, imine NCCH₃).

¹³C{¹H} NMR (151 MHz, C₆D₆): δ(ppm) 166.35 (s, imine NCCH₃), 156.41 (d, ²J_{C-Rh} = 2.8 Hz, Dipp *ipso* C), 148.37 (s, Dipp *ortho* C), 140.41 (s, Dipp *para* C), 126.52 (s, Dipp *meta* C), 125.00 (s, pyridine *meta* C), 123.50 (s, pyridine *ortho* C), 123.49 (d, ²J_{C-Rh} = 11.3 Hz, CCH), 122.94 (s, pyridine *para* C), 114.28 (d, ¹J_{C-Rh} = 60.6 Hz, CCH), 28.57 (s, Dipp CH(CH₃)₂), 23.96 (s, Dipp CH(CH₃)₂), 23.81 (s, Dipp CH(CH₃)₂), 17.58 (d, ³J_{C-Rh} = 1.5 Hz imine NCCH₃).

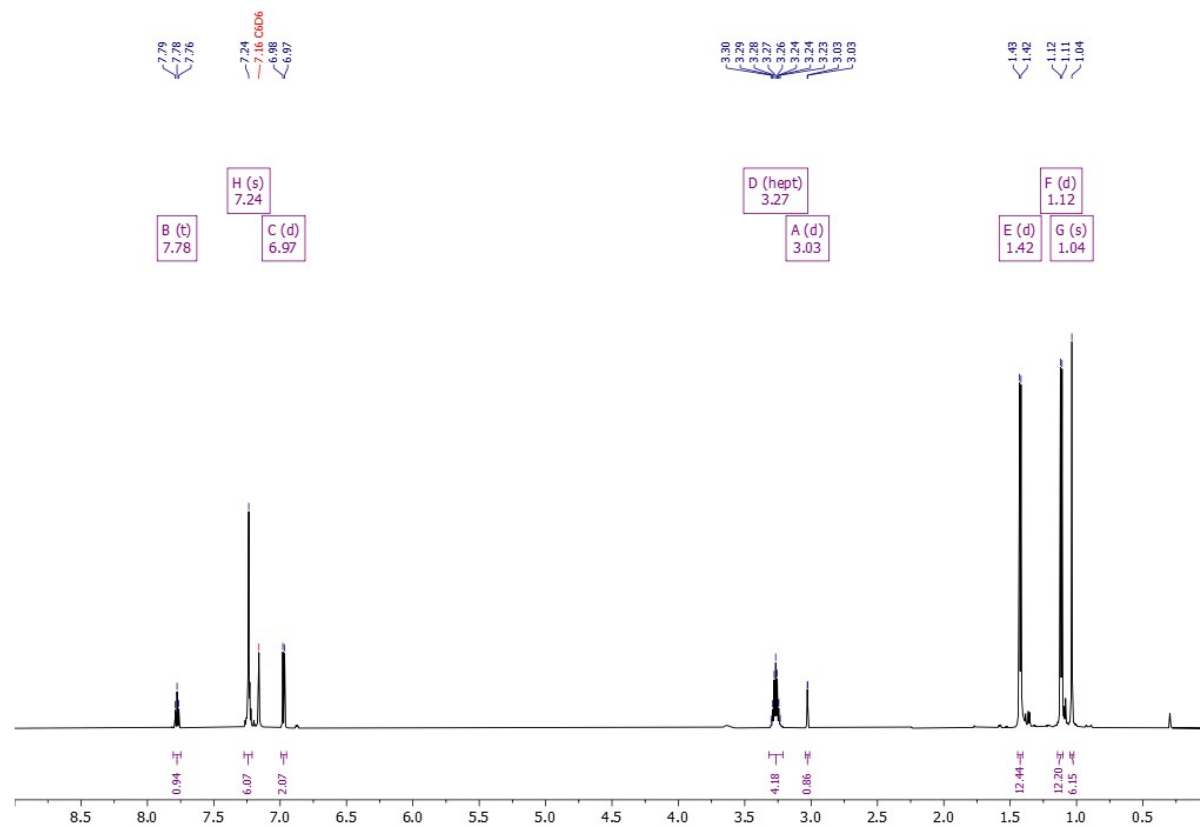


Figure S19. ¹H NMR (600 MHz) spectrum of Rh_{CCH} in C₆D₆.

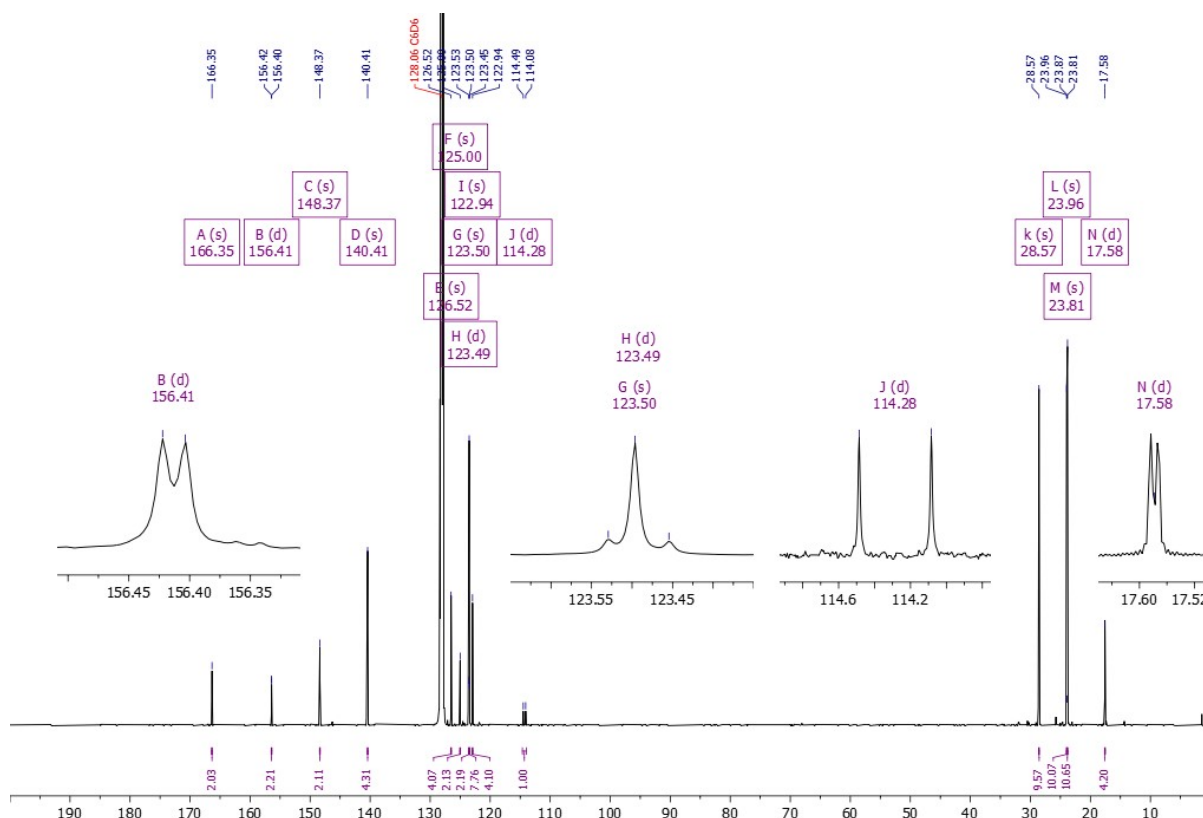


Figure S20. $^{13}\text{C}\{^1\text{H}\}$ NMR (151 MHz) spectrum of Rh_{CCH} in C_6D_6 .

1.2.8 Synthesis of $[\text{Rh}(\text{DippPDI})(\text{CO})][\text{BAR}^{\text{F}}_4]$ (Rh_{CO^+})

$\text{Rh}(\text{DippPDI})\text{Cl}$ (100 mg, 0.16 mmol) and $\text{Na}(\text{BAR}^{\text{F}}_4)$ (144 mg, 0.16 mmol) were dissolved in 1,2-DFB (3 mL). The solution was degassed, then placed under CO gas (1 bar). After stirring for 1 hour, the solution was degassed then filtered. The solution was concentrated, then layered with pentane (30 mL) for one week. After filtration, $[\text{Rh}(\text{DippPDI})(\text{CO})][\text{BAR}^{\text{F}}_4]$ was obtained as large dark green crystals. Yield: 181 mg, 0.12 mmol, 76%. Anal. Calcd. (%) for $\text{C}_{66}\text{H}_{55}\text{N}_3\text{BF}_{24}\text{ORh}$: C, 53.71; H, 3.76; N, 2.85. Found: C, 53.39; H, 3.68; N, 2.74.

^1H NMR (600 MHz, 1,2-DFB/ C_6D_6): δ (ppm) 8.17–8.09 (m, 8H, BAR^{F}_4 *ortho* CH) 7.86 (t, $^3J_{\text{H-H}} = 8.1$, 1H, pyridine *para* CH), 7.63 (d, $^3J_{\text{H-H}} = 8.1$, 2H, pyridine *meta* CH), 7.49 (bs, 4H, BAR^{F}_4 *para* CH), 3.16 (sept, $^3J_{\text{H-H}} = 6.8$ Hz, 4H, Dipp CH(CH_3)₂), 1.97 (s, 6H, imine NCCH_3), 1.26 (d, $^3J_{\text{H-H}} = 6.8$ Hz, 12H, Dipp CH(CH_3)₂), 1.08 (d, $^3J_{\text{H-H}} = 6.8$ Hz, 12H, Dipp CH(CH_3)₂). The signals for some aromatic protons could not be located due to overlap with 1,2-DFB solvent peaks.

$^{13}\text{C}\{^1\text{H}\}$ NMR (151 MHz, 1,2-DFB/ C_6D_6): δ (ppm) 187.42 (d, $^1J_{\text{C-Rh}} = 77.2$ Hz, CO), 176.19 (s, imine NCCH_3), 162.59 (q, $^1J_{\text{C-B}} = 49.7$ Hz, BAR^{F}_4 *ipso* C), 156.04 (d, $^2J_{\text{C-Rh}} = 3.1$ Hz, Dipp *ipso* C), 145.21 (s, Dipp *ortho* C), 142.26 (s, pyridine *para* C), 137.77 (s, ArC), 135.14 (bs, BAR^{F}_4 *ortho* C), 129.75 (qq, $^2J_{\text{C-F}} = 31.6$ Hz, $^2J_{\text{C-B}} = 2.9$ Hz, BAR^{F}_4 *meta* C), 128.79 (s, ArC), 125.85 (s, pyridine *meta* C), 117.70–117.58 (m, BAR^{F}_4 *para* C), 28.71 (s, Dipp CH(CH_3)₂), 22.78 (s, Dipp CH(CH_3)₂), 22.72 (s, Dipp CH(CH_3)₂), 16.44 (d, $^3J_{\text{C-Rh}} = 1.8$ Hz, imine NCCH_3). The

signals for some aromatic carbons could not be located or were not assigned due to overlap with 1,2-DFB solvent peaks.

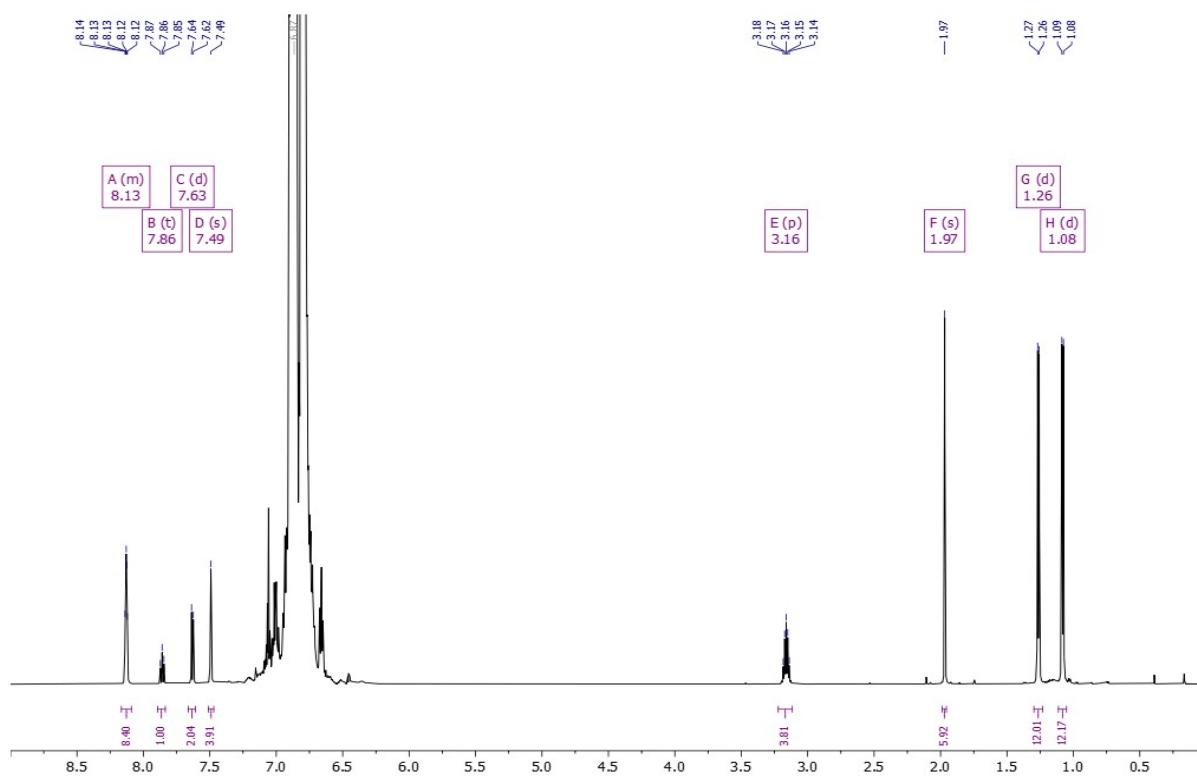


Figure S21. ^1H NMR (600 MHz) spectrum of RhCO^+ in 1,2-DFB, locked to a C_6D_6 capillary.

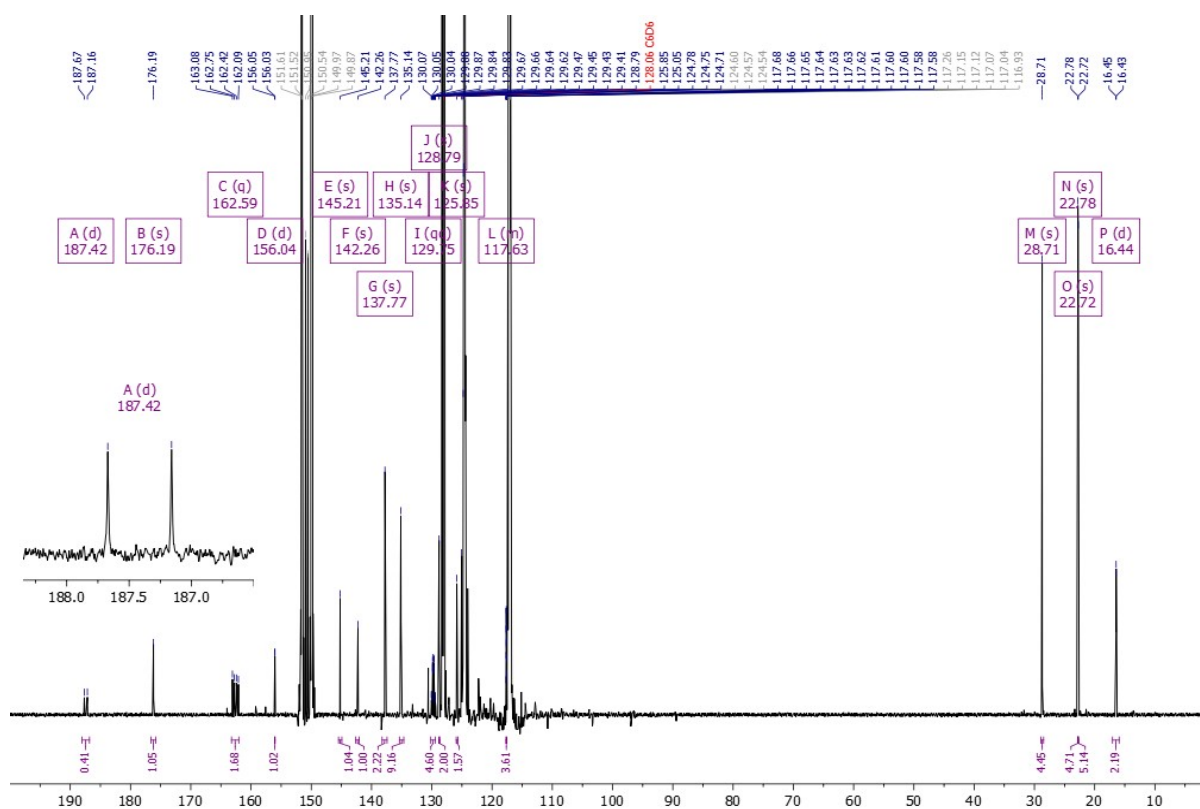
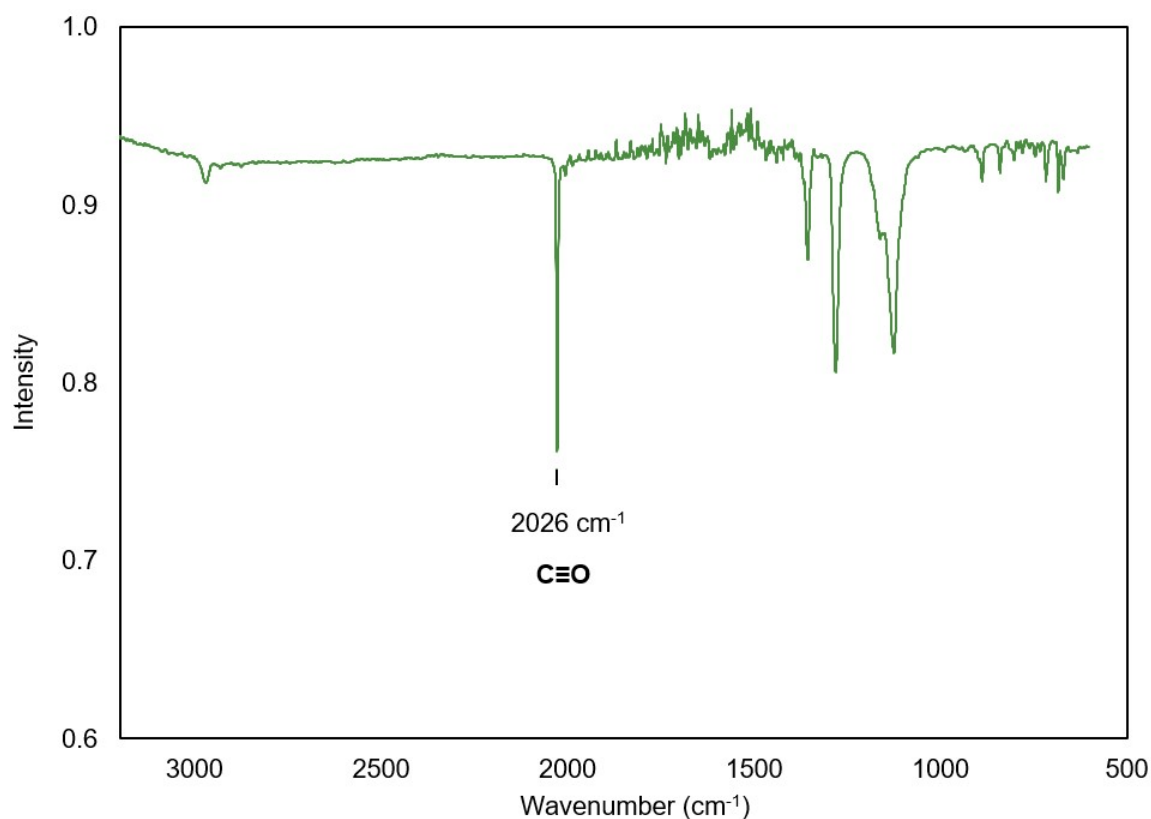


Figure S22. $^{13}\text{C}\{^1\text{H}\}$ NMR (600 MHz) spectrum of RhCO^+ in 1,2-DFB, locked to a C_6D_6 capillary.



Fig

re S23. ATR-FTIR spectrum of RhCO^+ .

1.2.9 Synthesis of $[\text{Rh}(\text{DippPDI})(\text{CN}^t\text{Bu})][\text{BARF}_4]$ ($\text{Rh}_{\text{CNBu}^+}$)

$\text{Rh}(\text{DippPDI})\text{Cl}$ (50 mg, 0.08 mmol) and $\text{Na}(\text{BARF}_4)$ (72 mg, 0.08 mmol) were dissolved in 1,2-DFB (3 mL). A solution of $^t\text{BuNC}$ (7 mg, 0.08 mmol) in DFB (0.5 mL) was added dropwise. The reaction mixture was stirred for 3 days, then filtered. The filtrate was concentrated, then layered with pentane (30 mL) for one week. After filtration, $[\text{Rh}(\text{DippPDI})(\text{CN}^t\text{Bu})][\text{BARF}_4]$ was obtained as dark green crystals. Yield: 101 mg, 0.07 mmol, 82%. Anal. Calcd. (%) for $\text{C}_{70}\text{H}_{64}\text{N}_4\text{BF}_{24}\text{Rh}$: C, 54.92; H, 4.21; N, 3.66. Found: C, 54.17; H, 3.60; N, 2.79.

^1H NMR (600 MHz, 1,2-DFB/ C_6D_6): δ (ppm) 8.18–8.12 (m, 8H, BARF_4 *ortho* CH) 7.73 (t, $^3J_{\text{H-H}} = 8.1$, 1H, pyridine *para* CH), 7.50 (bs, 4H, BARF_4 *para* CH), 7.46 (d, $^3J_{\text{H-H}} = 8.1$, 2H, pyridine *meta* CH), 3.06 (sept, $^3J_{\text{H-H}} = 6.9$ Hz, 4H, Dipp CH(CH_3)₂), 1.79 (s, 6H, imine NCCH₃), 1.17 (d, $^3J_{\text{H-H}} = 6.9$ Hz, 12H, Dipp CH(CH_3)₂), 1.07 (d, $^3J_{\text{H-H}} = 6.9$ Hz, 12H, Dipp CH(CH_3)₂), 0.70 (s, 9H, CNC(CH_3)₃). The signals for some aromatic protons could not be located due to overlap with 1,2-DFB solvent peaks.

$^{13}\text{C}\{^1\text{H}\}$ NMR (151 MHz, 1,2-DFB/ C_6D_6): δ (ppm) 178.60 (d, $^1J_{\text{C-Rh}} = 43.8$ Hz, CN t Bu), 172.01 (d, $^2J_{\text{C-Rh}} = 1.6$ Hz, imine NCCH₃), 162.59 (q, $^1J_{\text{C-B}} = 49.8$ Hz, BARF_4 *ipso* C), 156.01 (d, $^2J_{\text{C-Rh}} = 3.2$ Hz, Dipp *ipso* C), 146.13 (s, Dipp *ortho* C), 138.58 (s, ArC), 137.42 (s, ArC), 135.14 (bs, BARF_4 *ortho* C), 130.29–129.35 (m, BARF_4 *meta* C), 127.65 (s, ArC), 125.85 (s, ArC), 117.71–

117.58 (m, BARF_4 *para* C), 56.95 (s, $\text{CNC}(\text{CH}_3)_3$), 29.27 (s, $\text{CNC}(\text{CH}_3)_3$), 28.47 (s, Dipp $\text{CH}(\text{CH}_3)_2$), 23.00 (s, Dipp $\text{CH}(\text{CH}_3)_2$), 22.77 (s, Dipp $\text{CH}(\text{CH}_3)_2$), 16.05 (s, imine NCCH_3). The signals for some aromatic carbons could not be located or were not assigned due to overlap with 1,2-DFB solvent peaks.

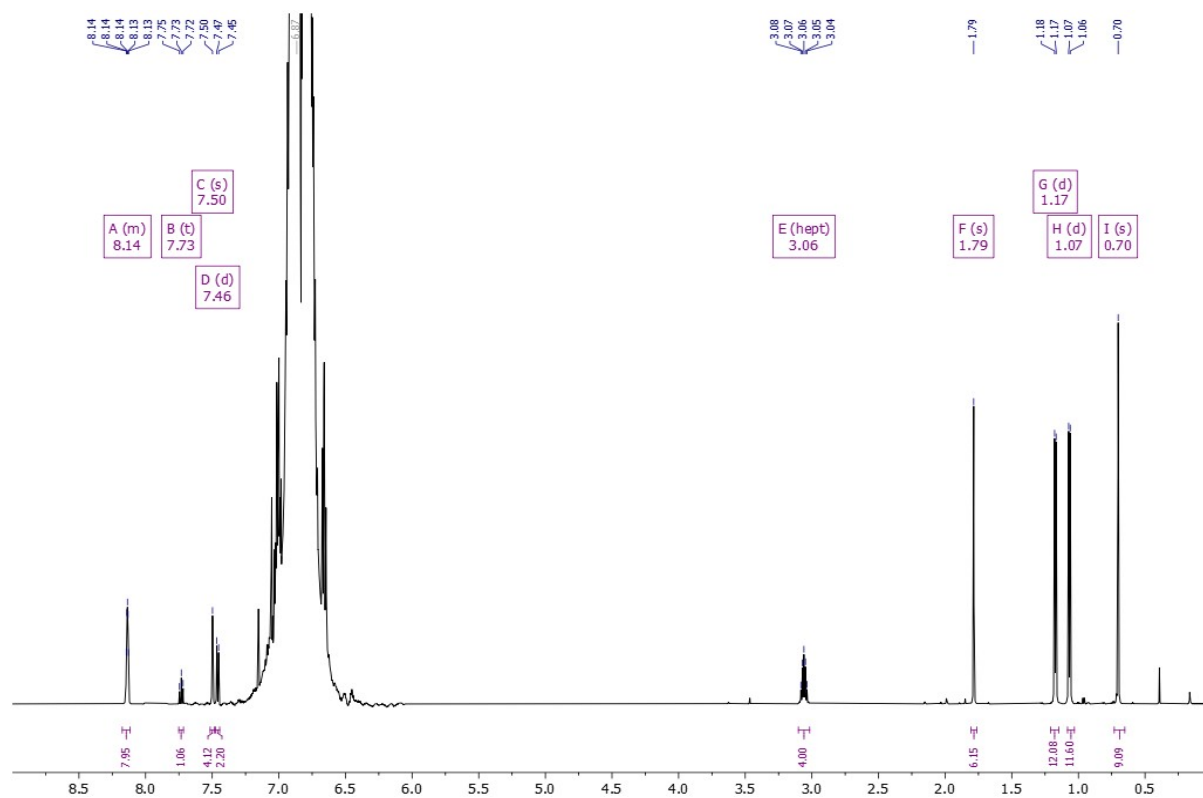


Figure S24. ^1H NMR (600 MHz) spectrum of $\text{Rh}_{\text{CNBu}}^+$ in 1,2-DFB, locked to a C_6D_6 capillary.

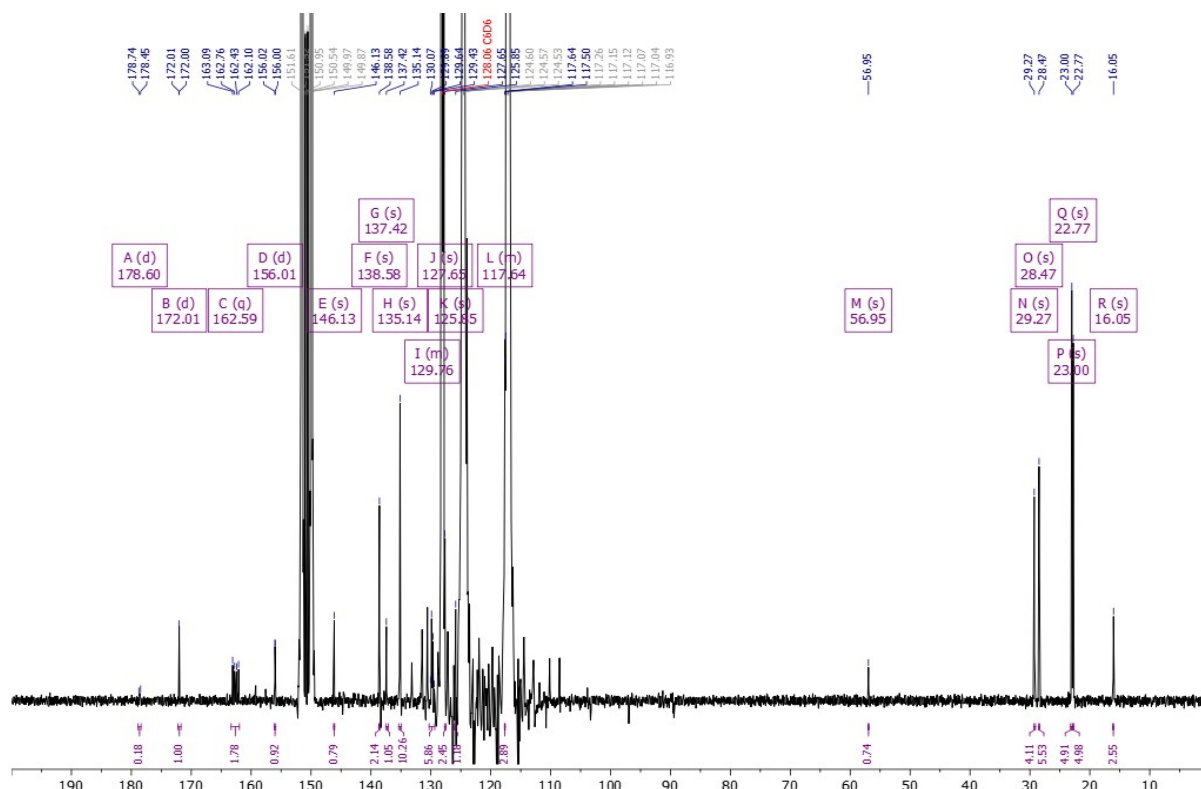


Figure S25. $^{13}\text{C}\{^1\text{H}\}$ NMR (600 MHz) spectrum of Rh_{CNU}^+ in 1,2-DFB, locked to a C_6D_6 capillary.

1.2.10 Synthesis of $[\text{Rh}(\text{DippPDI})(\text{C}_2\text{H}_4)][\text{BAR}^{\text{F}_4}]$ ($\text{Rh}_{\text{ethene}}^+$)

$[\text{Rh}(\text{DippPDI})(\text{C}_2\text{H}_4)][\text{BAR}^{\text{F}_4}]$ was synthesized using a modified literature procedure.⁷ $\text{Rh}(\text{DippPDI})\text{Cl}$ (50 mg, 0.08 mmol) and $\text{Na}(\text{BAR}^{\text{F}_4})$ (72 mg, 0.08 mmol) were dissolved in 1,2-DFB (3 mL). The solution was degassed, then placed under ethylene gas (1 bar). After stirring for 2 hours, the solution was degassed then filtered. The solution was concentrated, then layered with pentane (20 mL) for one week. After filtration, $[\text{Rh}(\text{DippPDI})(\text{C}_2\text{H}_4)][\text{BAR}^{\text{F}_4}]$ was obtained as large dark crystals suitable for X-ray diffraction. Yield: 114 mg, 0.08 mmol, 96%. ^1H NMR (600 MHz, 1,2-DFB/ C_6D_6): δ (ppm) 8.16–8.12 (m, 8H, BAR^{F_4} *ortho* CH) 7.88 (t, $^3J_{\text{H-H}} = 8.1$, 1H, pyridine *para* CH), 7.61 (d, $^3J_{\text{H-H}} = 8.1$, 2H, pyridine *meta* CH), 7.49 (bs, 4H, BAR^{F_4} *para* CH), 3.62 (d, $^2J_{\text{H-Rh}} = 1.6$ Hz, 4H, C_2H_4), 2.93 (sept, $^3J_{\text{H-H}} = 6.8$ Hz, 4H, Dipp CH(CH_3)₂), 1.85 (s, 6H, imine NCCH_3), 1.17 (d, $^3J_{\text{H-H}} = 6.9$ Hz, 12H, Dipp CH(CH_3)₂), 0.96 (d, $^3J_{\text{H-H}} = 6.9$ Hz, 12H, Dipp CH(CH_3)₂). The signals for some aromatic protons could not be located due to overlap with 1,2-DFB solvent peaks.

$^{13}\text{C}\{^1\text{H}\}$ NMR (151 MHz, 1,2-DFB/ C_6D_6): δ (ppm) 174.84 (s, imine NCCH_3), 162.58 (q, $^1J_{\text{C-B}} = 49.8$ Hz, BAR^{F_4} *ipso* C), 155.40 (d, $^2J_{\text{C-Rh}} = 2.9$ Hz, Dipp *ipso* C), 141.62 (s, Dipp *ortho* C), 139.72 (s, ArC), 138.98 (s, ArC), 135.14 (bs, BAR^{F_4} *ortho* C), 129.75 (qq, $^2J_{\text{C-F}} = 31.5$ Hz, $^2J_{\text{C-B}} = 3.0$ Hz, BAR^{F_4} *meta* C), 125.85 (s, ArC), 117.72–117.56 (m, BAR^{F_4} *para* C), 81.80 (d, $^1J_{\text{C-Rh}} = 10.1$ Hz, C_2H_4), 28.41 (s, Dipp CH(CH_3)₂), 23.57 (s, Dipp CH(CH_3)₂), 22.59 (s, Dipp

CH(CH₃)₂, 18.05 (s, imine NCCH₃). The signals for some aromatic carbons could not be located or were not assigned due to overlap with 1,2-DFB solvent peaks.

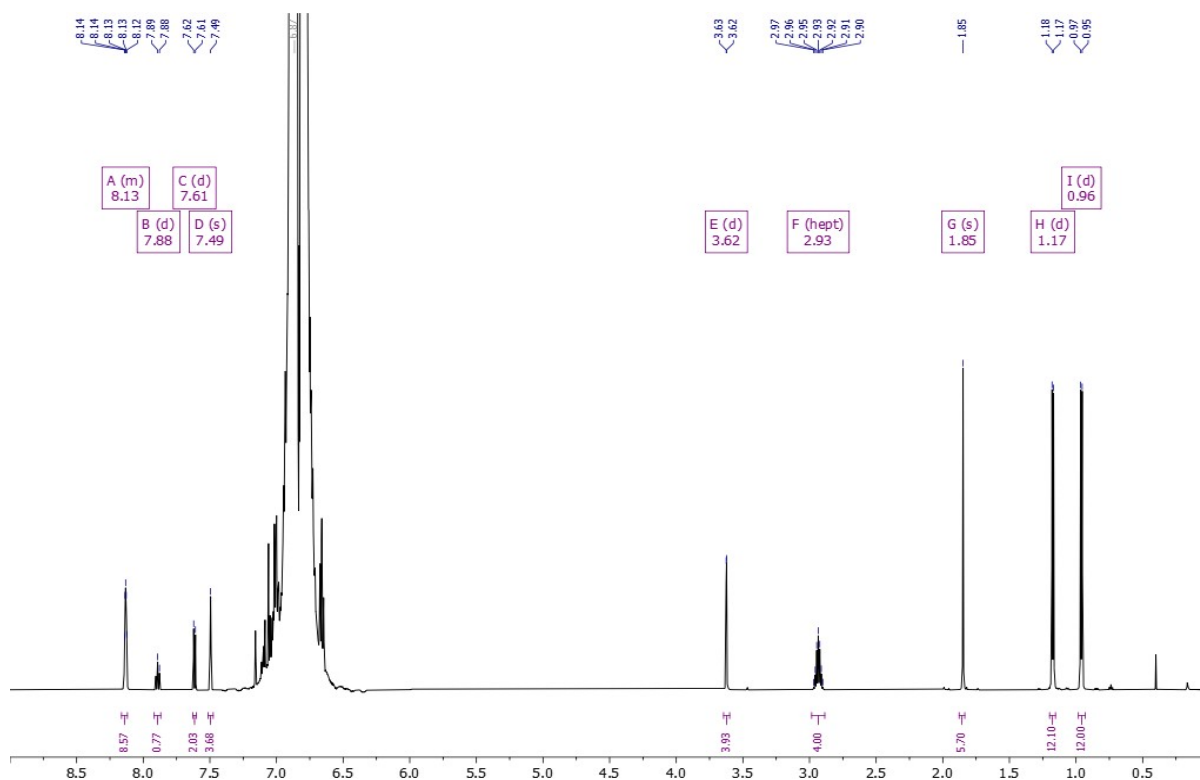


Figure S26. ¹H NMR (600 MHz) spectrum of Rh_{ethylene}⁺ in 1,2-DFB, locked to a C₆D₆ capillary.

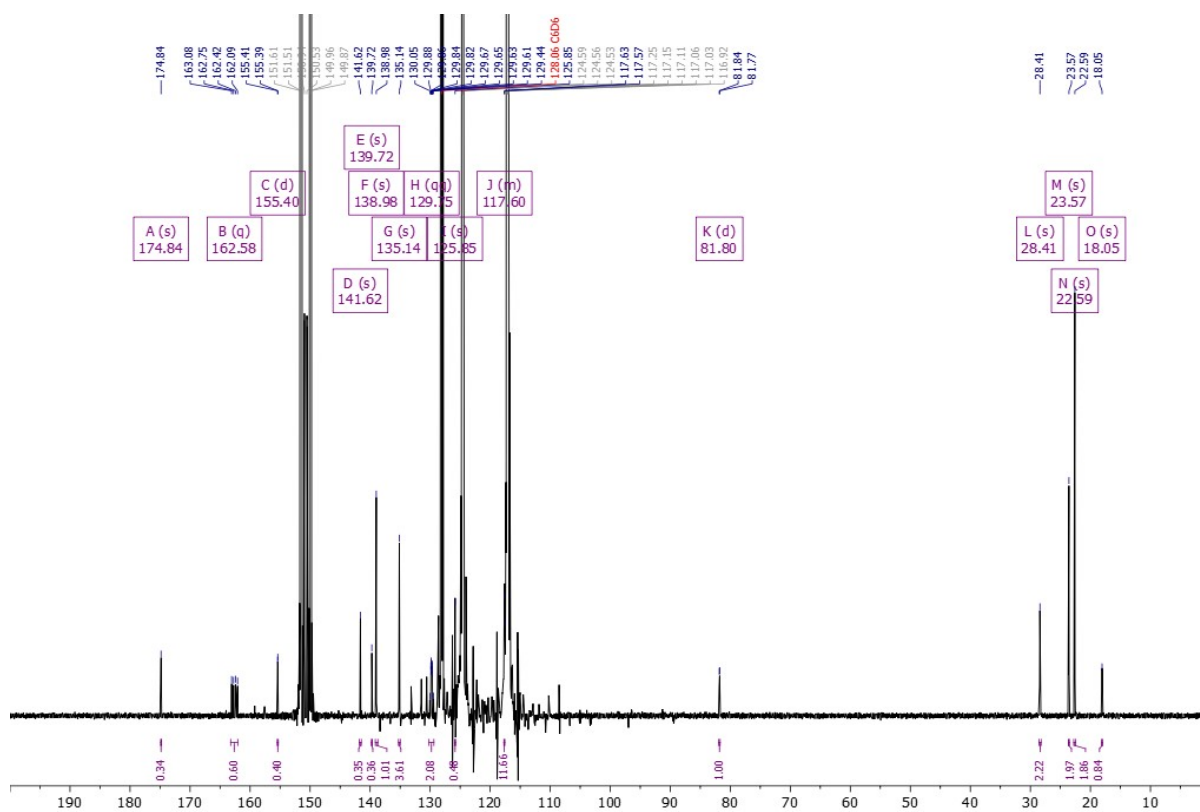


Figure S27. ¹³C{¹H} NMR (600 MHz) spectrum of Rh_{ethylene}⁺ in 1,2-DFB with a C₆D₆ capillary.

1.2.11 Attempted syntheses of $\text{Co}(\text{DippPDI})(\text{CN})$ (Co_{CN}) and $\text{Rh}(\text{DippPDI})(\text{CN})$ (Rh_{CN})

Method A: $\text{M}(\text{DippPDI})\text{Cl}$ ($\text{M} = \text{Co}, \text{Rh}$) (1 eq.) and KCN (1 eq.) were suspended in THF. The reaction mixture was heated to reflux for 3 days, after which ^1H NMR spectroscopy showed only unreacted starting material.

Method B: $\text{M}(\text{DippPDI})\text{Cl}$ ($\text{M} = \text{Co}, \text{Rh}$) (1 eq.) and KCN (1 eq.) and 18-crown-6 (1 eq.) were suspended in THF. The reaction mixture was heated to reflux for 3 days, after which ^1H NMR spectroscopy showed only unreacted starting material.

Method C: $\text{Rh}(\text{DippPDI})\text{Cl}$ (1 eq.) and KCN (1 eq.) were dissolved in methanol. The reaction mixture was stirred for 1 h, after which ^1H NMR spectroscopy showed a mixture of products including free DippPDI ligand.

Method D: $\text{M}(\text{DippPDI})\text{Cl}$ ($\text{M} = \text{Co}, \text{Rh}$) (1 eq.) was dissolved in toluene. A solution of Me_3SiCN in toluene (0.2 M, 1 eq.) was added dropwise at $-78\text{ }^\circ\text{C}$, resulting in discoloration of the solution to red ($\text{M} = \text{Co}$) or brown ($\text{M} = \text{Rh}$). After stirring overnight, ^1H NMR spectroscopy showed a mixture of products including free DippPDI ligand for $\text{M} = \text{Rh}$, and in the case of $\text{M} = \text{Co}$, unreacted $\text{Co}(\text{DippPDI})\text{Cl}$ as well as several paramagnetic species.

Method E: $\text{M}(\text{DippPDI})\text{Cl}$ ($\text{M} = \text{Co}, \text{Rh}$) (1 eq.) and NaBARF_4 (1 eq.) were dissolved in 1,2-DFB. A solution of $[\text{Bu}_4\text{N}]\text{CN}$ (1 eq.) in 1,2-DFB was added at $-35\text{ }^\circ\text{C}$, resulting in a color change to green ($\text{M} = \text{Co}$) or black ($\text{M} = \text{Rh}$). ^1H NMR spectroscopy showed a mixture of products, including unreacted $\text{M}(\text{DippPDI})\text{Cl}$.

Method F: $\text{Rh}(\text{DippPDI})(\text{C}_2\text{H}_4)$ (1 eq.) was dissolved in 1,2-DFB. A solution of $[\text{Bu}_4\text{N}]\text{CN}$ (1 eq.) in 1,2-DFB was added at $-35\text{ }^\circ\text{C}$, resulting in an initial color change to bright green, then black. ^1H NMR spectroscopy showed a mixture of products including unreacted $\text{Rh}(\text{DippPDI})\text{Cl}$.

1.3 Other characterization data

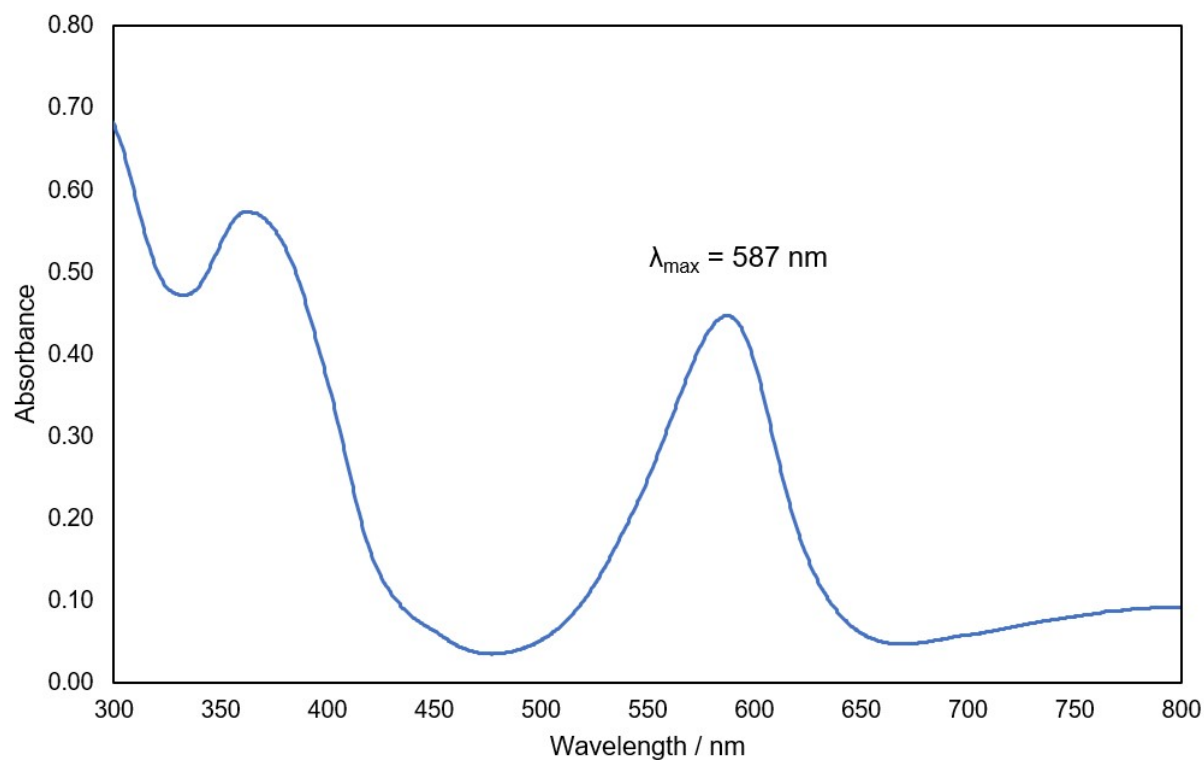


Figure S28. UV-vis absorption spectrum of $\text{Co}(\text{DiippPDI})(\text{CP})$ in toluene.

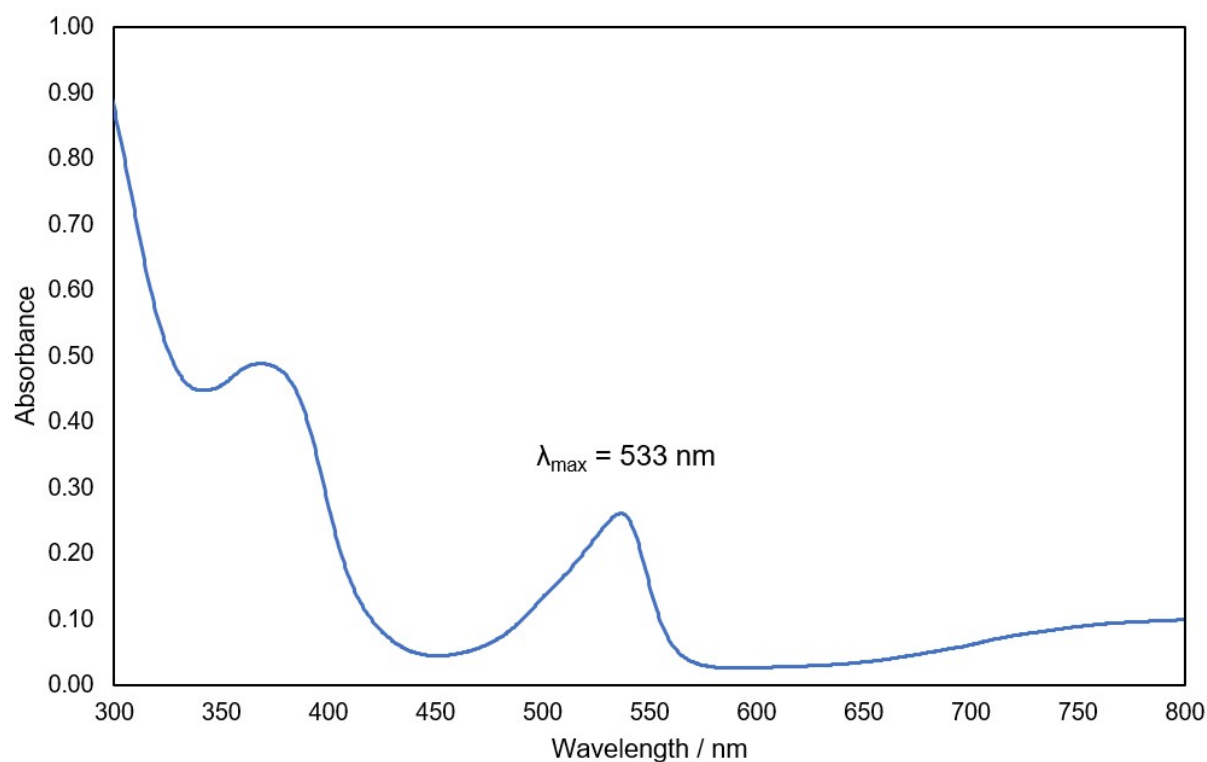


Figure S29. UV-vis absorption spectrum of $\text{Co}(\text{DiippPDI})\text{Cl}$ in toluene.

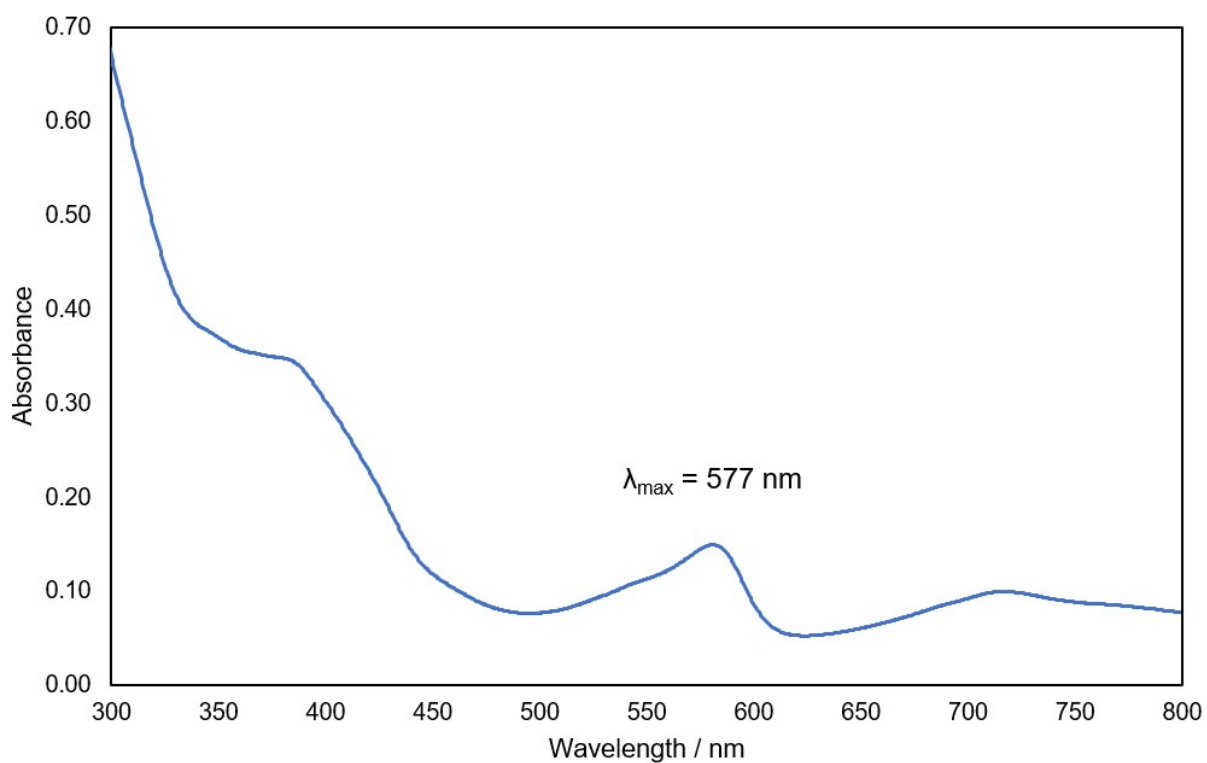


Figure S30. UV-vis absorption spectrum of $\text{Co}(\text{DiPPDI})\text{Me}$ in toluene.

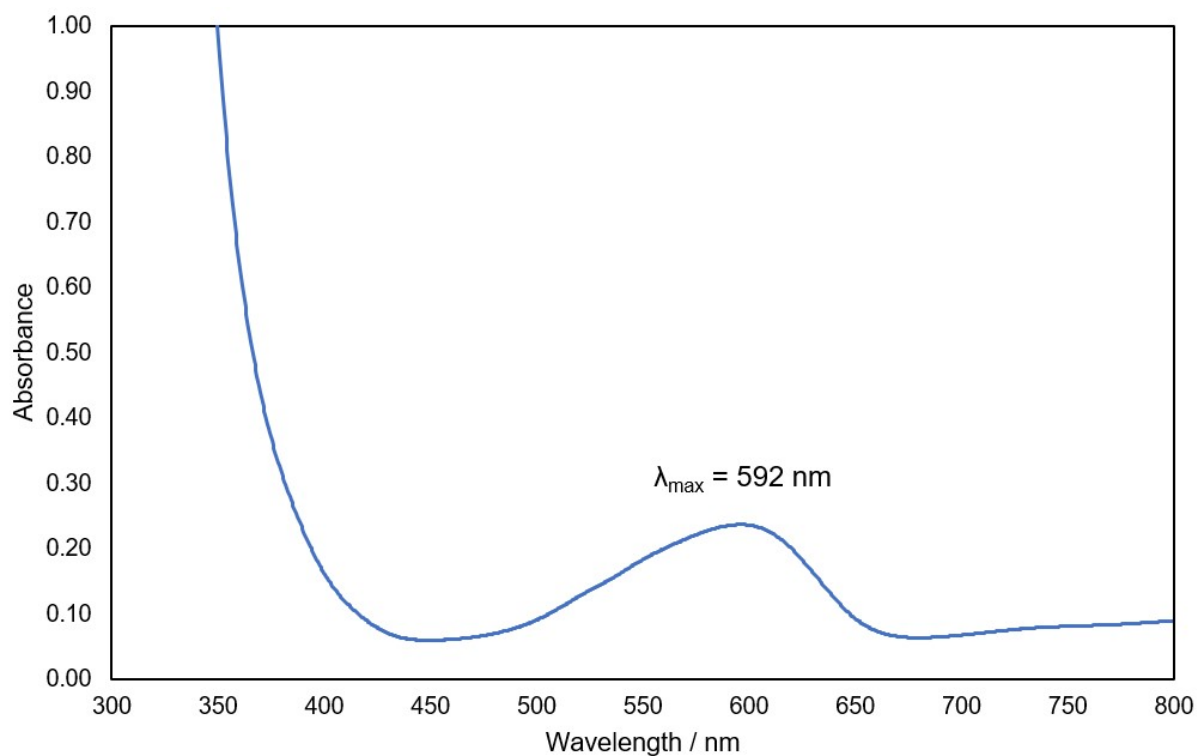


Figure S31. UV-vis absorption spectrum of $[\text{Co}(\text{DiPPDI})(\text{N}_2)][\text{B}(\text{Me})(\text{C}_6\text{F}_5)_3]$ in toluene.

2. Single crystal X-ray diffraction data

Single-crystal X-ray diffraction data were collected using an Oxford Diffraction Supernova dual-source diffractometer equipped with a 135 mm Atlas CCD area detector. Crystals were selected under Paratone-N oil, mounted on micro-mount loops and quench-cooled using an Oxford Cryosystems open flow N₂ cooling device. Data were collected at 150 K using mirror monochromated Cu K α ($\lambda = 1.54184$ Å) or Mo K α ($\lambda = 0.71073$ Å) radiation and processed using the CrysAlisPro package, including unit cell parameter refinement and inter-frame scaling (carried out using SCALE3 ABSPACK).⁸ Equivalent reflections were merged and diffraction patterns processed with the CrysAlisPro suite. Structures were subsequently solved using direct methods and refined on F^2 using the SHELXL package.⁹

Table S1. Selected X-ray data collection/refinement parameters for **Co_{CC}H**, Na(THF)Co(PIEA)(CCH) and **Co_{CO}⁺(BAR^F₄)⁻**.

	Co_{CC}H	Na(THF)Co(PIEA)(CCH)	Co_{CO}⁺(BAR^F₄)⁻
Formula	C ₃₅ H ₄₄ CoN ₃	C ₃₉ H ₅₁ CoN ₃ NaO	C ₆₆ H ₅₅ BCoF ₂₄ N ₃ O
CCDC	2242900	2242901	2242902
Fw [g mol ⁻¹]	565.66	659.74	1431.87
Crystal system	orthorhombic	monoclinic	monoclinic
Space group	<i>P</i> 2 ₁ 2 ₁ 2 ₁	<i>P</i> 2 ₁ / <i>c</i>	<i>P</i> 2 ₁ / <i>c</i>
<i>a</i> (Å)	8.47050(10)	11.78850(10)	17.4943(5)
<i>b</i> (Å)	17.9094(3)	16.6101(2)	17.8665(6)
<i>c</i> (Å)	20.2338(3)	18.5455(2)	22.1081(6)
α (°)	90	90	90
β (°)	90	99.7630(10)	104.528(3)
γ (°)	90	90	90
<i>V</i> (Å ³)	3069.50(8)	3578.77(7)	6689.2(4)
<i>Z</i>	4	4	4
Radiation, λ (Å)	Mo K α , 0.71073	Cu K α , 1.54184	Mo K α , 0.71073
Temp (K)	150(2)	150(2)	150(2)
ρ_{calc} (g cm ⁻³)	1.224	1.224	1.422
μ (mm ⁻¹)	0.586	4.125	0.367
Reflections collected	54167	78701	107320
Indep. reflections	8746	7475	15340
Parameters	367	418	1007
R(int)	0.0472	0.0465	0.0566
R1/wR2, ^[a] $I \geq 2\sigma I$ (%)	3.64/7.21	3.01/8.06	6.14/15.31
R1/wR2, ^[a] all data (%)	4.84/7.69	3.40/8.31	9.24/16.60
GOF	1.068	1.037	1.061

^[a] $R1 = \frac{\sum ||F_o| - |F_c||}{\sum |F_o|}$; $wR2 = \frac{\{\sum w[(F_o)^2 - (F_c)^2]^2\}^{1/2}}{\{\sum w(F_o)^2\}^{1/2}}$; $w = [\sigma^2(F_o)^2 + (AP)^2 + BP]^{-1}$, where $P = \frac{[(F_o)^2 + 2(F_c)^2]}{3}$ and the A and B values are 0.264 and 1.06 for **Co_{CC}H**, 0.456 and 1.0611 for Na(THF)Co(PIEA)(CCH), and 0.0642 and 9.16 for **Co_{CO}⁺(BAR^F₄)⁻**.

Table S2. Selected X-ray data collection/refinement parameters for $\text{Co}_{\text{CNBu}}^+(\text{BArF}_4)^-$, $\text{Co}_{2\text{CNBu}}^+(\text{BArF}_4)^-$ and $\text{Rh}_{\text{Cl}} \cdot 1.33\text{THF} \cdot 0.66\text{pent}$.

	$\text{Co}_{\text{CNBu}}^+(\text{BArF}_4)^-$	$\text{Co}_{2\text{CNBu}}^+(\text{BArF}_4)^-$	$\text{Rh}_{\text{Cl}} \cdot 1.33\text{THF} \cdot 0.66\text{pent}$
Formula	$\text{C}_{70}\text{H}_{64}\text{BCoF}_{24}\text{N}_4$	$\text{C}_{75}\text{H}_{73}\text{BCoF}_{24}\text{N}_5$	$\text{C}_{41.66}\text{H}_{61.66}\text{ClN}_3\text{O}_{1.33}\text{Rh}$
CCDC	2242903	2242904	2242905
Fw [g mol ⁻¹]	1486.99	1570.12	764.30
Crystal system	triclinic	triclinic	orthorhombic
Space group	<i>P</i> -1	<i>P</i> -1	<i>C</i> 222 ₁
<i>a</i> (Å)	14.3644(2)	12.9433(2)	17.36740(10)
<i>b</i> (Å)	15.5532(2)	15.1992(3)	29.7047(2)
<i>c</i> (Å)	16.5724(2)	20.7647(3)	23.95240(10)
α (°)	91.0850(10)	76.385(2)	90
β (°)	102.7870(10)	79.845(2)	90
γ (°)	99.3700(10)	87.162(2)	90
<i>V</i> (Å ³)	3556.66(8)	3907.87(12)	12356.88(12)
<i>Z</i>	2	2	12
Radiation, λ (Å)	Cu K α , 1.54184	Cu K α , 1.54184	Cu K α , 1.54184
Temp (K)	150(2)	150(2)	150(2)
ρ_{calc} (g cm ⁻³)	1.388	1.334	1.232
μ (mm ⁻¹)	2.835	2.613	4.200
Reflections collected	89994	44787	102303
Indep. reflections	14746	16152	12891
Parameters	954	1039	666
R(int)	0.0372	0.0355	0.0664
R1/wR2, ^[a] I $\geq 2\sigma$ I (%)	4.58/12.42	5.22/13.83	3.80/9.81
R1/wR2, ^[a] all data (%)	4.85/12.66	6.09/14.70	4.15/10.20
GOF	1.077	1.044	1.036

^[a] $R1 = \frac{[\sum ||F_o| - |F_c||]}{\sum |F_o|}$; $wR2 = \frac{\{[\sum w[(F_o)^2 - (F_c)^2]^2]\}}{[\sum w(F_o)^2]^{1/2}}$; $w = [\sigma^2(F_o)^2 + (AP)^2 + BP]^{-1}$, where $P = \frac{[(F_o)^2 + 2(F_c)^2]}{3}$ and the A and B values are 0.0663 and 1.48 for $\text{Co}_{\text{CNBu}}^+(\text{BArF}_4)^-$, 0.0818 and 0.98 for $\text{Co}_{2\text{CNBu}}^+(\text{BArF}_4)^-$, 0.0599 and 14.42 for $\text{Rh}_{\text{Cl}} \cdot 1.33\text{THF} \cdot 0.66\text{pent}$.

Table S3. Selected X-ray data collection/refinement parameters for **Rh_{Me}·0.25tol·0.25hex**, **Rh_{CP}**, **Rh_{CCH}**.

	Rh_{Me}·0.25tol·0.25hex	Rh_{CP}	Rh_{CCH}
Formula	C _{37.25} H _{51.5} N ₃ Rh	C ₃₄ H ₄₃ N ₃ PRh	C ₃₅ H ₄₄ N ₃ Rh
CCDC	2242906	2242907	2242908
Fw [g mol ⁻¹]	644.22	627.59	609.64
Crystal system	triclinic	orthorhombic	monoclinic
Space group	<i>P</i> -1	<i>P</i> 2 ₁ 2 ₁ 2 ₁	<i>P</i> 2 ₁ / <i>n</i>
<i>a</i> (Å)	16.0874(11)	8.49660(10)	10.43020(10)
<i>b</i> (Å)	16.5041(10)	17.9973(2)	24.0268(2)
<i>c</i> (Å)	17.1430(8)	20.3635(2)	12.31850(10)
α (°)	86.593(4)	90	90
β (°)	64.600(5)	90	93.2010(10)
γ (°)	61.518(7)	90	90
<i>V</i> (Å ³)	3553.1(4)	3113.90(6)	3082.25(5)
<i>Z</i>	4	4	4
Radiation, λ (Å)	Cu K _α , 1.54184	Cu K _α , 1.54184	Cu K _α , 1.54184
Temp (K)	150(2)	150(2)	150(2)
ρ _{calc} (g cm ⁻³)	1.204	1.339	1.314
μ (mm ⁻¹)	4.075	5.110	4.671
Reflections collected	39322	64682	17807
Indep. reflections	14641	6499	6385
Parameters	813	362	361
R(int)	0.0721	0.0453	0.0242
R1/wR2, ^[a] I ≥ 2σI (%)	5.74/14.90	2.14/5.62	2.92/7.41
R1/wR2, ^[a] all data (%)	7.42/16.93	2.25/5.69	3.02/7.48
GOF	1.031	1.068	1.102

^[a] R1 = $[\sum |F_o| - |F_c|] / \sum |F_o|$; wR2 = $\{[\sum w[(F_o)^2 - (F_c)^2]^2] / [\sum w(F_o)^2]\}^{1/2}$; w = $[\sigma^2(F_o)^2 + (AP)^2 + BP]^{-1}$, where P = $[(F_o)^2 + 2(F_c)^2] / 3$ and the A and B values are 0.0987 and 0.86 for **Rh_{Me}·0.25tol·0.25hex**, 0.036 and 0.80 for **Rh_{CP}**, 0.0398 and 2.42 for **Rh_{CCH}**.

Table S4. Selected X-ray data collection/refinement parameters for **Rh_{CO}⁺(BARF₄)⁻**, **Rh_{CNBu}⁺(BARF₄)⁻** and **Rh_{ethene}⁺(BARF₄)⁻**.

	Rh_{CO}⁺(BARF₄)⁻	Rh_{CNBu}⁺(BARF₄)⁻	Rh_{ethene}⁺(BARF₄)⁻
Formula	C ₆₆ H ₅₅ BF ₂₄ N ₃ ORh	C ₇₀ H ₆₄ BF ₂₄ N ₄ Rh	C ₆₇ H ₅₉ BF ₂₄ N ₃ Rh
CCDC	2242909	2242910	2242911
Fw [g mol ⁻¹]	1475.85	1530.97	1475.89
Crystal system	monoclinic	triclinic	monoclinic
Space group	<i>P</i> 2 ₁ / <i>c</i>	<i>P</i> -1	<i>P</i> 2 ₁ / <i>c</i>
<i>a</i> (Å)	17.5140(1)	14.4106(4)	17.5964(2)
<i>b</i> (Å)	17.7479(1)	15.5555(3)	17.6516(2)
<i>c</i> (Å)	22.3688(1)	16.6974(5)	22.6324(2)
α (°)	90	90.441(2)	90
β (°)	104.161(1)	103.544(2)	104.7830(10)
γ (°)	90	100.297(2)	90
<i>V</i> (Å ³)	6741.75(7)	3575.45(17)	6797.04(13)
<i>Z</i>	4	2	4
Radiation, λ (Å)	Cu K _α , 1.54184	Cu K _α , 1.54184	Cu K _α , 1.54184
Temp (K)	150(2)	150(2)	150(2)
ρ _{calc} (g cm ⁻³)	1.454	1.422	1.442
μ (mm ⁻¹)	3.031	2.871	2.994
Reflections collected	48569	39212	41283
Indep. reflections	13941	14755	13995
Parameters	935	914	935
R(int)	0.0325	0.0382	0.0288
R1/wR2, ^[a] I ≥ 2σI (%)	4.11/10.80	4.17/10.85	4.77/12.86
R1/wR2, ^[a] all data (%)	4.59/11.28	4.47/11.17	5.46/13.66
GOF	1.060	1.019	1.041

^[a] R1 = $[\sum ||F_o| - |F_c||] / \sum |F_o|$; wR2 = $\{[\sum w[(F_o)^2 - (F_c)^2]^2] / [\sum w(F_o)^2]\}^{1/2}$; w = $[\sigma^2(F_o)^2 + (AP)^2 + BP]^{-1}$, where P = $[(F_o)^2 + 2(F_c)^2] / 3$ and the A and B values are 0.0579 and 6.52 and for **Rh_{CO}⁺(BARF₄)⁻**, 0.0629 and 3.07 for **Rh_{CNBu}⁺(BARF₄)⁻**, and 0.0792 and 6.55 for **Rh_{ethene}⁺(BARF₄)⁻**.

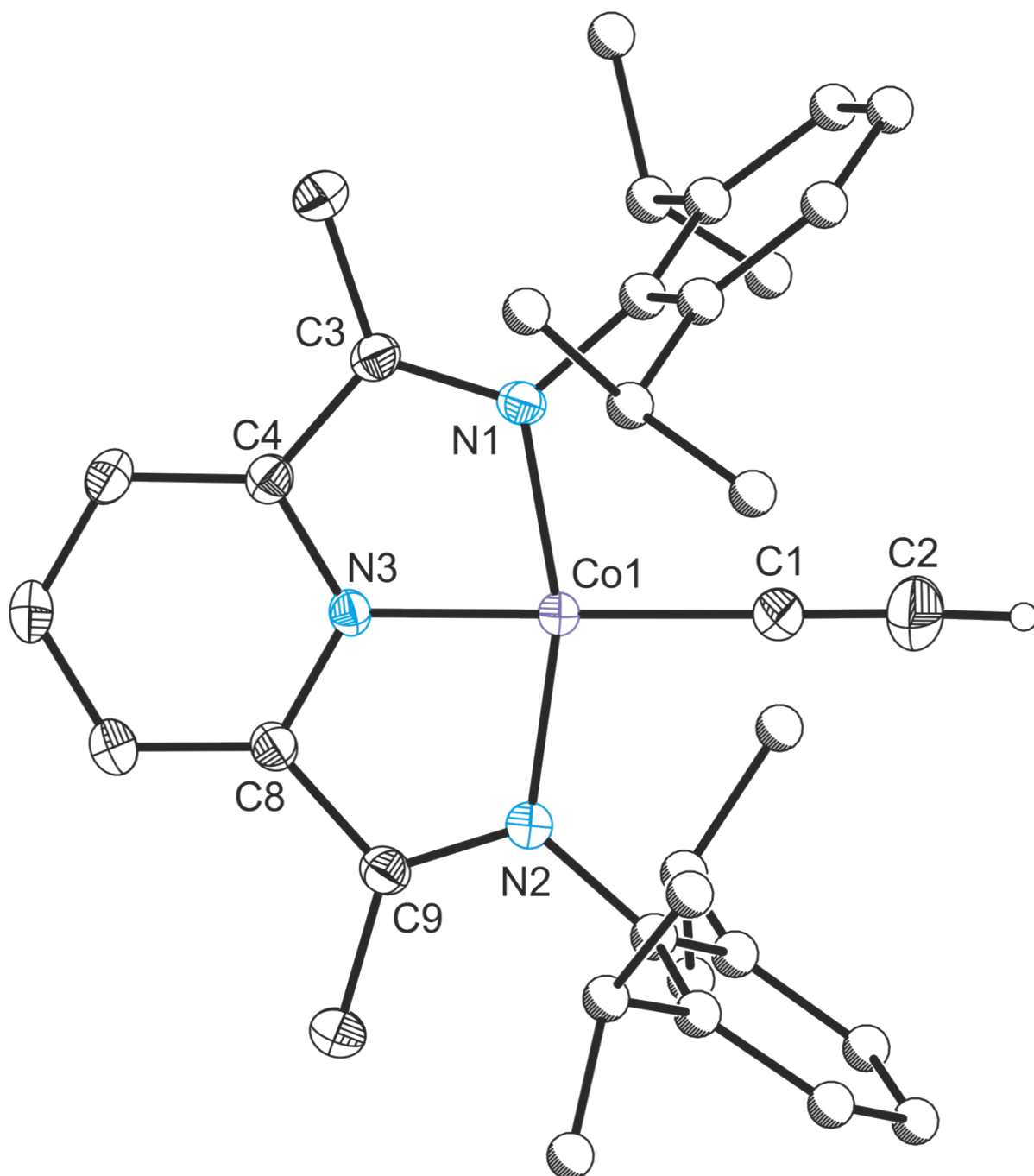


Figure S32. Single crystal X-ray structure of Co_{CCH} . Thermal ellipsoids displayed at 50% probability. Atoms of Dipp groups pictured as spheres of arbitrary radius. Hydrogen atoms (with the exception of that bonded to C2) have been removed for clarity. Selected bond distances (Å) and angles ($^{\circ}$): Co1–C1 1.906(3), C1–C2 1.192(4), Co1–N1 1.906(2), Co1–N2 1.904(2), Co1–N3 1.8117(19), N1–C3 1.319(3), C3–C4 1.442(3), C4–N3 1.367(3), N3–C8 1.374(3), C8–C9 1.445(3), C9–N2 1.321(3); C1–Co1–N1 98.14(10), C1–Co1–N2 99.28(10), C1–Co1–N3 179.31(11), N1–Co1–N2 162.54(8), N1–Co1–N3 81.38(9), Ni2–Co1–N3, 81.19(9).

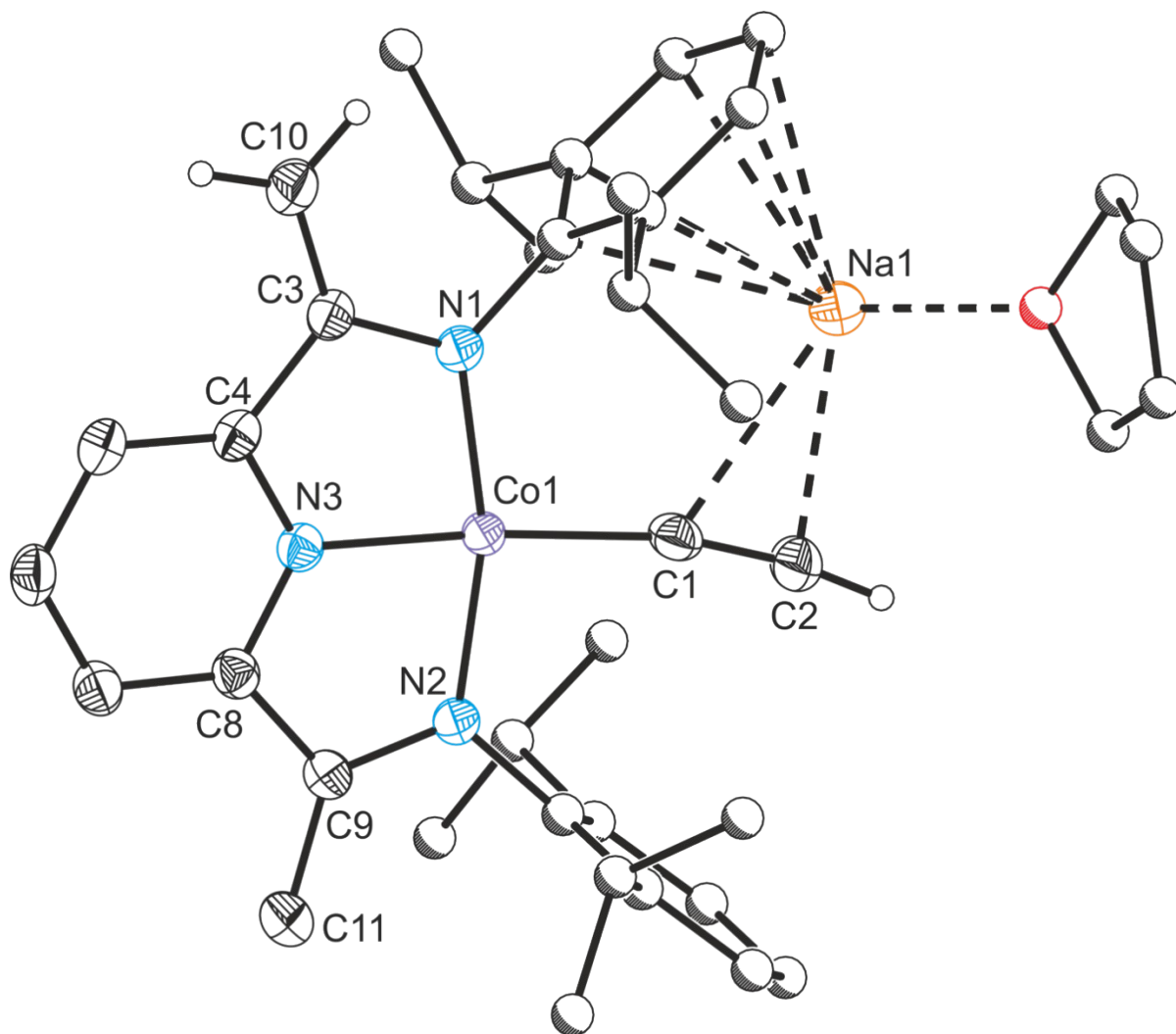


Figure S33. Single crystal X-ray structure of Na(THF)Co(PIEA)(CCH). Thermal ellipsoids displayed at 50% probability. Atoms of Dipp groups and THF molecule pictured as spheres of arbitrary radius. Hydrogen atoms (with the exception of that bonded to C2) have been removed for clarity. Selected bond distances (Å) and angles (°): Co1–C1 1.8970(15), C1–C2 1.212(2), Co1–N1 1.8759(11), Co1–N2 1.8686(11), Co1–N3 1.8399(11), N1–C3 1.3866(17), C3–C10 1.378(2), C3–C4 1.4681(19), C4–N3 1.3561(17), N3–C8 1.3678(17), C8–C9 1.4281(19), C9–C11 1.4680(19), C9–N2 1.3614(18); C1–Co1–N1 101.89(5), C1–Co1–N2 93.89(5), C1–Co1–N3 174.24(6), N1–Co1–N2 164.19(5), N1–Co1–N3 82.28(5), N2–Co1–N3, 81.91(5).

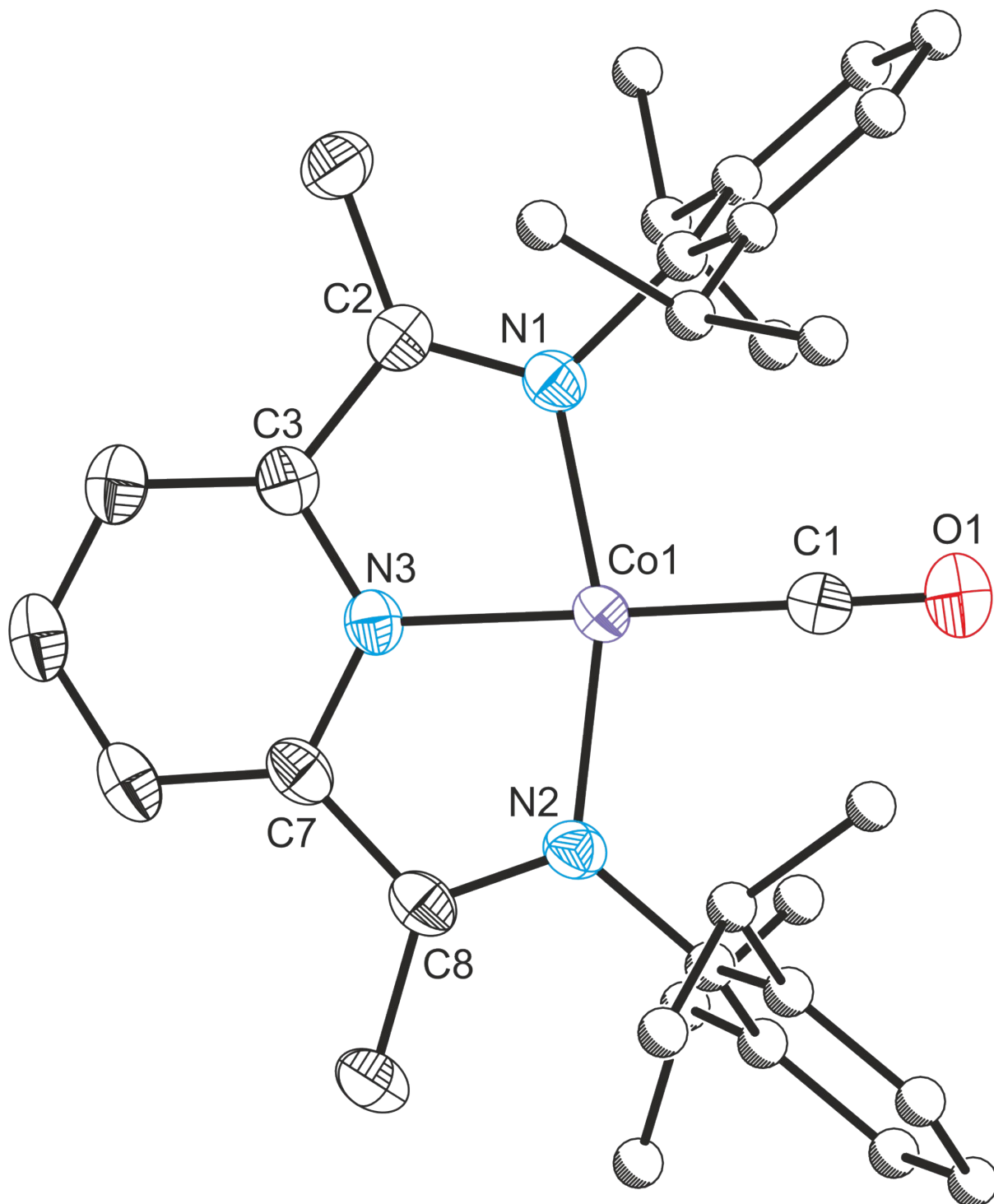


Figure S34. Single crystal X-ray structure of CoCo^+ . Thermal ellipsoids displayed at 50% probability. Atoms of Dipp groups pictured as spheres of arbitrary radius. Hydrogen atoms have been removed for clarity. Selected bond distances (\AA) and angles ($^\circ$): Co1–C1 1.773(3), C1–O1 1.129(4), Co1–N1 1.919(2), Co1–N2 1.920(2), Co1–N3 1.847(2), N1–C2 1.300(3), C2–C3 1.473(4), C3–N3 1.343(3), N3–C7 1.346(3), C7–C8 1.462(4), C8–N2 1.307(3); C1–Co1–N1 98.67(11), C1–Co1–N2 99.09(11), C1–Co1–N3 174.59(13), N1–Co1–N2 162.17(10), N1–Co1–N3 80.73(9), Ni2–Co1–N3, 81.43(10).

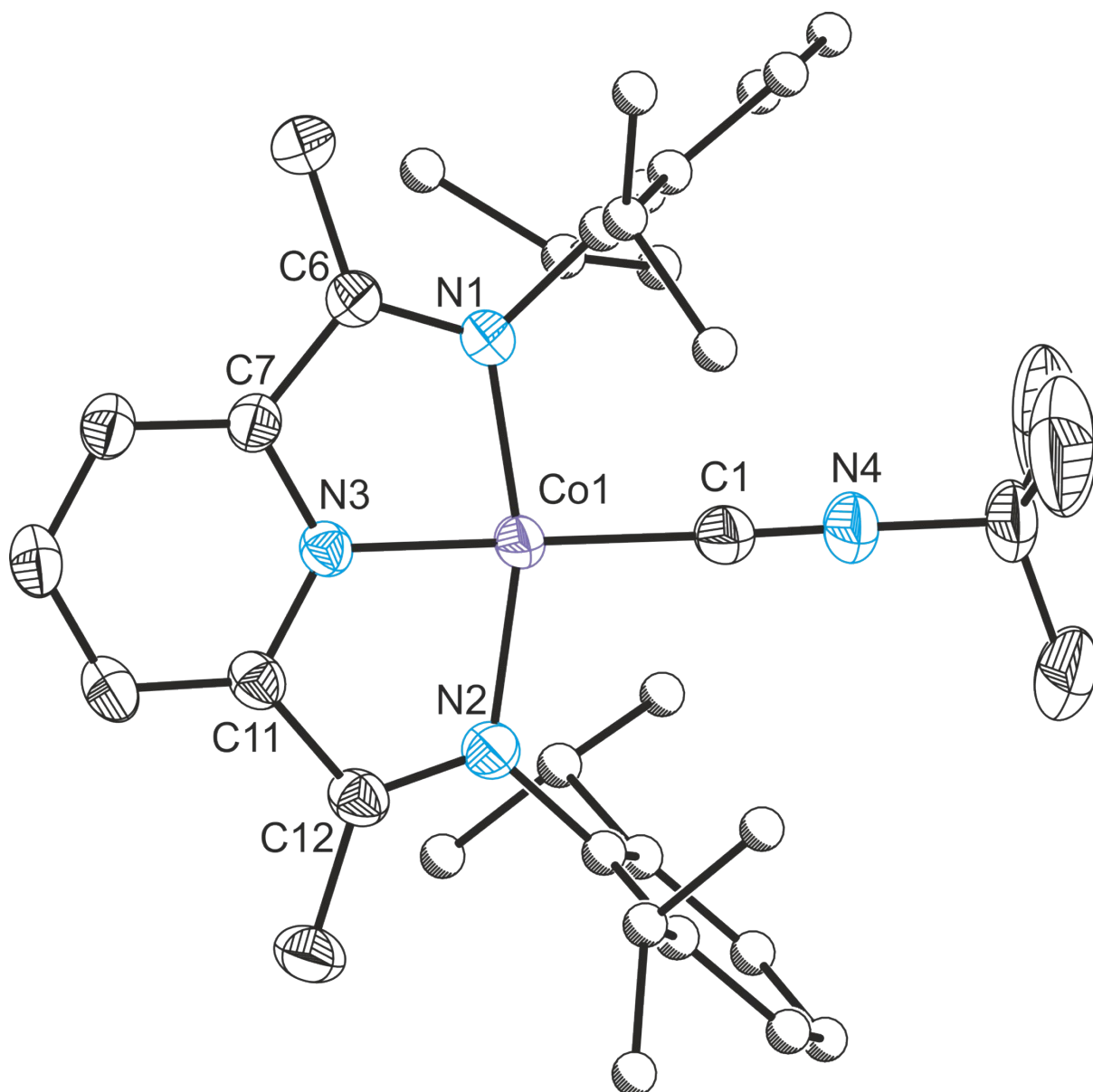


Figure S35. Single crystal X-ray structure of $\text{Co}_{\text{CNBu}}^+$. Thermal ellipsoids displayed at 50% probability. Atoms of Dipp groups pictured as spheres of arbitrary radius. Hydrogen atoms have been removed for clarity. Selected bond distances (Å) and angles ($^\circ$): Co1–C1 1.8755(19), C1–N4 1.154(3), Co1–N1 1.9072(14), Co1–N2 1.9198(15), Co1–N3 1.8186(14), N1–C6 1.312(2), C6–C7 1.451(2), C7–N3 1.357(2), N3–C11 1.353(2), C11–C12 1.457(2), C12–N2 1.309(2); C1–Co1–N1 97.83(7), C1–Co1–N2 99.30(7), C1–Co1–N3 171.81(8), N1–Co1–N2 162.44(6), N1–Co1–N3 81.03(6), Ni2–Co1–N3, 81.46(6).

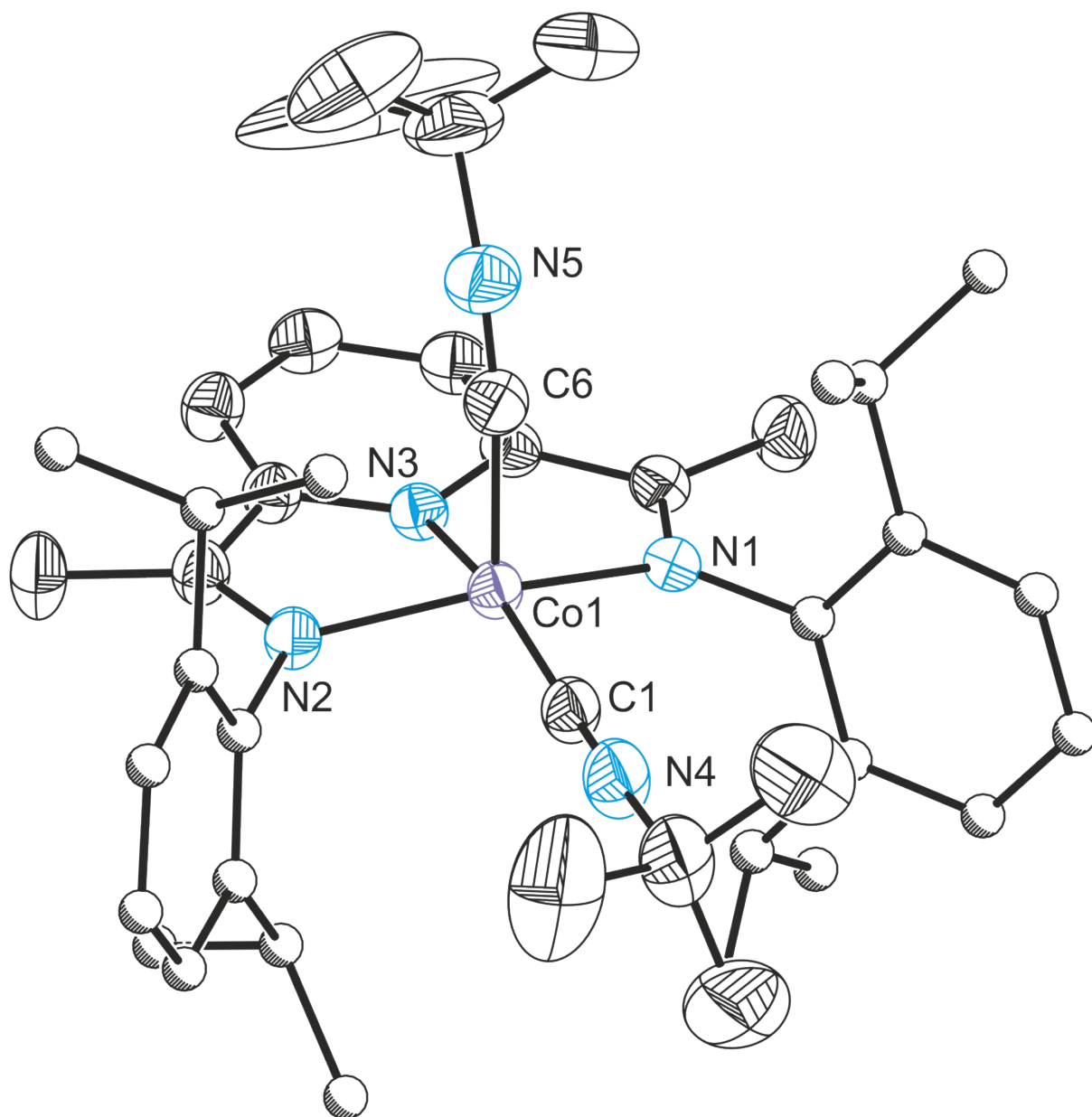


Figure S36. Single crystal X-ray structure of Co_2CNBu^+ . Thermal ellipsoids displayed at 50% probability. Atoms of Dipp groups pictured as spheres of arbitrary radius. Hydrogen atoms have been removed for clarity. Selected bond distances (Å) and angles ($^\circ$): Co1–C1 1.872(2), C1–N4 1.147(3), Co1–C6 1.918(2), C6–N5 1.146(3), Co1–N1 1.9329(16), Co1–N2 1.9319(16), Co1–N3 1.8194(16); C1–Co1–N1 97.75(8), C1–Co1–N2 97.04(8), C1–Co1–N3 166.86(9), C1–Co1–C6, 102.43(9), N1–Co1–N2 155.87(7), N1–Co1–N3 80.78(7), N1–Co1–C6 96.63(8), Ni2–Co1–N3, 80.48(7), N2–Co1–C6 98.67(8), N3–Co1–C6 90.70(8).

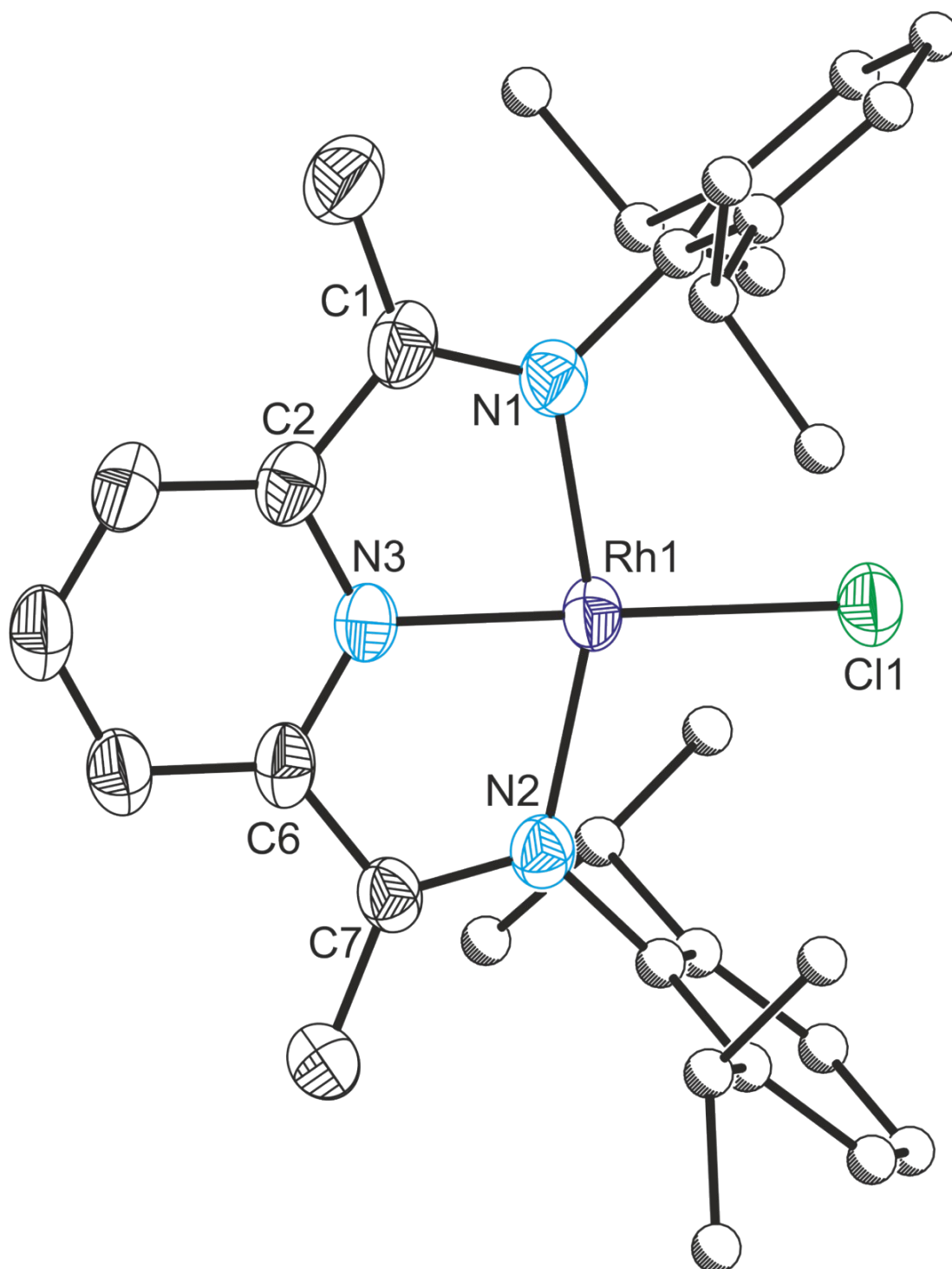


Figure S37. Single crystal X-ray structure of Rh_{Cl} . Thermal ellipsoids displayed at 50% probability. Atoms of Dipp groups pictured as spheres of arbitrary radius. Hydrogen atoms have been removed for clarity. Selected bond distances (\AA) and angles ($^\circ$): Rh1–Cl1 2.3191(12), Rh1–N1 2.032(4), Rh1–N2 2.036(4), Rh1–N3 1.897(4), N1–C1 1.310(7), C1–C2 1.467(8), C2–N3 1.365(6), N3–C6 1.353(7), C6–C7 1.455(7), C7–N2 1.311(6); Cl1–Rh1–N1 100.08(13), Cl1–Rh1–N2 100.85(12), Cl1–Rh1–N3 179.38(13), N1–Rh1–N2 159.06(16), N1–Rh1–N3 80.03(17), N2–Rh1–N3, 79.05(17).

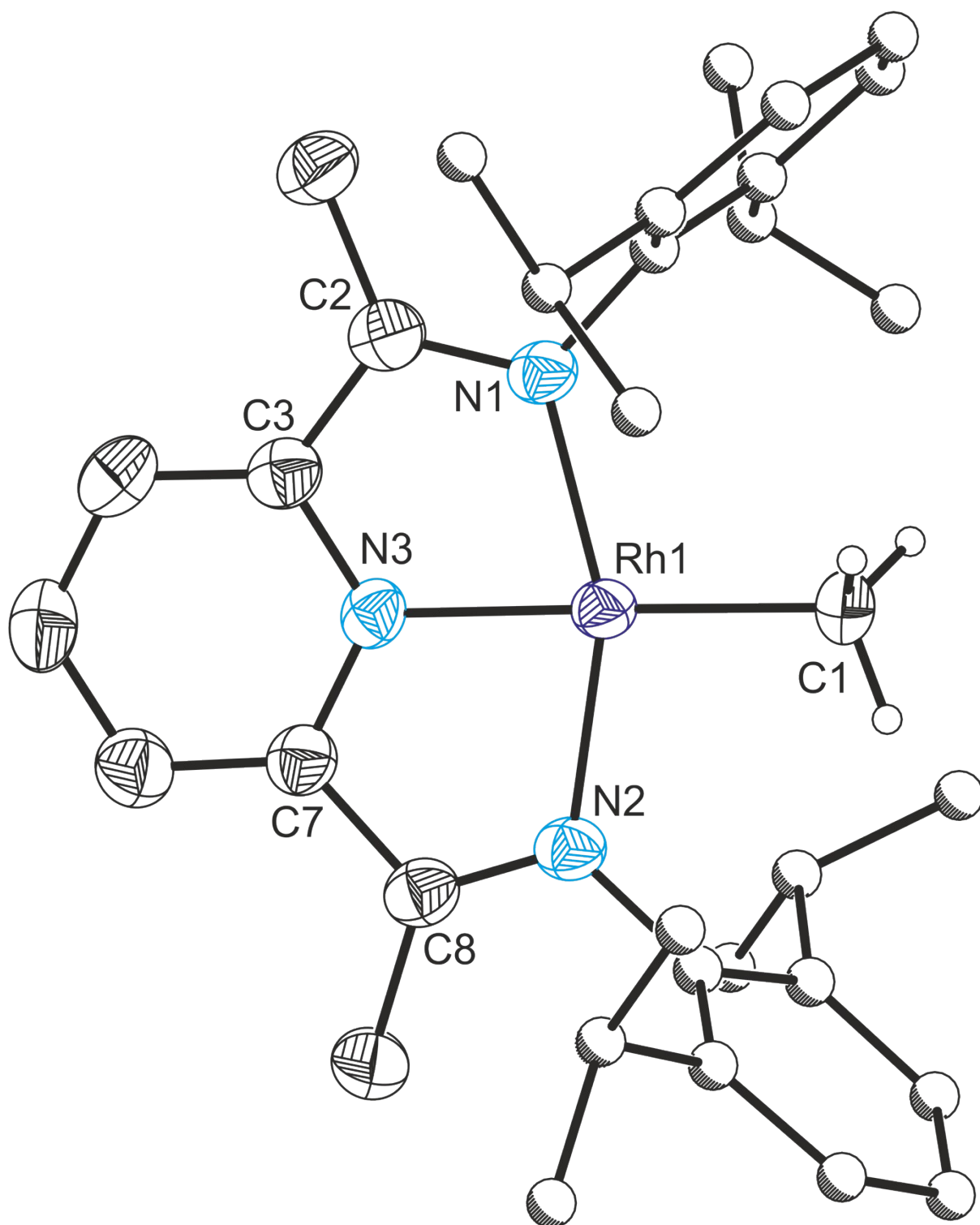


Figure S38. Single crystal X-ray structure of Rh_{Me} . Thermal ellipsoids displayed at 50% probability. Atoms of Dipp groups pictured as spheres of arbitrary radius. Hydrogen atoms (with the exception of those bonded to C1) have been removed for clarity. Selected bond distances (\AA) and angles ($^\circ$): Rh1–C1 2.074(4), Rh1–N1 2.015(3), Rh1–N2 2.022(3), Rh1–N3 1.936(3), N1–C2 1.329(6), C2–C3 1.454(6), C3–N3 1.364(5), N3–C7 1.367(6), C7–C8 1.465(6), C8–N2 1.310(6); C1–Rh1–N1 101.41(16), C1–Rh1–N2 101.14(16), C1–Rh1–N3 78.48(14), N1–Rh1–N2 157.31(15), N1–Rh1–N3 78.48(14), N2–Rh1–N3, 78.84(14).

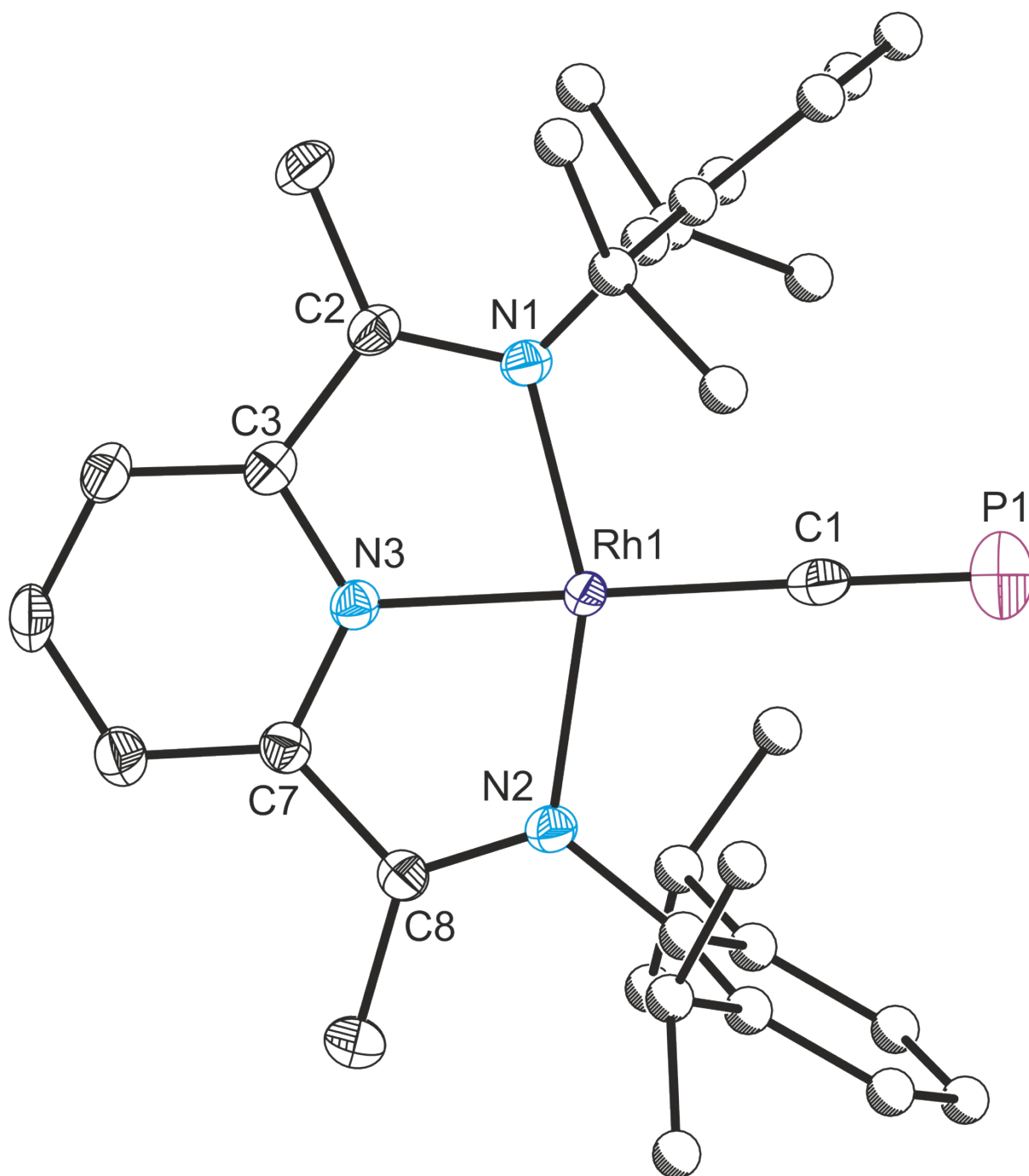


Figure S39. Single crystal X-ray structure of Rh_{cp} . Thermal ellipsoids displayed at 50% probability. Atoms of Dipp groups pictured as spheres of arbitrary radius. Hydrogen atoms have been removed for clarity. Selected bond distances (\AA) and angles ($^\circ$): Rh1–C1 1.969(3), C1–P1 1.542(4), Rh1–N1 2.019(2), Rh1–N2 2.023(2), Rh1–N3 1.942(2), N1–C2 1.309(4), C2–C3 1.470(4), C3–N3 1.360(4), N3–C7 1.357(4), C7–C8 1.468(4), C8–N2 1.315(4); C1–Rh1–N1 101.06(11), C1–Rh1–N2 101.41(11), C1–Rh1–N3 179.24(14), N1–Rh1–N2 157.48(10), N1–Rh1–N3 78.92(10), N2–Rh1–N3, 78.59(10).

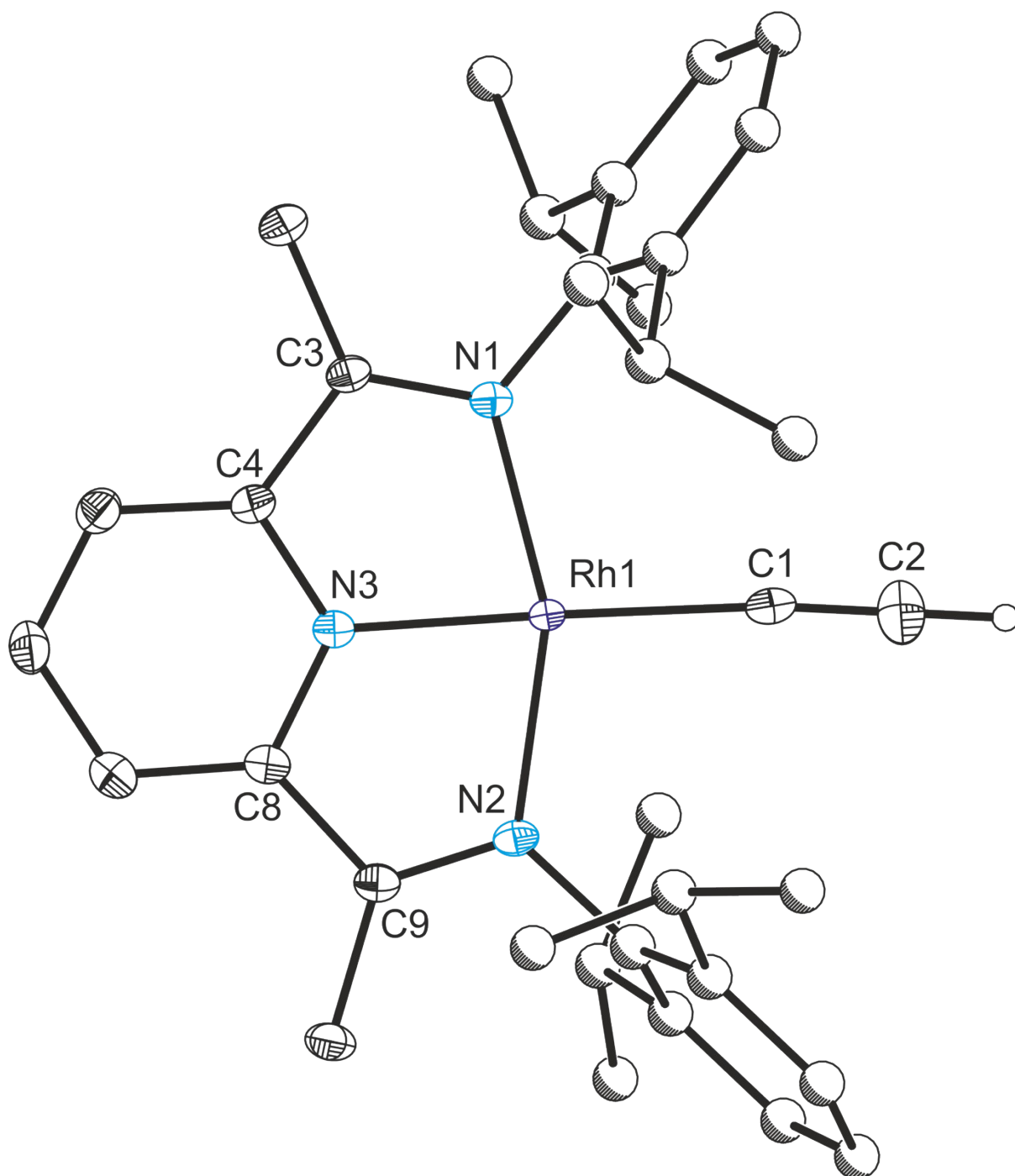


Figure S40. Single crystal X-ray structure of Rh_{cCH} . Thermal ellipsoids displayed at 50% probability. Atoms of Dipp groups pictured as spheres of arbitrary radius. Hydrogen atoms (with the exception of that bonded to C2) have been removed for clarity. Selected bond distances (Å) and angles ($^{\circ}$): Rh1–C1 2.025(2), C1–C2 1.188(3), Rh1–N1 2.0297(16), Rh1–N2 2.0378(16), Rh1–N3 1.9262(16), N1–C3 1.312(3), C3–C4 1.460(3), C4–N3 1.361(2), N3–C8 1.366(2), C8–C9 1.464(3), C9–N2 1.313(3); C1–Rh1–N1 103.08(7), C1–Rh1–N2 99.49(7), C1–Rh1–N3 177.18(7), N1–Rh1–N2 157.38(6), N1–Rh1–N3 78.78(6), N2–Rh1–N3, 78.73(7).

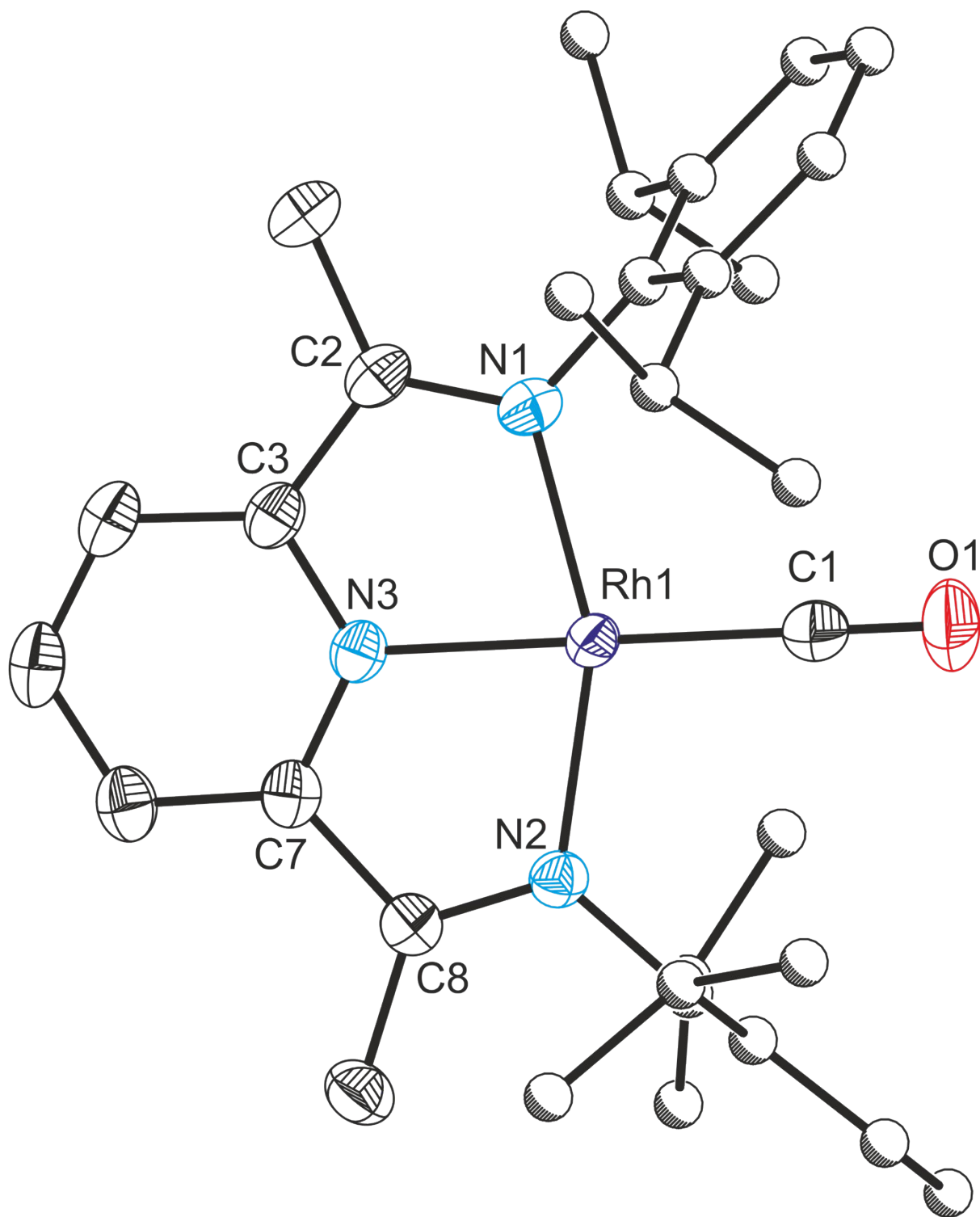


Figure S41. Single crystal X-ray structure of RhCO^+ . Thermal ellipsoids displayed at 50% probability. Atoms of Dipp groups pictured as spheres of arbitrary radius. Hydrogen atoms have been removed for clarity. Selected bond distances (\AA) and angles ($^\circ$): Rh1–C1 1.870(3), C1–O1 1.135(3), Rh1–N1 2.0442(19), Rh1–N2 2.0427(19), Rh1–N3 1.9684(19), N1–C2 1.301(3), C2–C3 1.482(3), C3–N3 1.341(3), N3–C7 1.343(3), C7–C8 1.484(3), C8–N2 1.302(3); C1–Rh1–N1 101.71(9), C1–Rh1–N2 101.07(9), C1–Rh1–N3 178.10(11), N1–Rh1–N2 157.22(8), N1–Rh1–N3 78.75(8), N2–Rh1–N3 78.49(8).

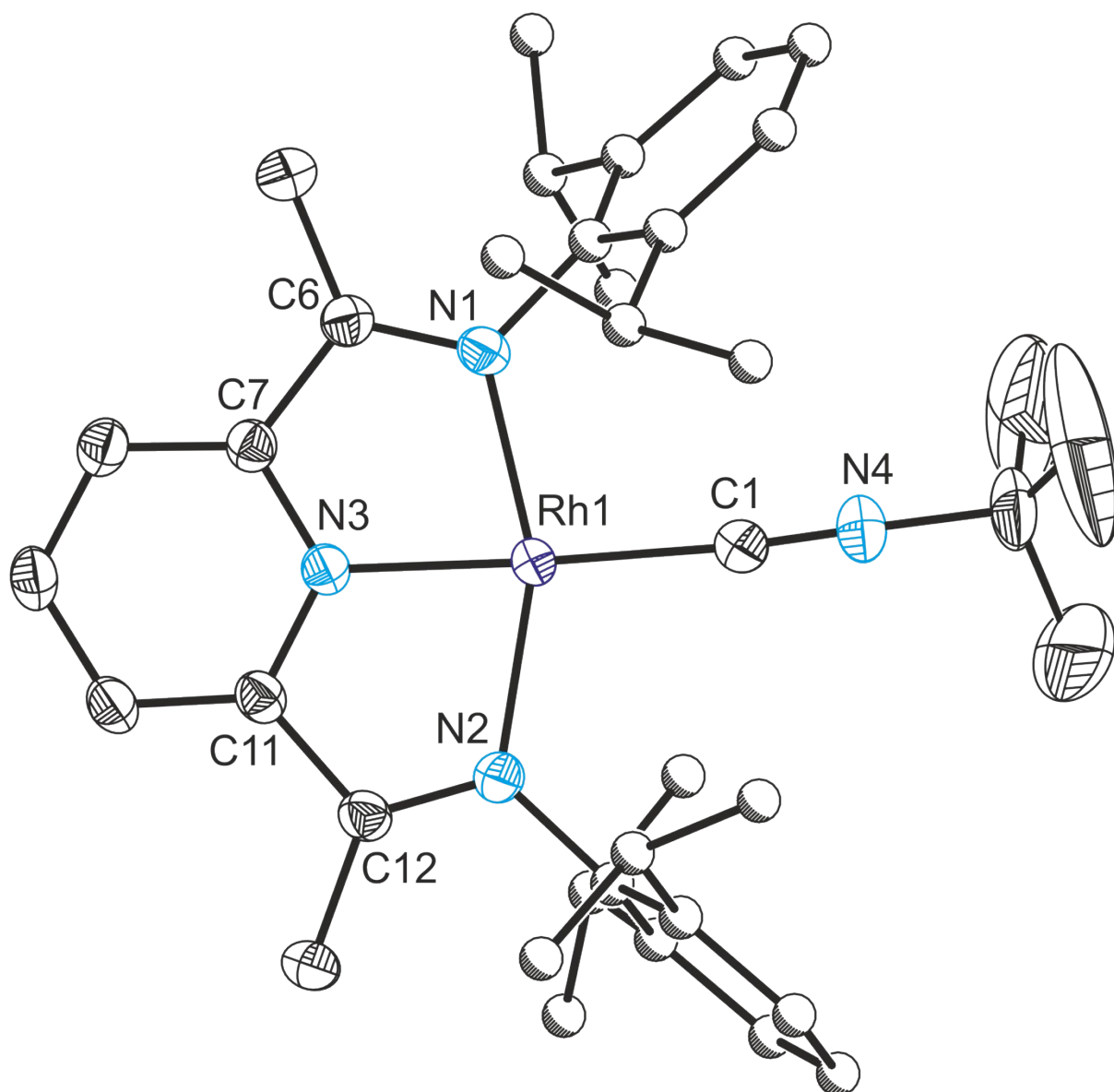


Figure S42. Single crystal X-ray structure of $\text{Rh}_{\text{CNBu}}^+$. Thermal ellipsoids displayed at 50% probability. Atoms of Dipp groups pictured as spheres of arbitrary radius. Hydrogen atoms have been removed for clarity. Selected bond distances (Å) and angles ($^\circ$): Rh1–C1 1.954(2), C1–N4 1.150(3), Rh1–N1 2.0310(18), Rh1–N2 2.0417(18), Rh1–N3 1.9422(17), N1–C6 1.306(3), C6–C7 1.475(3), C7–N3 1.348(3), N3–C11 1.345(3), C11–C12 1.479(3), C12–N2 1.301(3); C1–Rh1–N1 99.45(8), C1–Rh1–N2 102.87(8), C1–Rh1–N3 174.74(9), N1–Rh1–N2 157.60(7), N1–Rh1–N3 78.67(7), N2–Rh1–N3, 78.93(7).

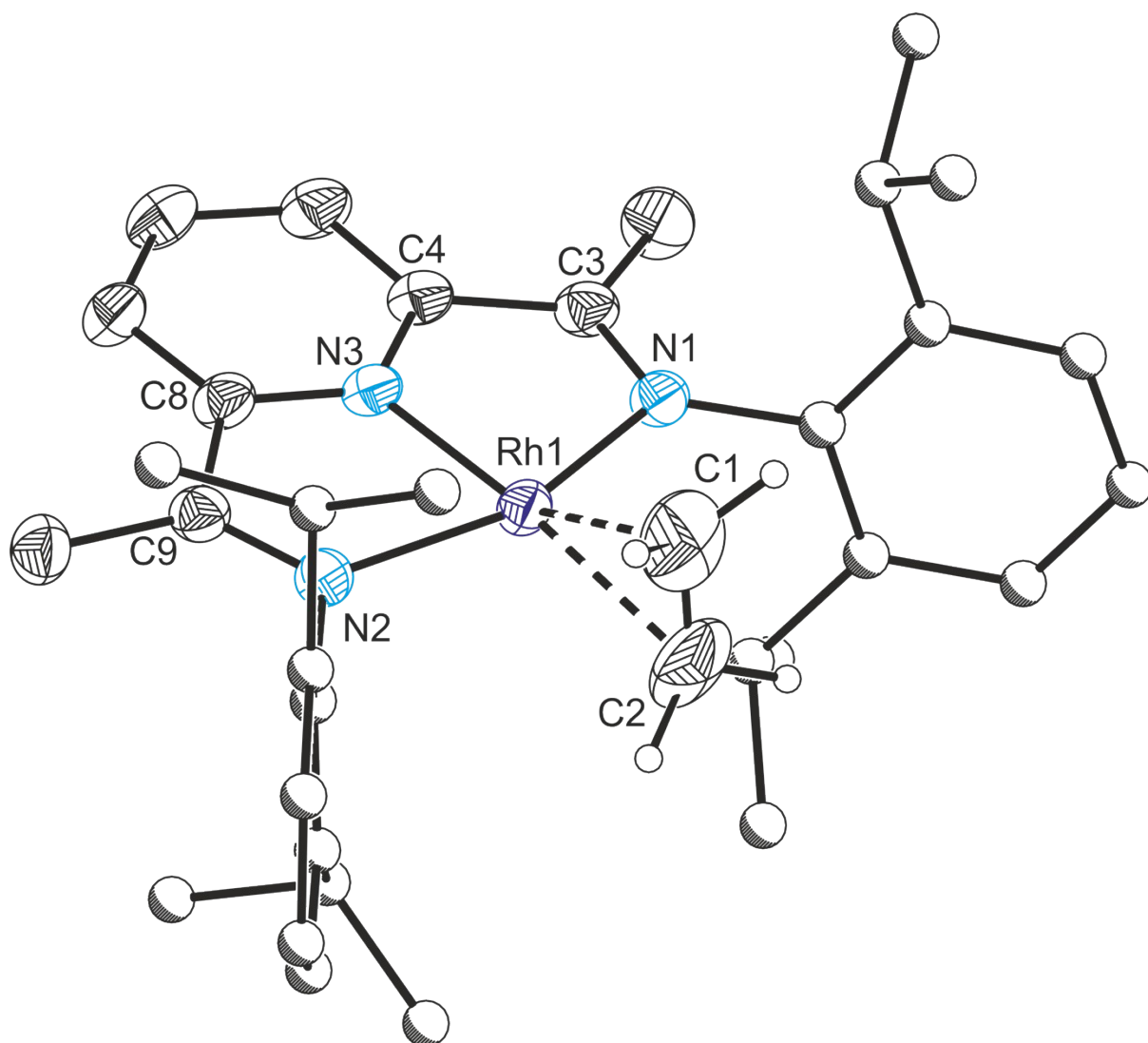


Figure S43. Single crystal X-ray structure of $\text{Rh}_{\text{ethylene}}^+$. Thermal ellipsoids displayed at 50% probability. Atoms of Dipp groups pictured as spheres of arbitrary radius. Hydrogen atoms have been removed for clarity. Selected bond distances (Å) and angles ($^\circ$): Rh1–C1 2.163(4), Rh1–C2 2.183(3), C1–C2 1.301(6), Rh1–N1 2.057(2), Rh1–N2 2.056(2), Rh1–N3 1.960(2), N1–C3 1.306(3), C3–C4 1.473(4), C4–N3 1.343(3), N3–C8 1.342(3), C8–C9 1.478(4), C9–N2 1.304(3); C1–Rh1–C2 34.84(17), C1–Rh1–N1 102.00(15), C1–Rh1–N2 100.06(15), C1–Rh1–N3 153.30(15), C2–Rh1–N1 100.71(14), C2–Rh1–N2 101.60(14), C2–Rh1–N3 171.86(14), N1–Rh1–N2 156.73(9), N1–Rh1–N3 78.51(9), N2–Rh1–N3, 78.47(9).

3. Computational details

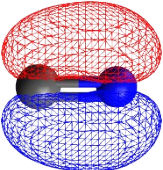
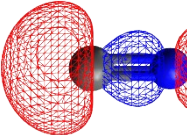
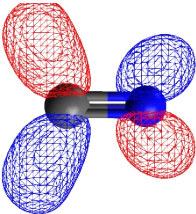
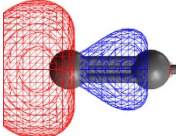
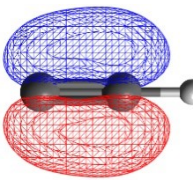
3.1. General computational methods

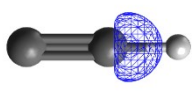
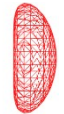
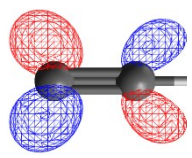
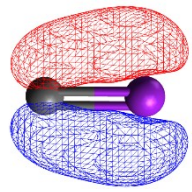
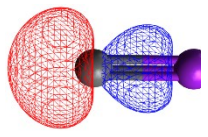
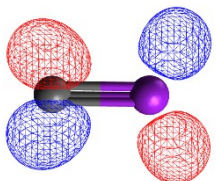
Density functional theory (DFT) calculations were performed using the ORCA 5.0.2 software package.^{10–12} All methods were used as implemented. Geometries were optimized using the B97-D3 functional and the def2-SVP basis set.^{13,14} Analytical frequency calculations were carried out to verify all molecular geometries as true minima ($N_{\text{imag}} = 0$). Single point calculations were performed on all molecules and fragments using the ω B97X-D3 functional¹⁵ and the Resolution of Identity approximation (RIJCOSX),^{15,16} and corrected for relativistic effects using the zeroth order regular approximation (ZORA). The segmented all-electron relativistically contracted basis set SARC-ZORA-TZVP was used for Au and Rh, and the relativistically contracted triple-zeta basis set ZORA-def2-TZVP was used for all other atoms, along with the SARC/J auxiliary basis set.^{16,17} Natural Bond Order analysis and Natural Population Analysis were carried out using the NBO 7.0 program.¹⁸ Energy decomposition analysis was carried out using the ETS-NOCV approach^{19,20} as implemented in ORCA 5.0.2, with difference densities generated by Multiwfn 3.8.²¹

3.2. Calculations on anions

Calculations on the cyanide ($\text{C}\equiv\text{N}^-$), acetylide ($\text{C}\equiv\text{CH}^-$) and cyaphide ($\text{C}\equiv\text{P}^-$) anions were performed using a method benchmarked against experimental and calculated electron affinities (EA) for ($\text{C}\equiv\text{N}^\bullet$),²² ($\text{C}\equiv\text{CH}^\bullet$),²³ and ($\text{C}\equiv\text{P}^\bullet$)²⁴: the range separated hybrid functional wB97X-D3, the zero order regular approximation (ZORA) using HF model densities, and the relativistically contracted quadruple-zeta basis set with added polarization functions ZORA-def2-QZVPP.

Table S5. Frontier orbitals of the cyanide, acetylide, and cyaphide ions ($\text{C}\equiv\text{E}^-$, E = N, CH, P).

	Isosurface	Reduced Loewdin Population		Energy /eV	EA(CE^\bullet) / eV
		C	E		
$\text{C}\equiv\text{N}^-$ HOMO-1/HOMO-2		44.2%	55.8%	-4.47	
$\text{C}\equiv\text{N}^-$ HOMO		71.6%	28.4%	-3.62	3.862 ²²
$\text{C}\equiv\text{N}^-$ LUMO/LUMO+1		79.3%	20.7%	9.34	
$\text{C}\equiv\text{CH}^-$ HOMO-2		80.9%	19.1%	-3.19	
$\text{C}\equiv\text{CH}^-$ HOMO/HOMO-1		43.6%	56.4%	-3.08	2.969 ²³

$\text{C}\equiv\text{CH}^-$ LUMO			7.5%	92.5%	7.75	
$\text{C}\equiv\text{CH}^-$ LUMO+1/LUMO+2			48.5%	51.5%	8.98	
$\text{C}\equiv\text{P}^-$ HOMO-1/HOMO-2			43.5%	56.5%	-3.36	
$\text{C}\equiv\text{P}^-$ HOMO			70.1%	29.9%	-3.06	2.806 ²⁴
$\text{C}\equiv\text{P}^-$ LUMO/LUMO+1			41.0%	59.0%	6.69	

3.3. Natural Bond Orbital analysis

Table S6. Summary of NBO and NPA analysis of Au(IDipp)(L) complexes, including second order perturbation energies corresponding to Au–L π back-donation ($E^{(2)}_{\pi}$).

NBO Lewis Structure	NPA Charge			Wiberg Bond Index		$E^{(2)}_{\pi}(\text{Au-L}) / \text{kcal mol}^{-1}$
	Au	C_{NHC}	C_{L}	$C_{\text{NHC-Au}}$	Au–L	
IDipp \rightarrow Au–C \equiv P	0.42	0.14	–0.98	0.49	0.58	22.0
IDipp \rightarrow Au–C \equiv N	0.37	0.14	–0.15	0.49	0.58	19.9
IDipp \rightarrow Au–C \equiv N(BCF)	0.43	0.13	0.18	0.51	0.56	27.8
IDipp \rightarrow Au–C \equiv CH	0.40	0.15	–0.46	0.50	0.58	19.2
IDipp \rightarrow Au–Me	0.32	0.16	–1.12	0.47	0.61	6.2
IDipp–Au ⁺ ←Cl [–]	0.41	0.16	–	0.60	0.45	–
IDipp–Au ⁺ ←OH [–]	0.48	0.18	–	0.64	0.42	–

Table S7. Summary of NBO and NPA analysis of Rh(^DiPPDI)(L) complexes, including second order perturbation energies corresponding to Rh–L π back-donation ($E^{(2)}_{\pi}$).

NBO Lewis Structure	NPA Charge		Wiberg Bond Index		$E^{(2)}_{\pi}(\text{Rh-L}) / \text{kcal mol}^{-1}$
	Rh	(^D iPPDI)	$\Sigma(N_{\text{PDI-Rh}})$	Rh–L	
(^D iPPDI) \rightarrow Rh–C \equiv P	0.23	0.43	1.19	0.73	44.1
(^D iPPDI) \rightarrow Rh–C \equiv N	0.21	0.43	1.26	0.63	28.7
(^D iPPDI) \rightarrow Rh–C \equiv CH	0.26	0.34	1.29	0.63	26.0
(^D iPPDI) \rightarrow Rh–Me	0.40	0.02	1.39	0.62	4.7
(^D iPPDI) \rightarrow Rh ⁺ –C \equiv O	0.21	0.66	1.14	0.93	78.1
(^D iPPDI) \rightarrow Rh ⁺ –C \equiv N– ^t Bu	0.21	0.56	1.19	0.72	52.5
(^D iPPDI) \rightarrow Rh ⁺ ←	0.37	0.61	1.26	0.66	–
(^D iPPDI) \rightarrow Rh ⁺ ←Cl [–]	0.36	0.32	1.46	0.39	–

3.4. Energy decomposition analysis

Table S8. Summary of EDA-NOCV analysis of the M–L bond in Au(IDipp)(L) and Rh(^{Dipp}PDI)(L) complexes, including ETS-NOCV energies from orbital contributions due to σ donation (ΔE_{orb}) and π back-donation (ΔE_{orb}), in kcal mol⁻¹.

	ΔE_{tot}	ΔE_{steric}	ΔE_{disp}	ΔE_{oi}	ΔE_{orb}	ΔE_{orb}
IDippAu–C≡P	-111.6	5.4	-31.4	-85.6	-44.5	-18.0
IDippAu–C≡P Ni ^{(Me)IPr} ₂	-126.3	54.3	-77.8	-102.8	-51.0	-17.5
IDippAu–C≡P Rh(Cp*)(PMe ₃)	-101.5	51.7	-59.5	-93.7	-46.9	-17.2
IDippAu–C≡P W(CO) ₅ Rh(Cp*)(PMe ₃)	-109.2	54.9	-71.4	-92.7	-47.0	-18.4
IDippAu–C≡N	-101.0	2.9	-31.0	-72.8	-40.8	-12.3
IDippAu–C≡N(BCF)	-73.9	50.1	-54.1	-69.8	-35.1	-19.1
IDippAu–C≡CH	-107.7	4.2	-31.1	-80.8	-42.5	-12.8
IDippAu–Me	-107.7	4.9	-30.7	-81.9	-50.5	-8.3
IDippAu–Cl	-91.1	7.4	-31.0	-67.5	-38.4	-5.6
IDippAu–OH	-113.9	1.9	-30.5	-85.3	-46.0	-6.5
DippPDIRh–C≡P	-108.1	28.8	-39.4	-97.4	-46.5	-21.5
DippPDIRh–C≡N	-98.4	15.5	-38.1	-75.8	-38.3	-11.1
DippPDIRh–C≡CH	-113.2	12.5	-38.4	-87.3	-41.6	-13.5
DippPDIRh–Me	-106.8	13.7	-38.6	-81.9	-50.5	-8.3
[^{Dipp} PDIRh–C≡O] ⁺	-50.2	67.5	-37.6	-80.1	-31.1	-42.2
[^{Dipp} PDIRh–C≡N– ^t Bu] ⁺	-62.7	50.0	-46.9	-65.8	-32.2	-25.5
[^{Dipp} PDIRh–] ⁺	-43.6	53.6	-39.8	-57.4	-22.3	-25.0
DippPDIRh–Cl	-92.4	10.7	-38.0	-65.1	-28.2	-5.5

$$\Delta E_{\text{tot}} = \Delta E_{\text{steric}} + \Delta E_{\text{disp}} + \Delta E_{\text{oi}} = \Delta E_{\text{steric}} + \Delta E_{\text{disp}} + \Sigma \Delta E_{\text{orb}}$$

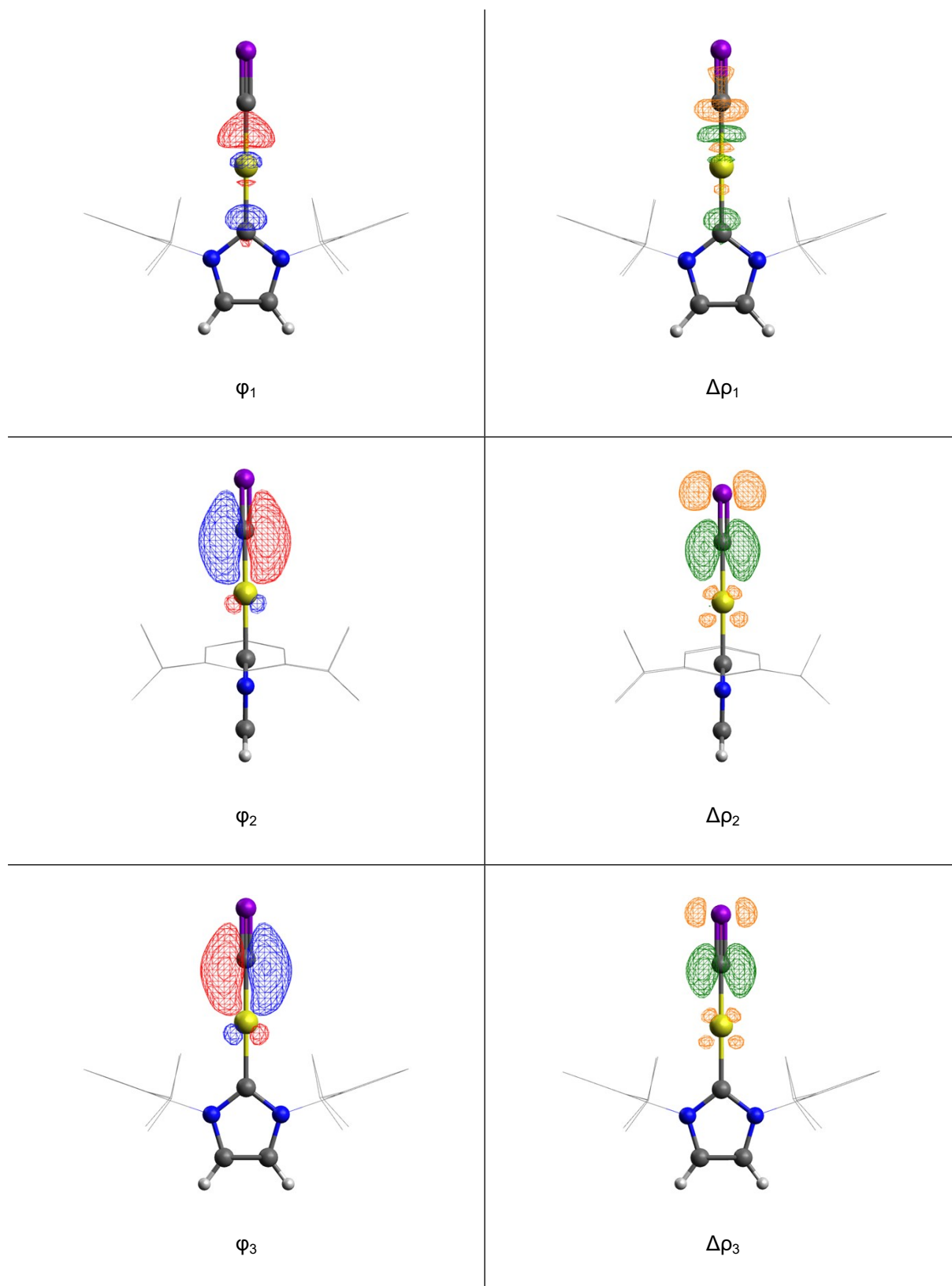


Figure S44. Contours of NOCVs φ_1 , φ_2 , and φ_3 , ($v > 0$), as well as their contributions to the deformation density, $\Delta\rho_1$, $\Delta\rho_2$, and $\Delta\rho_3$, (green: $\Delta\rho > 0$, orange: $\Delta\rho < 0$), for the Au–CP interaction in Au(IDipp)(CP). φ_1 corresponds to σ donation, whereas φ_2 and φ_3 correspond to π back-donation.

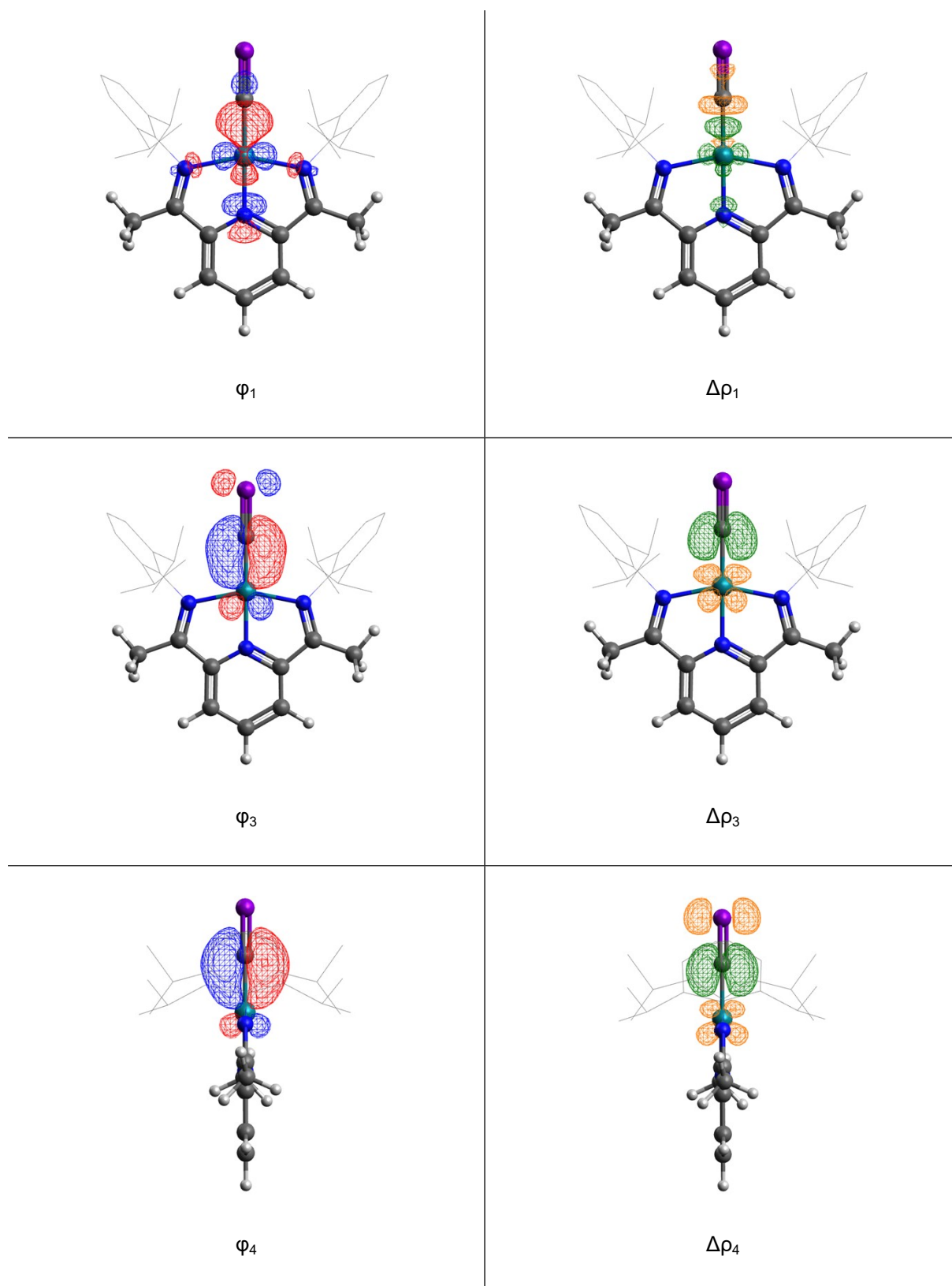


Figure S45. Contours of NOCVs φ_1 , φ_3 , and φ_4 , ($v > 0$), as well as their contributions to the deformation density, $\Delta\rho_1$, $\Delta\rho_3$, and $\Delta\rho_4$, (green: $\Delta\rho > 0$, orange: $\Delta\rho < 0$), for the Rh–CP interaction in Rh(^DiPPDI)(CP). φ_1 corresponds to σ donation, whereas φ_3 and φ_4 correspond to π back-donation.

3.5. Data analysis

Table S9. $^{13}\text{C}_{\text{NHC}}$ NMR shifts and $\text{C}_{\text{NHC}}\text{-Au}$ bond lengths for $\text{Au}(\text{IDipp})(\text{L})$ complexes.

L	$^{13}\text{C}_{\text{NHC}}$ / ppm	$\text{C}_{\text{NHC}}\text{-Au}$ / Å	Ref.
CP^-	193.0	2.035(6)	6
$(\mu\text{-CP})\{\text{Ni}(\text{Me}^i\text{Pr})_2\}^-$	198.5	2.024(3)	25
$(\mu\text{-CP})\{\text{Rh}(\text{Cp}^*)(\text{PMe}_3)\}^-$	195.6	2.026(4)	25
$(\mu_3\text{-CP})\{\text{Rh}(\text{Cp}^*)(\text{PMe}_3)\}\{\text{W}(\text{CO})_5\}^-$	193.9	2.025(4)	25
CN^-	186.2	2.00(2)	26
$(\mu\text{-CN})(\text{BCF})^-$	183.1	2.005(3)	25
CCPh^-	190.9	2.018(7)	26
BPin^-	216.7	2.084(4)	27
H^-	204.9	2.045(3)	28
Me^-	201.4	2.038(5)	29
OH^-	171.9	1.935(9)	26
Cl^-	175.1	1.9394(1)	30,31
CO	174.6	1.971(5)	32
CNXyl	178.6	–	33
IDipp	184.2	2.025(7)	34
P^iBu_3	191.9	2.045(7)	34
PPh_3	188.2	2.039(5)	34
Py	167.1	1.961(7)	35
MeCN	166.0	1.974(2)	35

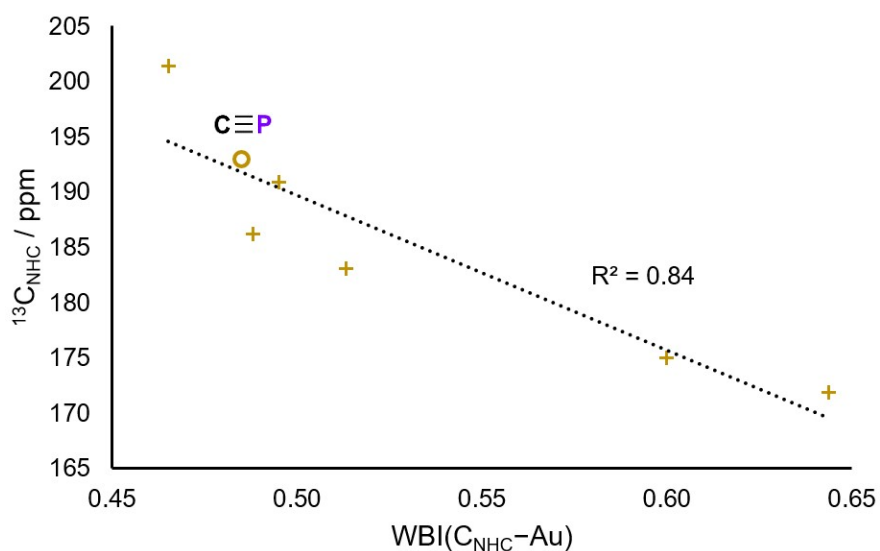


Figure 46. Calculated C_{NHC}-Au bond order (Wiberg) plotted against experimental ¹³C_{NHC} NMR shifts for selected Au(IDipp)(L) complexes.

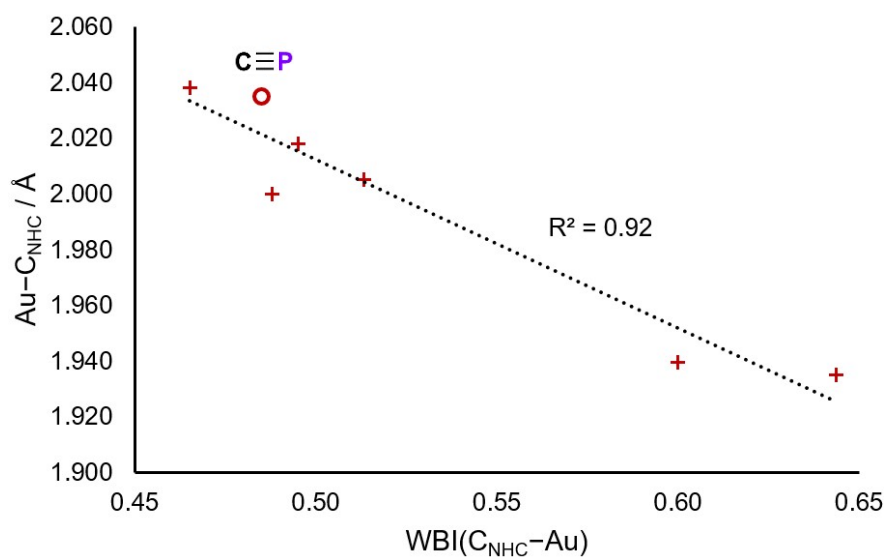


Figure S47. Calculated C_{NHC}-Au bond order (Wiberg) plotted against experimental solid-state C_{NHC}-Au bond lengths for selected Au(IDipp)(L) complexes.

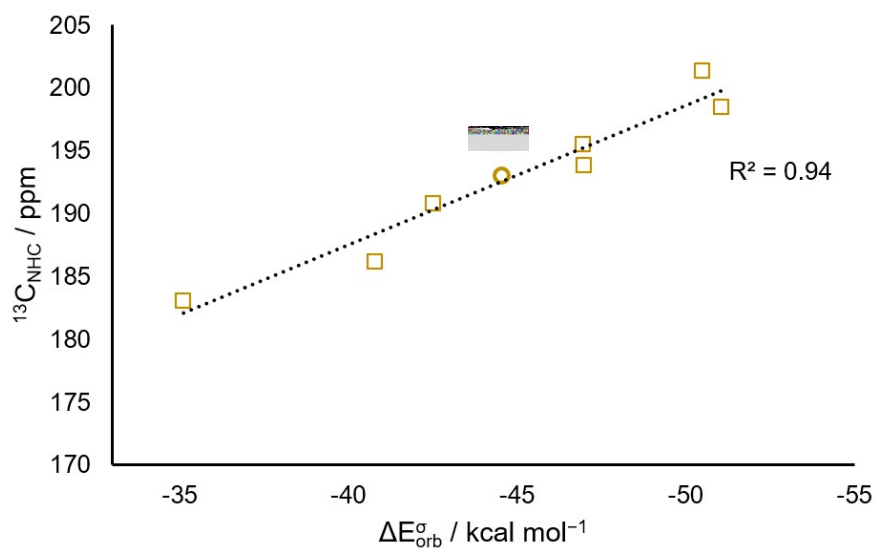


Figure S48. Calculated L–Au σ donation energies (ETS-NOCV, ΔE_{orb}) plotted against experimental $^{13}\text{C}_{\text{NHC}}$ NMR shifts for selected Au(IDipp)(L) complexes.

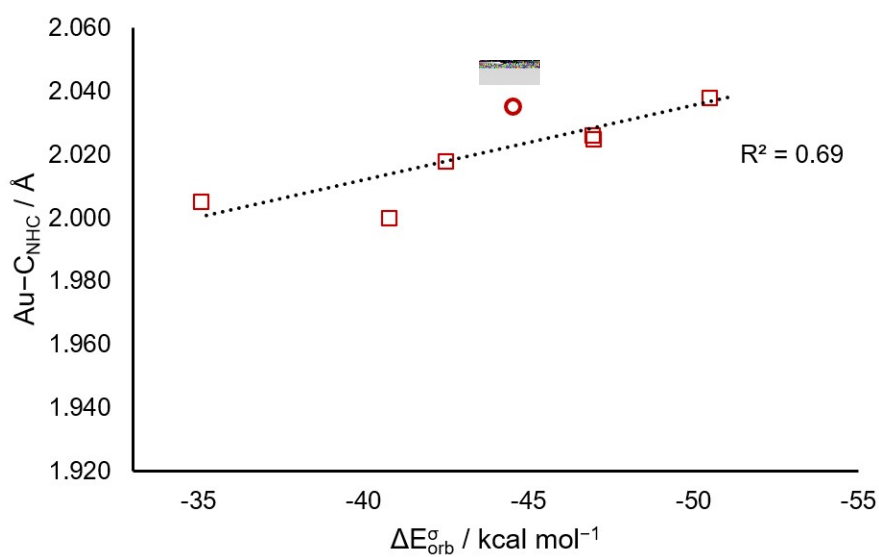


Figure S49. Calculated L–Au σ donation energies (ETS-NOCV, ΔE_{orb}) plotted against experimental solid-state $\text{C}_{\text{NHC}}\text{–Au}$ bond lengths for selected Au(IDipp)(L) complexes.

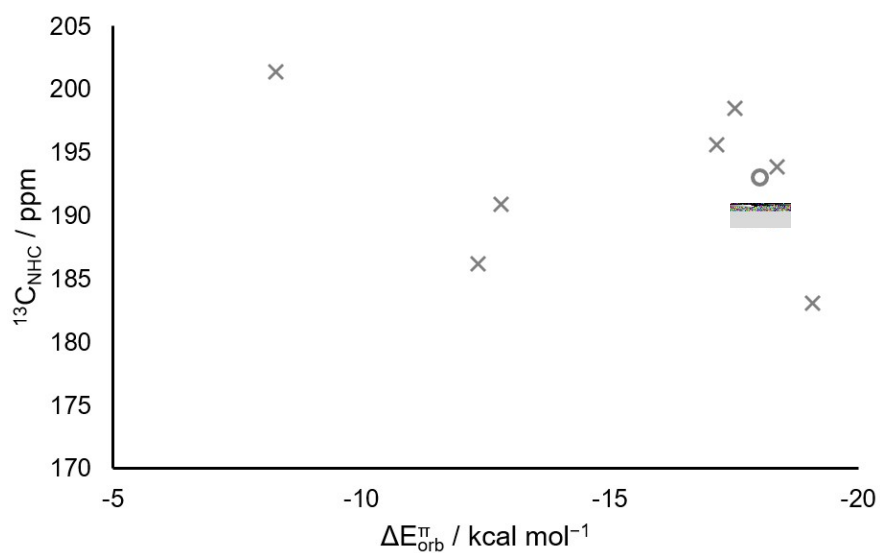


Figure S50. Calculated Au–L π back-donation energies (ETS-NOCV, ΔE_{orb}) plotted against experimental $^{13}\text{C}_{\text{NHC}}$ NMR shifts for selected Au(IDipp)(L) complexes.

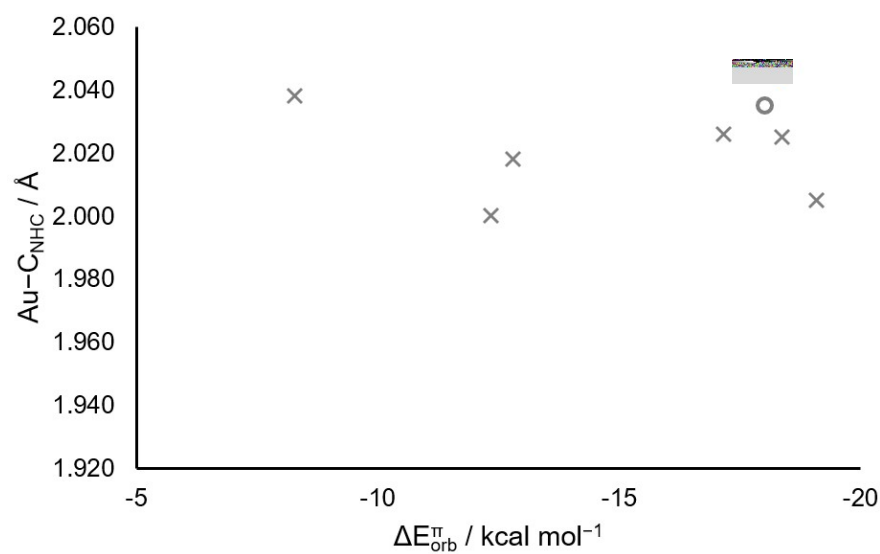


Figure S51. Calculated Au–L π back-donation energies (ETS-NOCV, ΔE_{orb}) plotted against experimental solid-state C_{NHC}–Au bond lengths for selected Au(IDipp)(L) complexes.

Table S10. $\delta(\text{PDI})$ values and $\text{N}_{\text{py}}\text{-Co}$ bond lengths for $\text{Co}(\text{DippPDI})(\text{L})$ complexes.

$$\delta(\text{PDI}) = \left(\frac{d2 + d2'}{2} \right) - \left(\frac{d1 + d1' + d3 + d3'}{4} \right)$$

L	$\delta(\text{PDI})^*$	$\text{N}_{\text{py}}\text{-Co} / \text{\AA}$	Ref.
CP^-	0.131(9)	1.825(3)	6
CCH^-	0.098(7)	1.812(2)	–
Me^-	0.090(9)	1.834(3)	36
N_2	0.132(9)	1.812(3)	3
CO	0.144(7)	1.847(2)	–
CN^iBu	0.121(4)	1.819(2)	–
Cl^-	0.096(12)	1.798(3)	3

*Uncertainties were determined by error propagation, where

$$\sigma(\delta(\text{PDI})) = \sqrt{\left(\frac{\sigma(d2)}{2}\right)^2 + \left(\frac{\sigma(d2')}{2}\right)^2 - \left(\frac{\sigma(d1)}{4}\right)^2 - \left(\frac{\sigma(d1')}{4}\right)^2 - \left(\frac{\sigma(d3)}{4}\right)^2 - \left(\frac{\sigma(d3')}{4}\right)^2}$$

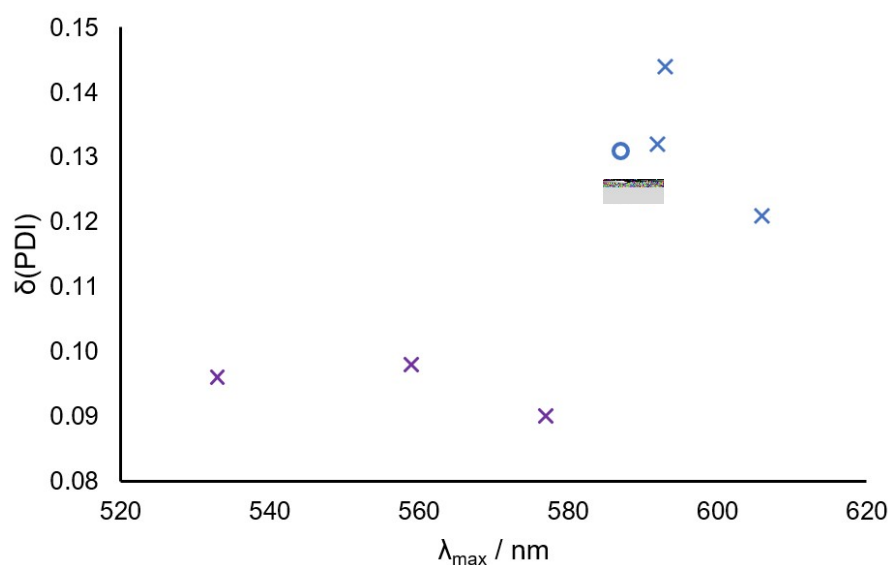
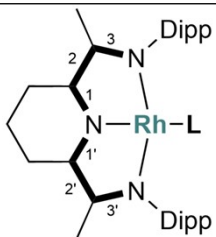
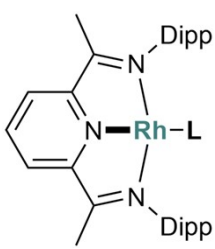
**Figure S52.** Experimental UV-vis absorption maxima (λ_{max}) plotted against experimental $\delta(\text{PDI})$ values for $\text{Co}(\text{DippPDI})(\text{L})$ complexes.

Table S11. $\delta(\text{PDI})$ values and $N_{\text{py}}\text{-Rh}$ bond lengths for $\text{Rh}(\text{DippPDI})(\text{L})$ complexes.


$$\delta(\text{PDI}) = \left(\frac{d_2 + d_{2'}}{2} \right) - \left(\frac{d_1 + d_{1'} + d_3 + d_{3'}}{4} \right)$$



L	$\delta(\text{PDI})^*$	$N_{\text{py}}\text{-Rh} / \text{\AA}$
CP ⁻	0.134(3)	1.943(2)
CCH ⁻	0.124(2)	1.926(2)
Me ⁻	0.110(6)	1.936(3)
CO	0.161(3)	1.969(2)
CN ^t Bu	0.152(3)	1.942(3)
C ₂ H ₄	0.152(3)	1.960(2)
Cl	0.108(6)	1.898(4)

*Uncertainties were determined by error propagation, where

$$\sigma(\delta(\text{PDI})) = \sqrt{\left(\frac{\sigma(d_2)}{2}\right)^2 + \left(\frac{\sigma(d_{2'})}{2}\right)^2 - \left(\frac{\sigma(d_1)}{4}\right)^2 - \left(\frac{\sigma(d_{1'})}{4}\right)^2 - \left(\frac{\sigma(d_3)}{4}\right)^2 - \left(\frac{\sigma(d_{3'})}{4}\right)^2}$$

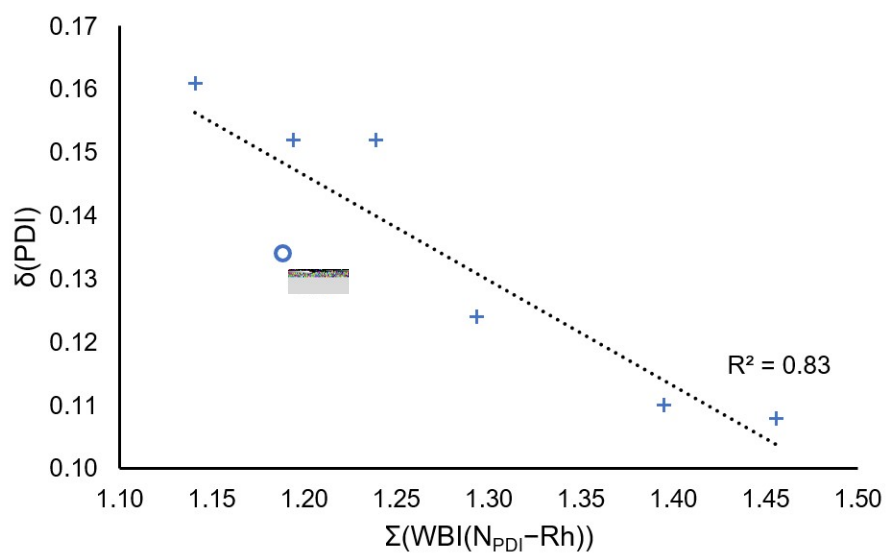


Figure S53. Calculated $\text{N}_{\text{PDI}}-\text{Rh}$ bond orders (Wiberg) plotted against experimental $\delta(\text{PDI})$ values for selected $\text{Rh}(\text{DippPDI})(\text{L})$ complexes.

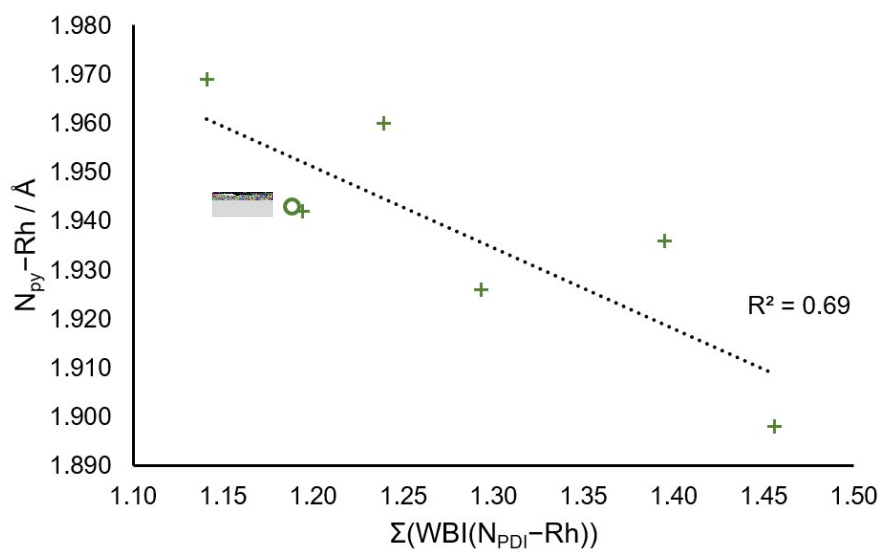


Figure S54. Calculated $\text{N}_{\text{PDI}}-\text{Rh}$ bond orders (Wiberg) plotted against experimental solid-state $\text{N}_{\text{py}}-\text{Rh}$ bond lengths for selected $\text{Rh}(\text{DippPDI})(\text{L})$ complexes.

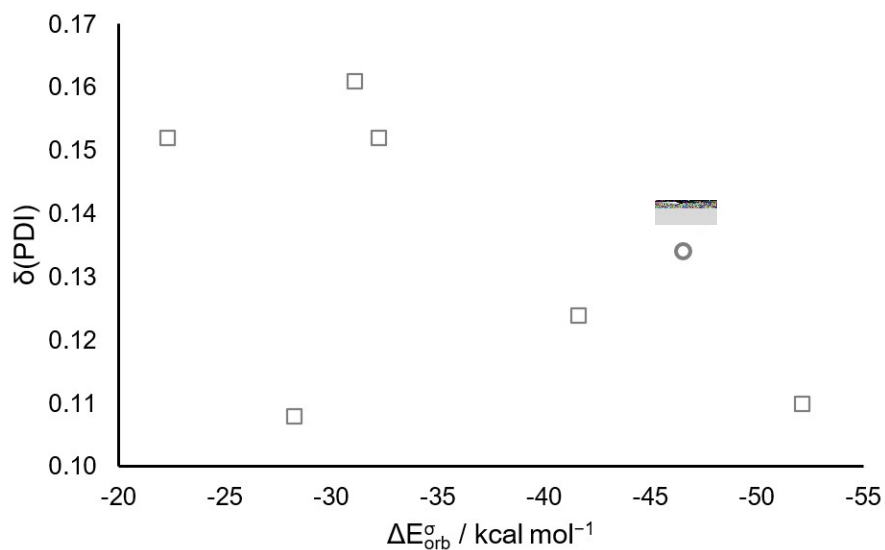


Figure S55. Calculated L–Rh σ donation energies (ETS–NOCV, $\Delta E_{\text{orb}}^{\sigma}$) plotted against experimental $\delta(\text{PDI})$ values for selected $\text{Rh}(\text{DippPDI})(\text{L})$ complexes.

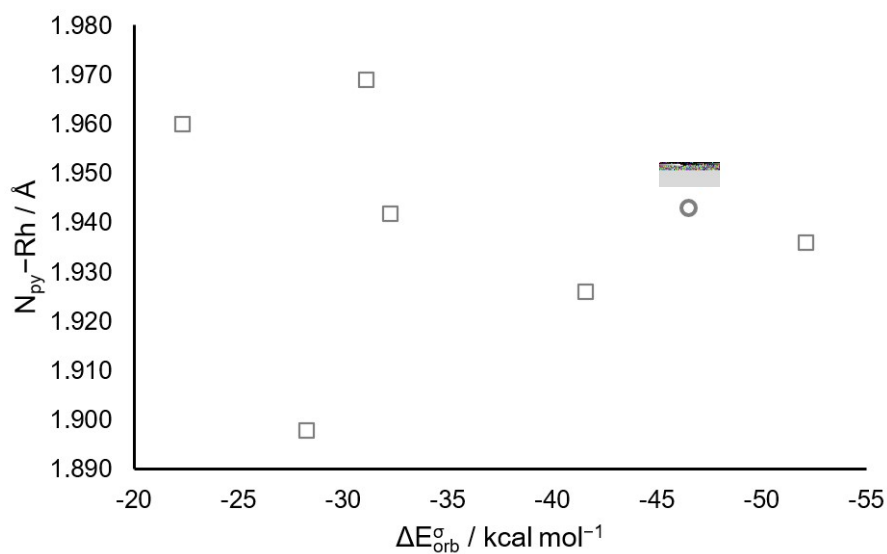


Figure S56. Calculated L–Rh σ donation energies (ETS–NOCV, $\Delta E_{\text{orb}}^{\sigma}$) plotted against experimental solid-state $\text{N}_{\text{py}}\text{-Rh}$ bond lengths for selected $\text{Rh}(\text{DippPDI})(\text{L})$ complexes.

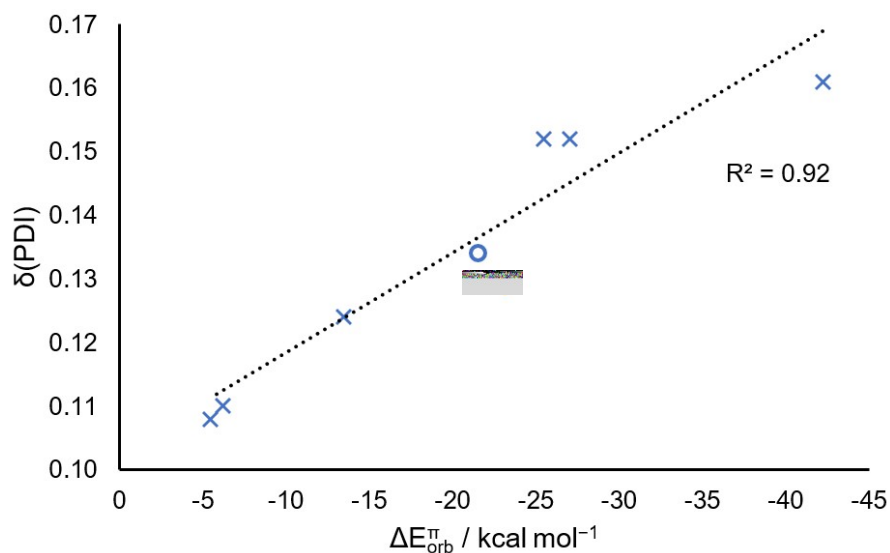


Figure S57. Calculated Rh–L π back-donation energies (ETS-NOCV, ΔE_{orb}) plotted against experimental $\delta(\text{PDI})$ values for selected $\text{Rh}(\text{DippPDI})(\text{L})$ complexes.

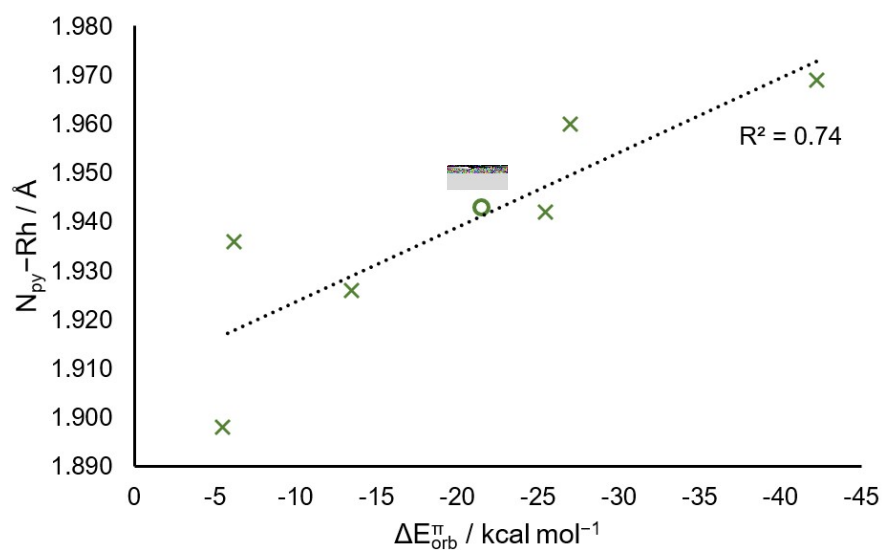


Figure S58. Calculated Rh–L π back-donation energies (ETS-NOCV, ΔE_{orb}) plotted against experimental solid-state $N_{\text{py}}\text{-Rh}$ bond lengths for selected $\text{Rh}(\text{DippPDI})(\text{L})$ complexes.

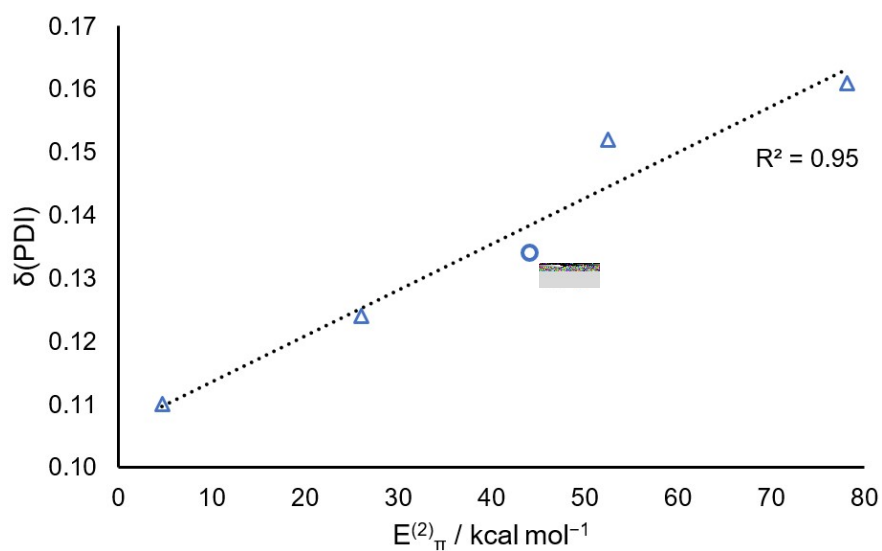


Figure S59. Calculated Rh–L π back-donation energies (NBO, $E^{(2)}_{\pi}$) plotted against experimental $\delta(\text{PDI})$ values for selected $\text{Rh}(\text{DiPPDI})(\text{L})$ complexes.

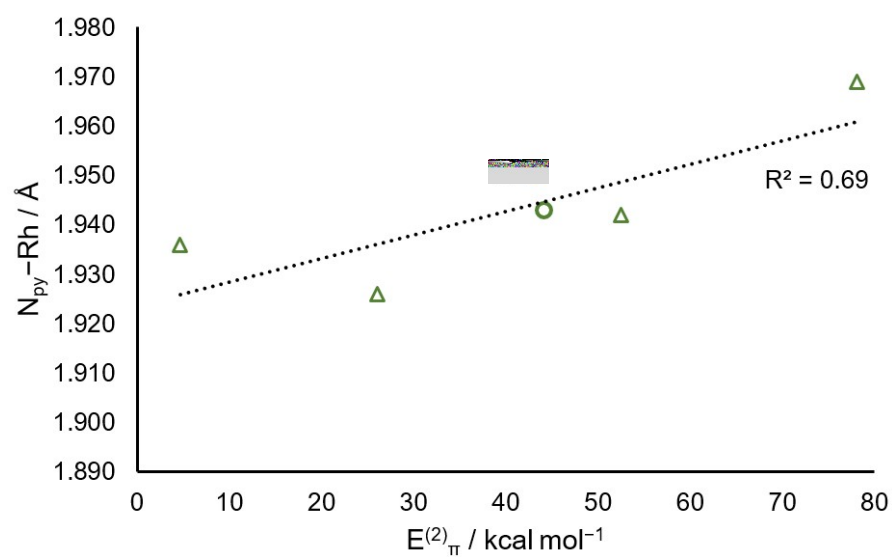


Figure S60. Calculated Rh–L π back-donation energies (NBO, $E^{(2)}_{\pi}$) plotted against experimental solid-state $N_{\text{py}}\text{-Rh}$ bond lengths for selected $\text{Rh}(\text{DiPPDI})(\text{L})$ complexes.

4. References

- 1 A. J. Martínez-Martínez and A. S. Weller, *Dalton Trans.*, 2019, **48**, 3551–3554.
- 2 C. C. Hojilla Atienza, C. Milsman, E. Lobkovsky and P. J. Chirik, *Angew. Chem. Int. Ed.*, 2011, **50**, 8143–8147.
- 3 V. C. Gibson, M. J. Humphries, K. P. Tellmann, D. F. Wass, A. J. P. White and D. J. Williams, *Chem. Commun.*, 2001, **1**, 2252–2253.
- 4 S. Nüchel and P. Burger, *Organometallics*, 2001, **20**, 4345–4359.
- 5 Q. Knijnenburg, D. Hettterscheid, T. Martijn Kooistra and P. H. M. Budzelaar, *Eur. J. Inorg. Chem.*, 2004, **2004**, 1204–1211.
- 6 D. W. N. Wilson, S. J. Urwin, E. S. Yang and J. M. Goicoechea, *J. Am. Chem. Soc.*, 2021, **143**, 10367–10373.
- 7 E. L. Dias, M. Brookhart and P. S. White, *Organometallics*, 2000, **19**, 4995–5004.
- 8 CrysAlisPro, Agilent Technologies, Version 1.171.41.117a.
- 9 (a) G. M. Sheldrick in SHELXL97, *Programs for Crystal Structure Analysis (Release 97-2)*, Institut für Anorganische Chemie der Universität, Tammanstrasse 4, D-3400 Göttingen, Germany, 1998; (b) G. M. Sheldrick, *Acta Crystallogr. Sect. A*, 1990, **46**, 467–473; (c) G. M. Sheldrick, *Acta Crystallogr. Sect. A*, 2008, **64**, 112–122.
- 10 F. Neese, *Wiley Interdiscip. Rev. Comput. Mol. Sci.*, 2012, **2**, 73–78.
- 11 F. Neese, *Wiley Interdiscip. Rev. Comput. Mol. Sci.*, 2018, **8**, 1–6.
- 12 F. Neese, F. Wennmohs, U. Becker and C. Riplinger, *J. Chem. Phys.*, 2020, **152**, 224108.
- 13 S. Grimme, *J. Comput. Chem.*, 2006, **27**, 1787–1799.
- 14 F. Weigend and R. Ahlrichs, *Phys. Chem. Chem. Phys.*, 2005, **7**, 3297–3305.
- 15 Y. S. Lin, G. De Li, S. P. Mao and J. Da Chai, *J. Chem. Theory Comput.*, 2013, **9**, 263–272.
- 16 D. A. Pantazis, X. Y. Chen, C. R. Landis and F. Neese, *J. Chem. Theory Comput.*, 2008, **4**, 908–919.
- 17 M. Bühl, C. Reimann, D. A. Pantazis, T. Bredow and F. Neese, *J. Chem. Theory Comput.*, 2008, **4**, 1449–1459.
- 18 E. D. Glendening, J. K. Badenhoop, A. E. Reed, J. E. Carpenter, J. A. Bohmann, C. M. Morales, P. Karafiloglou, C. R. Landis and F. Weinhold, *NBO 7.0*, Theoretical Chemistry Institute, University of Wisconsin, Madison, 2018.
- 19 M. Mitoraj and A. Michalak, *J. Mol. Model.*, 2007, **13**, 347–355.
- 20 L. Zhao, M. von Hopffgarten, D. M. Andrada and G. Frenking, *Wiley Interdiscip. Rev. Comput. Mol. Sci.*, 2018, **8**, e1345.
- 21 T. Lu and F. Chen, *J. Comput. Chem.*, 2012, **33**, 580–592.
- 22 S. E. Bradforth, E. H. Kim, D. W. Arnold and D. M. Neumark, *J. Chem. Phys.*, 1998, **98**,

- 800–810.
- 23 J. Zhou, E. Garand and D. M. Neumark, *J. Chem. Phys.*, 2007, **127**, 114313.
 - 24 Russell D. Johnson III, *NIST Computational Chemistry Comparison and Benchmark DataBase (Release 22): NIST Standard Reference Database Number 101* can be found under <http://cccbdb.nist.gov/>, **2022**.
 - 25 E. S. Yang and J. M. Goicoechea, *Angew. Chem. Int. Ed.*, 2022, **61**, e202206783.
 - 26 S. Gaillard, A. M. Z. Slawin and S. P. Nolan, *Chem. Commun.*, 2010, **46**, 2742–2744.
 - 27 C. M. Zinser, F. Nahra, L. Falivene, M. Brill, D. B. Cordes, A. M. Z. Slawin, L. Cavallo, C. S. J. Cazin and S. P. Nolan, *Chem. Commun.*, 2019, **55**, 6799–6802.
 - 28 E. Y. Tsui, P. Müller and J. P. Sadighi, *Angew. Chem. Int. Ed.*, 2008, **47**, 8937–8940.
 - 29 V. J. Scott, J. A. Labinger and J. E. Bercaw, *Organometallics*, 2010, **29**, 4090–4096.
 - 30 M. R. Fructos, T. R. Belderrain, P. de Frémont, N. M. Scott, S. P. Nolan, M. Mar Díaz-Requejo and P. J. Pérez, *Angew. Chem. Int. Ed.*, 2005, **44**, 5284–5288.
 - 31 R. E. Marsh, *Acta Crystallogr. Sect. B Struct. Sci.*, 2009, **65**, 782–783.
 - 32 C. Dash, P. Kroll, M. Yousufuddin and H. V. R. Dias, *Chem. Commun.*, 2011, **47**, 4478–4480.
 - 33 L. Canovese, F. Visentin, C. Levi and V. Bertolasi, *Organometallics*, 2011, **30**, 875–883.
 - 34 S. Gaillard, P. Nun, A. M. Z. Slawin and S. P. Nolan, *Organometallics*, 2010, **29**, 5402–5408.
 - 35 P. de Frémont, N. Marion and S. P. Nolan, *J. Organomet. Chem.*, 2009, **694**, 551–560.
 - 36 M. J. Humphries, K. P. Tellmann, V. C. Gibson, A. J. P. White and D. J. Williams, *Organometallics*, 2005, **24**, 2039–2050.